Carnegie Mellon University

CARNEGIE INSTITUTE OF TECHNOLOGY

THESIS

SUBMITTED IN PARTIAL FULFILLMENT OF THE REQUIREMENTS

FOR THE DEGREE OF Doctor of Philosophy

TITLE **Visible-light Photocatalytic Activity of $TiO_2/BiFeO_3$ Heterostructures**

PRESENTED BY **Yiling Zhang**

ACCEPTED BY THE DEPARTMENT OF

Materials Science and Engineering

ADVISOR, MAJOR PROFESSOR — DATE

DEPARTMENT HEAD — DATE

APPROVED BY THE COLLEGE COUNCIL

DEAN — DATE

Visible-light Photocatalytic Activity of TiO_2/$BiFeO_3$ Heterostructures

Submitted in partial fulfillment of the requirements for

the degree of

Doctor of Philosophy

in

Materials Science and Engineering

Yiling Zhang

B.S., Engineering Physics, The Hong Kong Polytechnic University
M.S., Materials Science and Engineering, Carnegie Mellon University

Carnegie Mellon University
Pittsburgh, PA

February, 2013

Acknowledgements

I would like first to thank my advisors, Dr. Gregory Rohrer and Dr. Paul Salvador, for their guidance and encouragement in my PhD study and research, and for being extremely patient in editing my documents. I have learnt a great deal from them. I also owe my sincere thankfulness to Dr. Chris Pistorius, Dr. Lisa Porter, and Dr. Yi Luo, for being on my committee. My appreciations will have to go to the staff in the MSE department as well, especially to Jason Wolf, Adam Wise, and Tom Nuhfer, for their continuous assistance. The financial support of the NSF (DMR 0804770) is acknowledged.

I want to express my gratefulness to my friends and colleagues for their help. I would specially like to thank Dr. Li Li and Dr. Andrew Schultz for sharing their thoughts and helping with my experiments over the years. Also Dr. Li Li and Dr. Yimeng Lu kindly helped correcting the present documents. My thanks also go to Dr. Jason Gu and Ying Yi Dang for their XPS work and Dr. Harry Chien for his help in EBSD work.

Finally, I want to give the biggest thanks to my mom and my dad, who have always been there for me whole-heartedly. Without their support and encouragement, I would never have come this far.

Abstract

Ferroelectric polarization is believed to enhance the efficiency of a semiconductor photocatalyst, including ferroelectric/semiconductor heterojunction photocatalysts. $BiFeO_3$, which has a narrow band gap of ≈ 2.2 – 2.7 eV and can absorb visible light, is investigated as a ferroelectric substrate that supports a TiO_2 film in a photocatalytic heterostructure. The photocatalytic activity of the $TiO_2/BiFeO_3$ heterostructure is studied in detail, using visible light irradiation. The photochemical reduction of Ag^+ to Ag^0 in an aqueous silver nitrate solution under illumination from a blue light emitting diode is used to characterize the activity of the heterostructures and related samples. The photocatalytic activity is quantified by measuring the heights of the reduction products using atomic force microscopy.

The observation of spatially selective silver patterns on the surface of the heterostructure after reaction suggests that electrons photogenerated in the $BiFeO_3$ substrate migrate, under the influence of ferroelectric polarization, to the TiO_2 surface, where they participate in the photochemical reduction reaction. This is supported by the correlation of the reduced silver pattern and the ferroelectric domain structure as revealed by piezoresponse force microscopy (PFM). To establish correlation between out-of-plane polarity of domains and photochemical activity for both bare $BiFeO_3$ and $TiO_2/BiFeO_3$, analysis of domain structures using PFM responses and crystallographic orientation information and comparison to reactivity patterns are made.

To study the dependence of photocatalytic activity of the heterostructures on the TiO_2 phase and orientation, the orientation relationships (ORs) of TiO_2 and

$BiFeO_3$ are determined via the Combinatorial Substrate Epitaxy technique using electron backscatter diffraction data of each grain in a heterostructure having a thick TiO_2 film on a polycrystalline $BiFeO_3$ substrate. It is found that the three dimensional alignment of closest packed planes and directions of TiO_2 and $BiFeO_3$ drives the epitaxial growth regardless of their interface planes As a result, anatase grows on $BiFeO_3$ with the OR $(112)_A \parallel (111)_{BFO}$ and $[1\bar{1}0]_A \parallel [1\bar{1}0]_{BFO}$ within 35° of $[100]_{BFO}$. Rutile grows on other $BiFeO_3$ orientations with $(100)_R \parallel (111)_{BFO}$, and with in-plane orientation being primarily $[001]_R \parallel [1\bar{1}0]_{BFO}$ and secondarily $[001]_R \parallel [\bar{1}2\bar{1}]_{BFO}$.

Comparisons of the amounts of reduced silver on TiO_2 film grains with distinct phases/orientations show that the heterostructure reactivity is approximately the same on anatase and rutile grains and is not strongly affected by the crystallographic orientation of both phases, an observation that contrasts the behavior of bulk TiO_2 (under UV irradiation) but is in agreement with the behavior of UV-light absorbing ferroelectric / titania heterostructures. Collectively these observations demonstrated that TiO_2 heterostructures can be engineered with visible light absorbing sensitizers that spatially separate the oxidation and reduction reaction, which will increase overall efficiencies.

Table of Contents

List of Figures

List of Tables

Chapter 1 Introduction

Solar energy harvesting is a promising solution to the ever-pressing crisis of conventional energy source depletion. Solar energy is abundant in supply as the radiation energy from the Sun arriving on Earth is about 10,000 times as much as the world energy consumption every second. Hydrogen, which is a renewable energy source that does not create carbonaceous green house gases after burning can be produced from photolysis of water using solar energy. Photocatalysis has been one focus of the materials research community worldwide since the discovery of photolytic activity of titania under ultraviolet (UV) light in 1972 by Fujishima and Honda.[1] Based on the observation that oxygen evolution occurred when a TiO_2 electrode was irradiated with UV light, it was proposed that the dissociation of water could be achieved via the following reactions:

$$2H^+ + 2e^- \longrightarrow H_2 \quad (1)$$

$$H_2O + 2h^+ \longrightarrow 2H^+ + \frac{1}{2}O_2 \quad (2)$$

In the photolytic process, titania serves as a photocatalyst. The electrons are excited from the valence band of titania by the irradiation and migrate to the Pt electrode to react with protons (H^+) in aqueous solution to produce hydrogen, and the holes in the valence band react with H_2O to produce oxygen. On the basis of this mechanism, there are mainly two approaches to generate hydrogen. The first approach is a photoelectrochemical (PEC) cell, depicted in Fig. 1.1, which was used in the work of Fujishima and Honda.[1] The second approach is a colloidal catalyst,[2] where a

particulate oxide, usually titania, with a small amount of Pt on the surface forms tiny local PEC cells, as shown in Fig. 1.2.

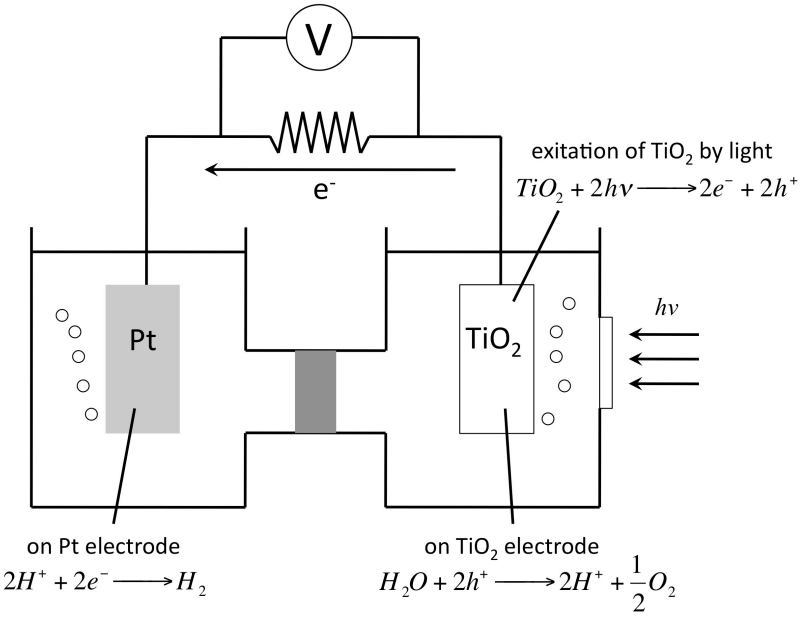

Figure 1.1 The photoelectrochemical cell by Fujishima and Honda.[1] Electrons excited by irradiation migrate through an external circuit to the Pt electrode where they react with H^+ to produce H_2. Holes in the TiO_2 electrode react with H_2O to produce O_2.

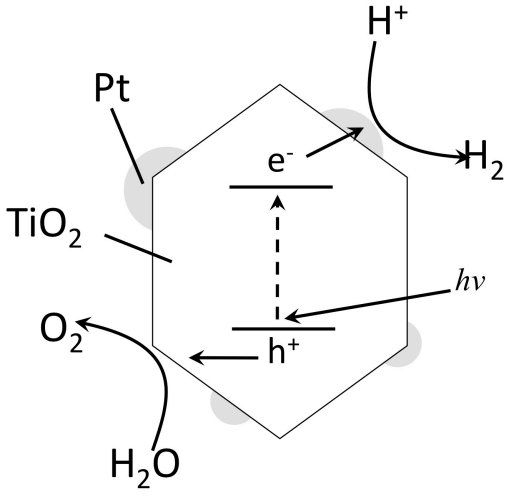

Figure 1.2 A Pt-TiO_2 colloidal photocatalyst.[2] Electrons excited inside TiO_2 migrate to Pt deposited on the surface to react with H^+ to produce H_2. Holes migrate to the TiO_2 surface, where they react with H_2O to produce O_2.

The PEC cells are efficient, but are expensive to build. On the contrary, the colloidal catalysts are cheap, but are much less efficient. There is not yet a large-scale application of photocatalysis developed based on either of the two approaches. Over the past four decades, the research community has been continuously making efforts to improve the photocatalytic activity of TiO_2. For example, various strategies have been employed to extend the absorption edge into the visible range, as will be mentioned later in Chapter 2.

This work uses the approach of growing titania films on ferroelectric materials to create better photocatalysts. Prior works by Burbure *et al.*[3-6] have demonstrated enhanced activity of titania supported on ferroelectric $BaTiO_3$. In the TiO_2/ferroelectric heterostructure, the TiO_2 film serves as protection against photocorrosion and degradation in an aqueous environment for the ferroelectric substrate. The internal electric fields induced by ferroelectric polarization drive electrons and holes in opposite directions and decrease their chance of recombination.[7-11] Owing to the separation of charge carriers, the hydrogen and oxygen production reactions also take place in separated spaces. Consequently, the chance for reaction intermediates to back-react is reduced. Both effects are believed to lead to an enhancement of the overall photocatalytic efficiency. Herein, $BiFeO_3$ is chosen as the ferroelectric material on which titania is deposited. $BiFeO_3$'s narrow band gap 2.2 – 2.7 eV[12-14] allows it to create charge carriers upon absorption of visible light, which is beyond the capability of titania and $BaTiO_3$.

In the present work, the proposed photocatalytic mechanism, which will be described in Chapter 2, is supported by the experimental results. Besides, the

influence of phase and crystallographic orientation of TiO_2 film on the photocatalytic activity is examined, which also leads to the finding of epitaxial relationships of titania and $BiFeO_3$.

References:

[1]A. Fujishima and K. Honda, "Electrochemical Photolysis of Water at a Semiconductor Electrode," *Nature*, **238**[5358] 37-38 (1972).

[2]S. Sato and J. M. White, "Photo-Decomposition of Water over p-TiO_2 Catalysts," *Chem. Phys. Lett.*, **72**[1] 83-86 (1980).

[3]N. V. Burbure, "Influence of Ferroelectric Substrates on the Photochemical Reactivity of Titanium Dioxide Thin Films," *PhD Thesis* (2009).

[4]N. V. Burbure, P. A. Salvador, and G. S. Rohrer, "Influence of Dipolar Fields on the Photochemical Reactivity of Thin Titania Films on $BaTiO_3$ Substrates," *J. Am. Ceram. Soc.*, **89**[9] 2943-45 (2006).

[5]N. V. Burbure, P. A. Salvador, and G. S. Rohrer, "Photochemical Reactivity of Titania Films on $BaTiO_3$ Substrates: Origin of Spatial Selectivity," *Chem. Mater.*, **22**[21] 5823-30 (2010).

[6]N. V. Burbure, P. A. Salvador, and G. S. Rohrer, "Photochemical Reactivity of Titania Films on $BaTiO_3$ Substrates: Influence of Titania Phase and Orientation," *Chem. Mater.*, **22**[21] 5831-37 (2010).

[7]S. Dunn, P. M. Jones, and D. E. Gallardo, "Photochemical Growth of Silver Nanoparticles on c^- and c^+ Domains on Lead Zirconate Titanate Thin Films," *J. Am. Chem. Soc.*, **129**[28] 8724-28 (2007).

[8]J. L. Giocondi and G. S. Rohrer, "Spatial Separation of Photochemical Oxidation and Reduction Reactions on the Surface of Ferroelectric $BaTiO_3$," *J. Phys. Chem. B*, **105**[35] 8275-77 (2001).

[9]J. L. Giocondi and G. S. Rohrer, "Spatially Selective Photochemical Reduction of Silver on the Surface of Ferroelectric Barium Titanate," *Chem. Mater.*, **13**[2] 241-42 (2001).

[10]P. M. Jones, D. E. Gallardo, and S. Dunn, "Photochemical Investigation of a Polarizable Semiconductor, Lead-Zirconate-Titanate," *Chem. Mater.*, **20**[18] 5901-06 (2008).

[11]S. V. Kalinin, D. A. Bonnell, T. Alvarez, X. Lei, Z. Hu, J. H. Ferris, Q. Zhang, and S. Dunn, "Atomic Polarization and Local Reactivity on Ferroelectric Surfaces: A New Route Toward Complex Nanostructures," *Nano Lett.*, **2**[6] 589-93 (2002).

[12]S. R. Basu, "Photoconductivity in $BiFeO_3$ Thin Films," *Appl. Phys. Lett.*, **92**[9] 091905 (2008).

[13]T. Choi, S. Lee, Y. J. Choi, V. Kiryukhin, and S.W. Cheong, "Switchable Ferroelectric Diode and Photovoltaic Effect in $BiFeO_3$," *Science*, **324**[5923] 63-66 (2009).

[14]F. Gao, "Preparation and Photoabsorption Characterization of $BiFeO_3$ Nanowires," *Appl. Phys. Lett.*, **89**[10] 102506 (2006).
[15]R. G. Breckenridge and W. R. Hosler, "Electrical Properties of Titanium Dioxide Semiconductors," *Phys. Rev.*, **91**[4] 793-802 (1953).

Chapter 2 Background

Beginning with a brief introduction of photocatalysis with titania, this chapter focuses on the photocatalytic mechanism of TiO_2/$BiFeO_3$ heterostructures. The energy level diagram of the TiO_2/$BiFeO_3$ heterostructure, which helps us understand the photocatalytic behavior, is constructed step-by-step based on literature values. Epitaxial relationships of titania on $BiFeO_3$, which are important in the study of photocatalytic activity as a function of crystallographic orientation, are described in the final section of the chapter.

2.1 Photocatalysis with TiO_2

In this section, prior work on TiO_2 photocatalysis is reviewed. Photochemical marker reaction is also introduced here, and it will be extensively applied in the whole work.

2.1.1 Brief history

In 1972, TiO_2 was discovered by Fujishima and Honda[1] to be capable of splitting H_2O to hydrogen and oxygen in an electrochemical cell under ultraviolet (UV) light illumination. According to their report, a current flow was detected from the platinum electrode to the TiO_2 electrode and oxygen evolution occurred on the TiO_2 anode when the TiO_2 was irradiated with UV light (>3.0 eV). As mentioned in the introduction chapter, Fig. 1.1 is a schematic drawing of the electrochemical cell[1]. The photocatalytic process will be described later in Section 2.1.2. Later, powdered TiO_2 impregnated with Pt[2] or RuO_2[3] was reported to be capable of producing

hydrogen and oxygen continuously under UV light. TiO_2's ability to produce hydrogen from water through photocatalysis represented a novel method of converting of solar energy to useful chemical energy.

2.1.2 Photocatalytic process of TiO_2

2.1.2.1 Photo-generation of charge carriers in TiO_2

Charge carriers, electrons and holes, can be photogenerated in semiconductors such as TiO_2. The band structure of a semiconductor is essential in determining what photons can be absorbed by the semiconductor. Fig. 2.1 is an energy level diagram of a generic semiconductor. E_C is the conduction band edge; E_V is the valence band edge. The distance between E_C and E_v is the band gap E_g. A photon with energy greater than E_g can be absorbed by the semiconductor to excite an electron from the valence band to the conduction band. The void left behind in the valence band is a hole, which is often considered as a positively charged particle. The electron and the hole will take part in the photochemical reactions described in section 2.1.2.2.

The details of the band structure are determined in part by the crystal structure of the semiconductor. TiO_2 has three important phases that can be stabilized at room temperature: anatase, rutile, and brookite. Anatase and rutile phases are the major phases and both are of interest to the current work. The band gap energy E_g is 3.2 eV for anatase[4,5] and 3.0 eV for rutile.[6,7] Due to their relatively large band gaps, both phases only absorb UV light to generate electrons and holes from the above-described absorption mechanism.

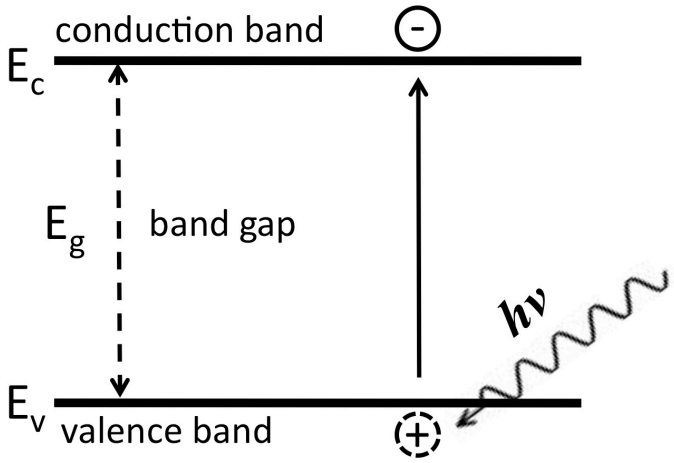

Figure 2.1 The energy level diagram of a generic semiconductor. E_C is the conduction band edge; E_V is the valence band edge; E_g is the band gap. When a photon with energy > E_g comes in and is absorbed by an electron in the valence band, the electron is excited to the conduction band.

2.1.2.2 Photochemical reactions

The overall photochemical reaction to produce hydrogen from water using photons of light is:

$$2H_2O \xrightarrow{h\nu} 2H_2 + O_2$$

This reaction can be divided into two half reactions as given in Fig. 1.1:

$$2H^+ + 2e^- \longrightarrow H_2 \qquad (1)$$

$$H_2O + 2h^+ \longrightarrow 2H^+ + \frac{1}{2}O_2 \qquad (2)$$

Reaction (1) is the reduction (cathodic) half reaction, which consumes electrons to produce hydrogen. In Fig. 1.1, the photo-generated electrons travel through the external circuit to reach the surface of the Pt electrode, where they react with the hydrogen ions in the water to form hydrogen. Reaction (2) is the oxidation (anodic) half reaction, which consumes holes to produce oxygen. In Fig. 1.1, the photo-

generated holes on the surface of the TiO_2 electrode react with water molecules to form oxygen.

Because hydrogen produced in a photochemical process bubbles out of the aqueous solution, it is difficult to track the reaction sites from where it is emanated. For the present study, reduction of Ag^+ in aqueous $AgNO_3$ solution, which generates solid products at reactions sites on the surface, is used as a "marker reaction". The reduced Ag can be easily tracked and its amount can be measured using atomic force microscopy. This reduction reaction, which replaces reaction (1), is expressed as following:

$$Ag^+ + e^- \longrightarrow Ag \qquad (3)$$

Ag^+ in the silver nitrate ($AgNO_3$) solution captures an electron to be reduced to Ag^0 and precipitates as a solid at the reaction site.

Fig. 2.2 is an energy level diagram showing the band edge positions of TiO_2 on the left of the y-axis and the redox potential levels on the right of the y-axis. For a water-splitting photocatalyst, its conduction band (CB) edge has to be higher than the redox level of H^+/H_2 and its valence band (VB) edge has to be lower than the redox level of H_2O/O_2, TiO_2 is such a photocatalyst. Regarding the marker reaction, since the Ag^+/Ag redox level is much lower than the H^+/H_2 level, the reaction will much easier to proceed.

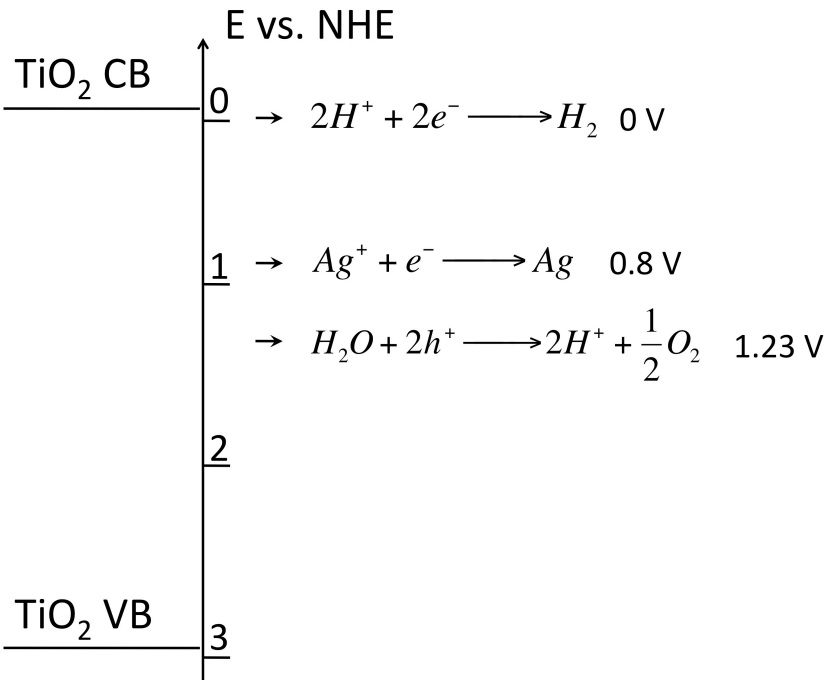

Figure 2.2 Energy level diagram showing the redox potential levels for the relevant reactions[8] and the positions for the conduction band (CB) edge and the valence band (VB) edge of TiO_2.

2.1.3 Barrier for massive application of photocatalysis with TiO_2

Because of the large band gaps of TiO_2 (rutile and anatase), they can only utilize the UV portion (~3%) of the solar spectrum. This leads to the low efficiency of TiO_2 photocatalysts. Despite much research effort over the past four decades, there is not yet a massive application of photocatalysis with TiO_2 to produce hydrogen on an industrial level.

There are two approaches to achieve hydrogen production with TiO_2. The first approach is to use photoelectrochemical (PEC) cells.[1,9] An example of a PEC cell is the one by Fujishima and Honda (see Fig. 1.1).[1] The other approach is to use powdered catalysts.[10] Pt-deposited TiO_2 particles form tiny PEC cells (see Fig. 1.2). Photogenerated electrons migrate to the Pt deposits where they reduce hydrogen

ions to hydrogen; holes on TiO_2 particles oxidize water molecules to oxygen, as shown in Fig. 1.2. The PEC cell approach is more efficient than the powdered catalyst approach because the photo-generated electrons and holes in the PEC cells are well separated through the external circuit, lowering their chance of recombination as well as the chance of back-reaction of reduced and oxidized intermediate species. However, the PEC cells are much more expensive to build than the powdered catalysts. Up to date, no cost-effective system has been developed in either approach.

2.1.4 Efforts to improve photocatalytic activity

The photocatalytic activity of TiO_2 has been improved via a number of strategies including extrinsic doping, addition of adsorbed species, and making nano-sized TiO_2. Extrinsic doping adds electronic levels in the band gap of TiO_2 that can extend the absorption edge into the visible range. For example, N-doped TiO_2 has been shown to have electronic states approximately 0.75 eV above the valence band edge.[11-18] In general, doping increases the photocatalytic activity of TiO_2 in 400 – 600 nm range. However, dopants also become recombination centers that decrease the efficiency of the photochemical process.[19] Adding an adsorbed molecular species that can absorb visible light and donate an electron or a hole to the TiO_2 facilitates the photocatalytic process.[20-22] Photocatalysis with nano-sized TiO_2 has the advantages of high specific surface areas[23,24] and fast diffusion of charge carriers to surfaces.[24,25] Besides all that, an alternative method of using

ferroelectric materials to improve photocatalytic activity has emerged recently, as discussed in detail in section 2.2.

2.2 Photocatalysis with ferroelectric materials

The present work focuses on a different method to improve the photocatalytic activity of semiconductor materials, which takes advantage of spontaneous polarizations in ferroelectric materials. The internal electric fields induced by the spontaneous polarizations spatially separate the photogenerated charge carriers to improve the overall activity.

2.2.1 Origin of internal electric fields

To introduce the internal electric fields present in ferroelectric materials, $BiFeO_3$ is used as an example. $BiFeO_3$ is a perovskite-type ferroelectric material.[26] Its rhombohedral unit cell[27] is only slightly distorted from the ideal cubic structure and thus can be considered as a pseudo-cubic perovskite as shown in Fig. 2.3. The origin of a ferroelectric spontaneous polarization can be explained by the two Bi-Fe distances along the three-fold axes.[26] The Fe atom at the center of the cell is displaced along the eight equivalent <111> directions (one of them shown as the green vector in Fig. 2.3). The polarization has a magnitude of 6.1 μC cm^{-2} for bulk specimens.[28]

A domain is a continuous space within a ferroelectric crystal where all of the spontaneous polarizations are pointing in a single direction. In $BiFeO_3$, there are three possible angles between the polarization vectors of adjacent domains: 71°,

109°, and 180°.[29-31] The boundaries between domains are {100} and {110} type planes for 71° and 109° domain boundaries, respectively.[31] The 180° domain boundary planes can take any orientation in the zone of [111].[32]

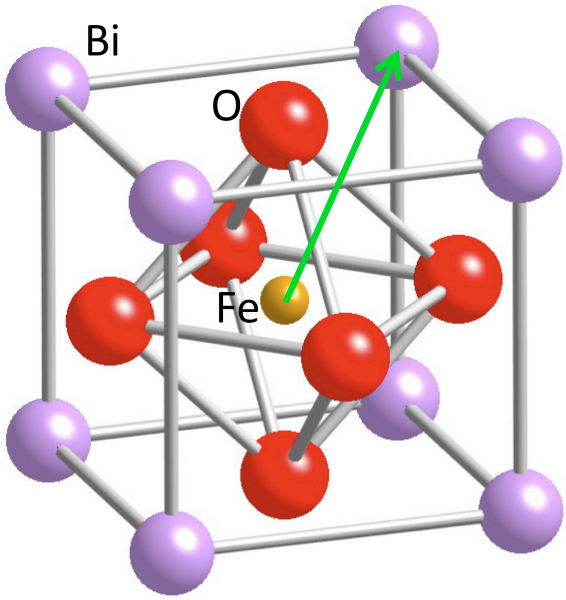

Figure 2.3 The unit cell of the pseudo-cubic $BiFeO_3$ crystal. The different types of atoms (Bi, Fe, O) are designated in the drawing. The green arrow shows one of the <111> directions of spontaneous polarization.

The spontaneous polarization (P_s) in a domain induces an internal electric field that has significant influence on the transport of charge carriers in that domain. The concept of internal electric field is first hypothesized by Chen.[33] As shown in Fig. 2.4, the spontaneous polarization induces bound charge layers at the ends of the P_s vectors. The bound charge layers in turn induce the internal electric field E anti-parallel with P_s. This field, whose intensity scales with the magnitude of P_s, counteracts the P_s. It is called the depolarizing field. Electrons and holes, once excited by photons, are driven in opposite directions, and their chance of recombination is reduced.[34-38]

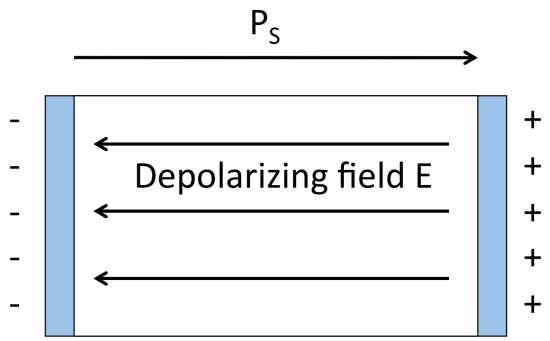

Figure 2.4 The spontaneous polarization P_s induces the bound charge layers at both ends of the domain. The bound charge layers create the depolarizing field E in the opposite direction of P_s.

2.2.2 Photocatalytic activity of TiO_2 with ferroelectric $BaTiO_3$

The work by Burbure *et al*. has shown that the photocatalytic activity of TiO_2 is influenced by the underlying ferroelectric substrate $BaTiO_3$.[39-42] The reduction and oxidation reactions in photochemical processes under UV light occur on spatially distinctive regions on the surface of the TiO_2 film supported by the $BaTiO_3$. After the photochemical reaction, the pattern of the products Ag deposits reduced from Ag^+ in $AgNO_3$ solution is consistent with the domain pattern of the $BaTiO_3$ substrate underneath the TiO_2 film.[40,41] The pattern of the products PbO_2 deposits oxidized from Pb^{2+} in $Pb(CH_3COO)_2$ solution is complementary to the pattern of Ag deposits.[41] Fig. 2.5[41] is the figure demonstrating the complementary locations of the reaction products, Ag and PbO_2. The arrows in Fig. 2.5 (a,b) point at the same locations. The stripes marked by the arrows in the Fig. 2.5 (a) do not have Ag particles deposited. In Fig. 2.5 (b), they are covered with PbO_2 deposits. Identical observations are made for $BaTiO_3$ that has no TiO_2 film.[35] It is also observed that the spatial localization of the reaction products diminishes as the thickness of the TiO_2

film increases.[41] In Fig. 2.6,[41] the AFM topographic images of the surfaces of three $BaTiO_3$ substrates (with 10, 30, and 50 nm TiO_2 films, respectively) after Ag reduction reaction are shown. From the height profiles, it is clear that as the film thickness increases, the amount of Ag deposits after reaction decreases.

From all of these observations, it is concluded that the internal electric fields have significant influence on the photocatalytic activity of the $TiO_2/BaTiO_3$ heterostructure. Also, the electrons and holes photogenerated in the substrate are responsible for the spatial selectivity on the film surface.[39] This is because if the electrons and holes were from the films, we would expect the amount of Ag deposits to increase with increasing film thickness, which is inconsistent with the observation.

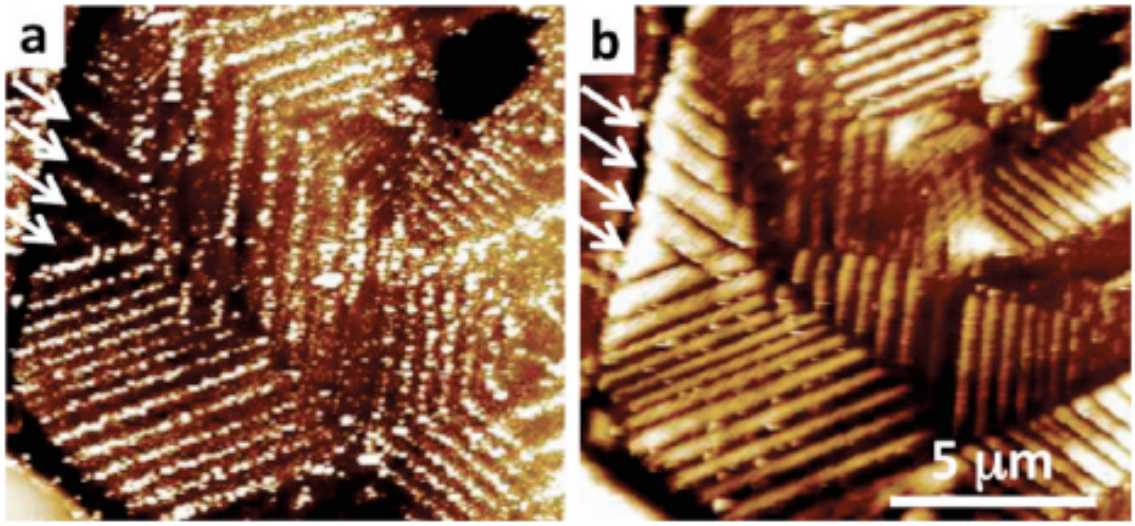

Figure 2.5 Topographic AFM images of a 15 nm thick TiO_2 film surface (a) after reaction with silver nitrate solution and (b) after reaction in lead acetate solution. The arrows in the upper left corner draw attention to the complementary width of the reduced silver and oxidized lead stripes.[41]

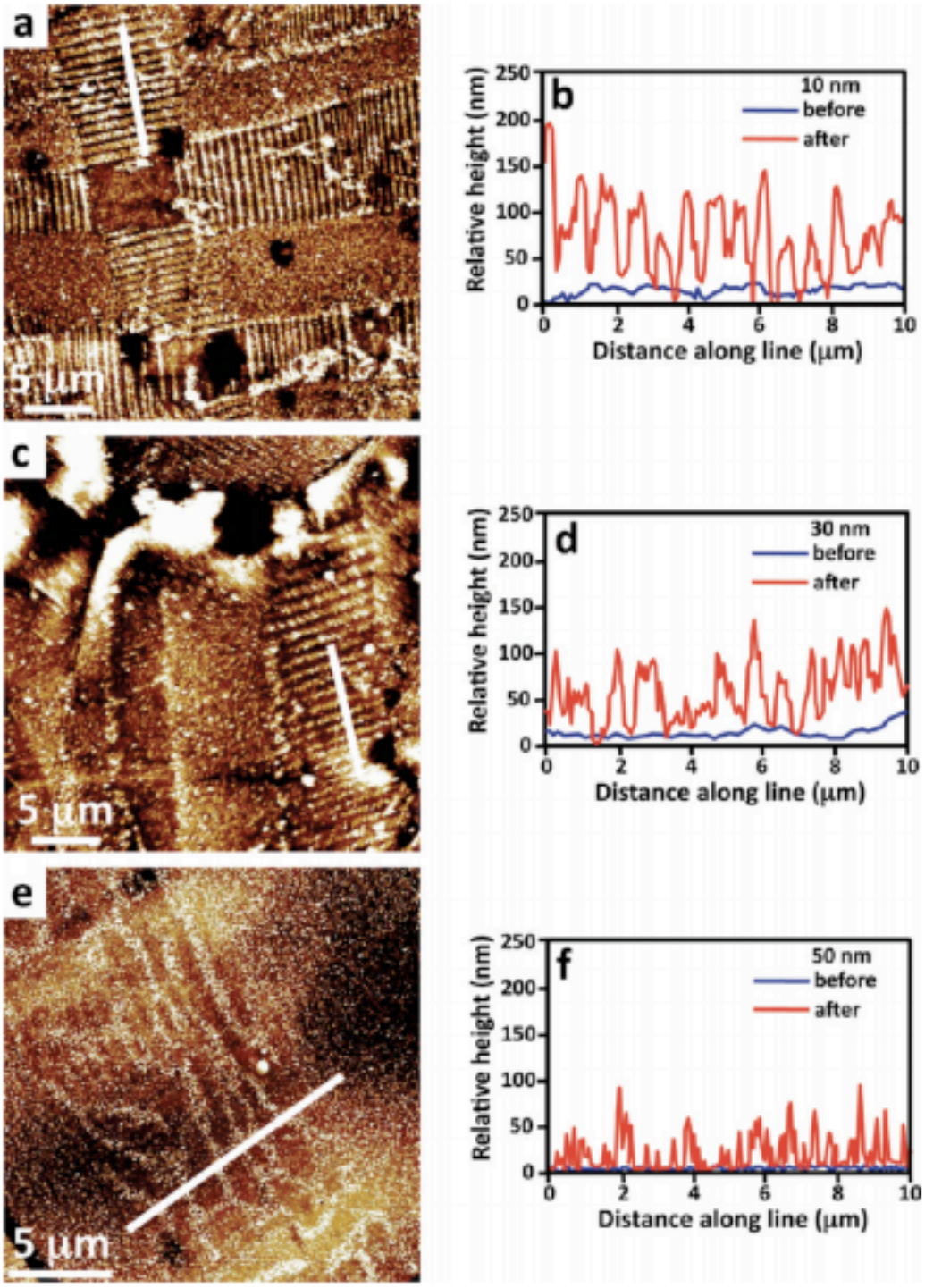

Figure 2.6 Topographic AFM images (a, c, e) and height profiles (b, d, f) for reacted TiO_2 films after silver reduction. Height profiles were extracted along the thick white lines. The before (blue) profiles were extracted from the same locations as the after (red) profiles before the reaction. Panels a and b are for a 10 nm thick film; panels c and d are for a 30 nm thick film; and panels e and f are for a 50 nm thick film.[41]

2.3 $TiO_2/BiFeO_3$ as photocatalyst

$TiO_2/BiFeO_3$ heterostructure is the focus of the present work. Preliminary results by Burbure *et al.*[39] have demonstrated that ferroelectric $BiFeO_3$ behaves similarly to $BaTiO_3$. This section explains why we are interested in $BiFeO_3$ and provides the background information of photocatalysis with $TiO_2/BiFeO_3$.

2.3.1 Properties of $BiFeO_3$ in photocatalysis

In Section 2.2.2, $BaTiO_3$ has been demonstrated to have significant influence on the photocatalytic activity of TiO_2. However, $BaTiO_3$ has a large band gap of 3.0 eV,[43,44] which makes it only capable of absorbing photons within the UV range. Like TiO_2, this is a major hindrance for $BaTiO_3$ to be an efficient photocatalyst with visible light. In addition to being ferroelectric, $BiFeO_3$ has a smaller band gap, reported to be 2.2 – 2.7 eV,[45-47] that extends its absorption edge into the visible range. Because of that, it can utilize a larger portion of the solar energy than $BaTiO_3$ in a photocatalytic process.

However, $BiFeO_3$ by itself is not a competent catalyst in splitting water. It suffers from degradation by hydrogen during the photocatalytic process.[48] Also the conduction band edge is lower than the hydrogen reduction level.[49,50]

2.3.2 Mechanism of photocatalysis with $TiO_2/BiFeO_3$

It will be shown that $BiFeO_3$ is active under visible blue light in chapter 5, and therefore the photocatalytic reactions in the current work are conducted using

visible blue light (λ=470 nm). A detailed description of the photocatalytic process of $TiO_2/BiFeO_3$ is given in this section.

2.3.2.1 Photo-generation of charge carriers in $TiO_2/BiFeO_3$

Since the visible light provided by the LED in this work has an energy range from 2.53 to 2.70 eV, the photons are not energetic enough to excite electrons in the TiO_2 film (E_g = 3.0 or 3.2 eV), assuming the band structure of the TiO_2 film is the same as that of the bulk and uniform across the film. Thus, the visible light can only excite electrons in the $BiFeO_3$ substrate, whose E_g is 2.2 to 2.7 eV.[45-47] This photo-generation process is introduced earlier in Fig. 2.1.

2.3.2.2 Transport of charge carriers through p-n junction

The photogenerated charge carriers are driven in the $TiO_2/BiFeO_3$ heterostructure by the potential gradient, determined by the band structure. To construct the energy level diagram of the heterostructure, first we have to consider the diagrams of the two semiconductors.

(a) Energy level diagrams of TiO_2 and $BiFeO_3$

TiO_2 is typically an n-type semiconductor with oxygen vacancies as the major defect type.[6,51] For rutile, the Fermi level is located approximately 0.2 eV below the bottom of its conduction band edge E_c;[6] its band gap, distance from E_c to the valence band edge E_v, is 3.0 eV;[6,7] and its reported work function, distance from the vacuum level E_{vac} to the Fermi level E_f, is 4.2 eV.[52] For anatase, the Fermi level is only 4.2×10^{-3} eV below the conduction band edge;[51] its band gap is 3.2 eV;[4,5] and its reported

electron affinity, distance from E_{vac} to E_c, is ~ 4.4 eV.[53] Because the energy level diagrams of rutile and anatase are not very different from each other, the one of rutile is used in this work for simplicity.

$BiFeO_3$ is reported to be a p-type semiconductor, likely owing to the Bi vacancies.[54,55] The X-ray photoelectron spectroscopy (XPS) analysis (thanks to Y. Y. Dang and Dr. J. Gu, MSE, CMU) confirmed it is a p-type semiconductor. Its electron affinity is estimated to be 4.6 eV, using the method by Morrison;[56] its band gap is chosen to be 2.5 eV, averaged from all of the reported values;[45-47] and its Fermi level is estimated to be ~0.6 eV above the top of its valence band by the XPS analysis. Their respective energy level diagrams before they are in contact are depicted in Fig. 2.7.

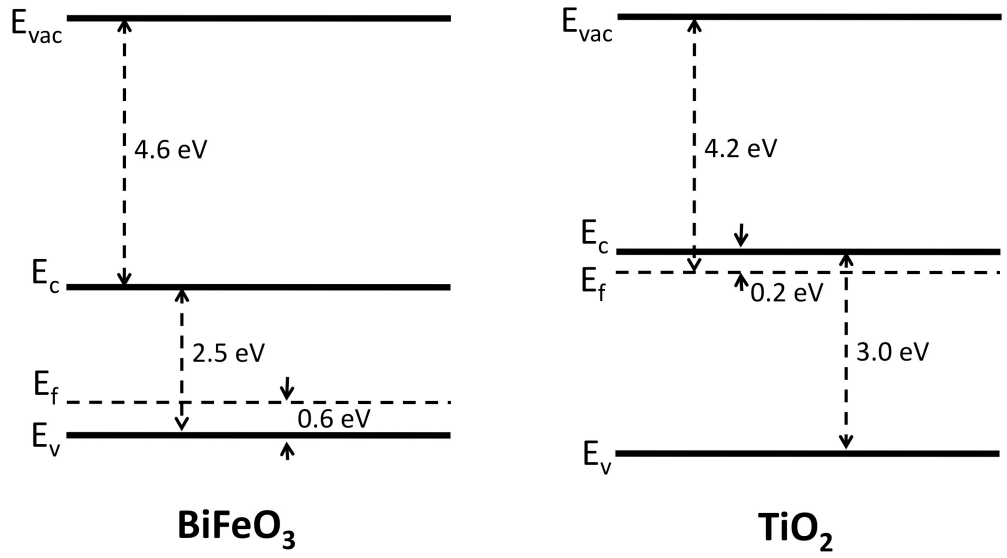

Figure 2.7 The energy level diagram of $BiFeO_3$ on the left and the band structure of rutile TiO_2 on the right. From top down, E_{vac} is the vacuum level; E_c is the conduction band edge; E_f is the Fermi level; E_v is the valence band edge, for both semiconductors.

(b) Energy level diagram of $TiO_2/BiFeO_3$ in solution

When the n-type TiO_2 and the p-type $BiFeO_3$ come into contact, a p-n junction is formed at their interface. A net transfer of charge carriers across their interface takes place until equilibrium is reached. The positive holes on the $BiFeO_3$ side and the negative electrons on the TiO_2 side annihilate one another and each side of the interface has a space charge region. For simplicity, it is assumed that no mobile charge carriers exist in both regions, and there are no trapped charges at the interface. The bands are bent upward on the $BiFeO_3$ side and downward on the TiO_2 side. With their Fermi levels aligned and the vacuum level (the reference level) smoothly connected, the band diagram of the $TiO_2/BiFeO_3$ heterostructure can be drawn as in Fig. 2.8.

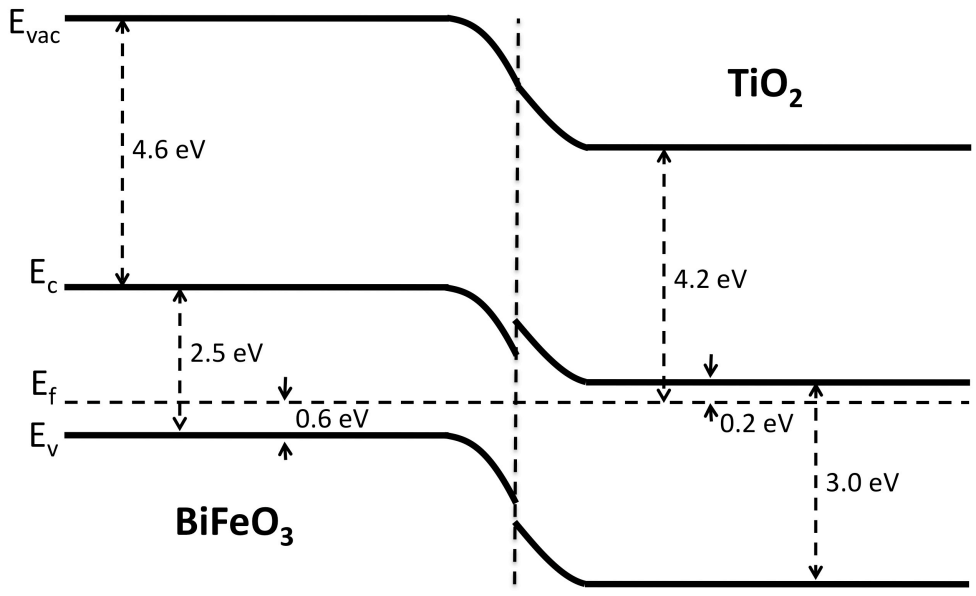

Figure 2.8 The p-n junction formed by a bulk $BiFeO_3$ and a bulk TiO_2. The Fermi levels of $BiFeO_3$ and TiO_2 are aligned and the vacuum levels are connected smoothly.

Since the TiO_2 film is in contact with a solution during the photochemical process, the surface condition of the TiO_2 has to be considered. In general, n-type TiO_2 has upward band bending at the surface,[57] creating a barrier for electrons to move to the surface. Fig. 2.9 is a more complete energy level diagram with the addition of the bent bands at the TiO_2 surface and the redox level of Ag^+/Ag in the solution.

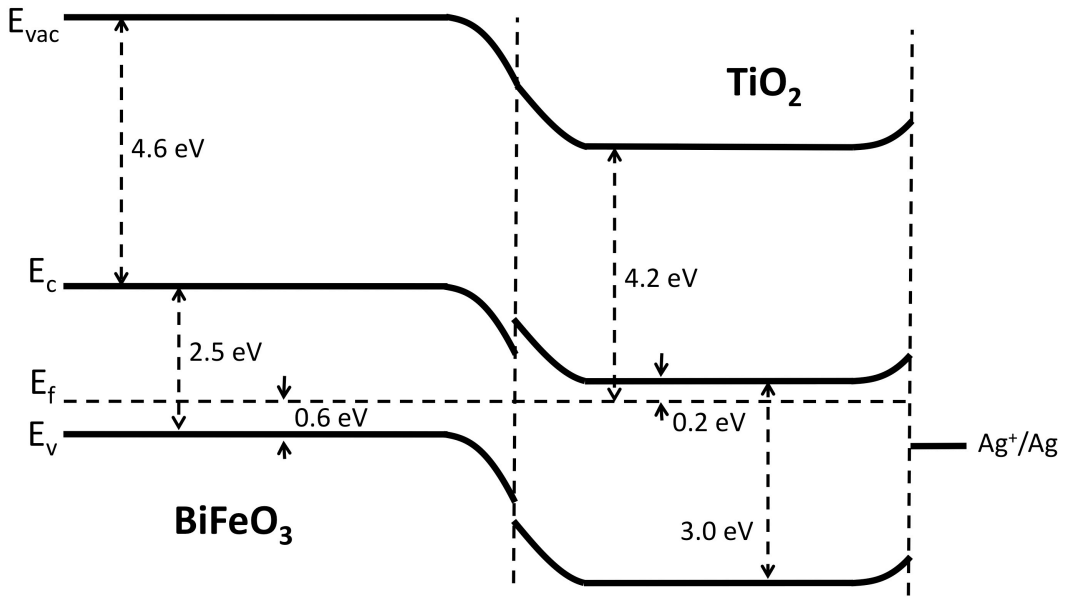

Figure 2.9 The energy level diagram of $TiO_2/BiFeO_3$ in contact with solution. At the surface of TiO_2, the bands bend upward. The redox level of Ag^+/Ag is from Fig. 2.3.

(c) Energy level diagram of thin film $TiO_2/BiFeO_3$ in solution with polarization

Note that the dimension of TiO_2 in Fig. 2.9 is large enough for its bands to fully relax to the equilibrium positions in the middle. If the thickness of the TiO_2 film is less than the expected thickness of space charge region on the TiO_2 side, the full relaxation cannot be realized. The space charge region on the TiO_2 side is caused by the p-n junction and by the spontaneous polarization.

Firstly, the p-n junction at the TiO_2/$BiFeO_3$ interface drains the electrons from the TiO_2 side. The width of the space charge region of TiO_2 can be calculated using the following equations:[58]

$$W = x_n + x_p = \left[\frac{2K_S\varepsilon_0}{q}\left(\frac{N_A + N_D}{N_A N_D}\right)V_{bi}\right]^{1/2} \quad \text{Eqn (1)}$$

$$N_A x_p = N_D x_n \quad \text{Eqn (2)}$$

where W = the total width of the space charge region (on both sides),

x_n = width of the space charge region on n-type TiO_2 side,

x_p = width of the space charge region on p-type $BiFeO_3$ side,

K_S = semiconductor dielectric constant,

ε_0 = permittivity of free space, 8.854×10^{-12} F m^{-1},

q = elementary charge, 1.6×10^{-19} C,

N_A = concentration of acceptors in $BiFeO_3$, $\sim 10^{17}$ cm^{-3},[55]

N_D = concentration of donors in TiO_2, $\sim 10^{18} - 10^{19}$ cm^{-3},[6] and

V_{bi} = potential drop across the total depletion region.

K_S is ~ 100 for TiO_2[59] and is ~ 60 for $BiFeO_3$.[60] Without introducing a large discrepancy in the calculation, K_S is assumed for simplicity to be ~ 100 the same for both materials. V_{bi}, the potential drop across the total depletion region, is the difference between the two conduction band edges when the Fermi levels are aligned, calculated to be 1.7 V. Eqn (1) calculates the total width of the space charge region W. Eqn (2) is derived from the neutrality of charge in the p-n junction. The width of the space charge region on the TiO_2 side x_n can be estimated using these two equations. Note that this estimation is rough, because it is based on some ideal

assumptions and there is a fair bit of uncertainty in the values reported for many parameters. When $N_D = 10^{18}$ cm^{-3}, x_n = 33 nm. When $N_D = 10^{19}$ cm^{-3}, x_n = 3 nm.

Secondly, to screen the spontaneous polarization from the $BiFeO_3$, free charge carriers from TiO_2 are needed. In the case that P_s is directed to the interface as in Fig. 2.10, free charge carriers ionized from the donor states in TiO_2 are accumulated at the interface to compensate for the bound charge induced by P_s. The width of the space charge region in TiO_2 for this purpose is calculated by the following equation:[61]

$$z_0 = \frac{\alpha P_S}{qN_D} \qquad \text{Eqn (3)}$$

where z_0 = width of space charge region due to P_s compensation

P_s = magnitude of spontaneous polarization in $BiFeO_3$, maximum in [111] at 6.1μC cm^{-2},[28]

α = level of compensation from 0 ~ 1,

q = elementary charge, 1.6 × 10^{-19} C, and

N_D = concentration of donors in TiO_2, ~10^{18} – 10^{19} cm^{-3}.[6]

Note that only the part of the P_s normal to the surface is useful in creating the space charge region. The width of the space charge can vary from 0 to the maximum occurring at P_s = 6.1μC cm^{-2}. Assuming α = 0.5, for $N_D = 10^{18}$ and 10^{19} cm^{-3}, z_0 maximizes at 190 and 19 nm, respectively. When the spontaneous polarization is reversed, the charge at the interface becomes negative and is likely to be compensated by the holes in $BiFeO_3$.

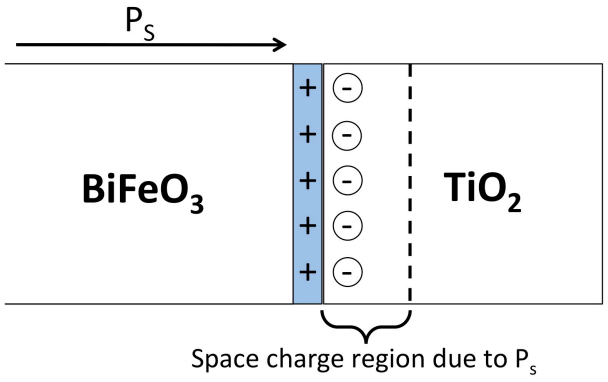

Figure 2.10 Spontaneous polarization screened by free charge carriers from TiO_2. The bound positive charge induced by P_s at the interface is indicated by "+". The free charge carriers are indicated by a circle with a "-". A space charge region due to this compensation is created as in the figure.

Combining the effect of both causes, the total width of space charge region in TiO_2 with P_s directed at the interface is estimated to vary in the range of around 30 to 200 nm if $N_D = 10^{18}$ cm^{-3}, and in the range of about 3 to 20 nm if $N_D = 10^{19}$ cm^{-3}. When P_s is inversed, the total width is estimated to vary in the range of 0 to 30 nm if $N_D = 10^{18}$ cm^{-3}, and in the range of 0 to 3 nm if $N_D = 10^{19}$ cm^{-3}. Here, cautions have to be taken that all the calculations were performed upon quite a few assumptions, both in the formulae and in the parameters from reference, such that the final results could vary by an order of magnitude. An important uncertainty in the calculation is the donor concentration in TiO_2, where the film could have a much different concentration level than the referenced number for bulk. The width of space charge region in TiO_2 has an empirical value of $\sim$ 100 nm, which is within the range in the case when $N_D = 10^{18}$ cm^{-3}.

The thicknesses of the thin TiO_2 films studied in this work (10 nm, 20 nm) are within the range of the width of the space charge region when the P_s is directed at the interface (referred to as positive domain). In this case, it is highly likely that the films are depleted of electrons and their band structures cannot return to the equilibrium positions. When P_s is reversely directed away from the interface (referred to as negative domain), despite a chance of the space charge region being very thin or even non-existent, the films are more likely depleted as in the case of positive domain.

The energy level diagrams of these two cases are depicted in Fig. 2.11. In the first case of negative domain as in Fig. 2.11 (a), the conduction band edge of $BiFeO_3$ bends upward at the interface under the influence of P_s, creating a potential barrier to prevent electrons in the conduction band from migrating to the TiO_2 film. When an electron is excited by a photon in the $BiFeO_3$ substrate near the interface, it is repelled from the interface into the interior of the $BiFeO_3$ and gets recombined with a hole somewhere there. In the second case of positive domain as in Fig. 2.11 (b), the conduction band edge bends downward, facilitating the migration of electrons to the TiO_2 film. An excited electron is driven by the potential gradient to interface, then through the TiO_2 film to reach the surface.

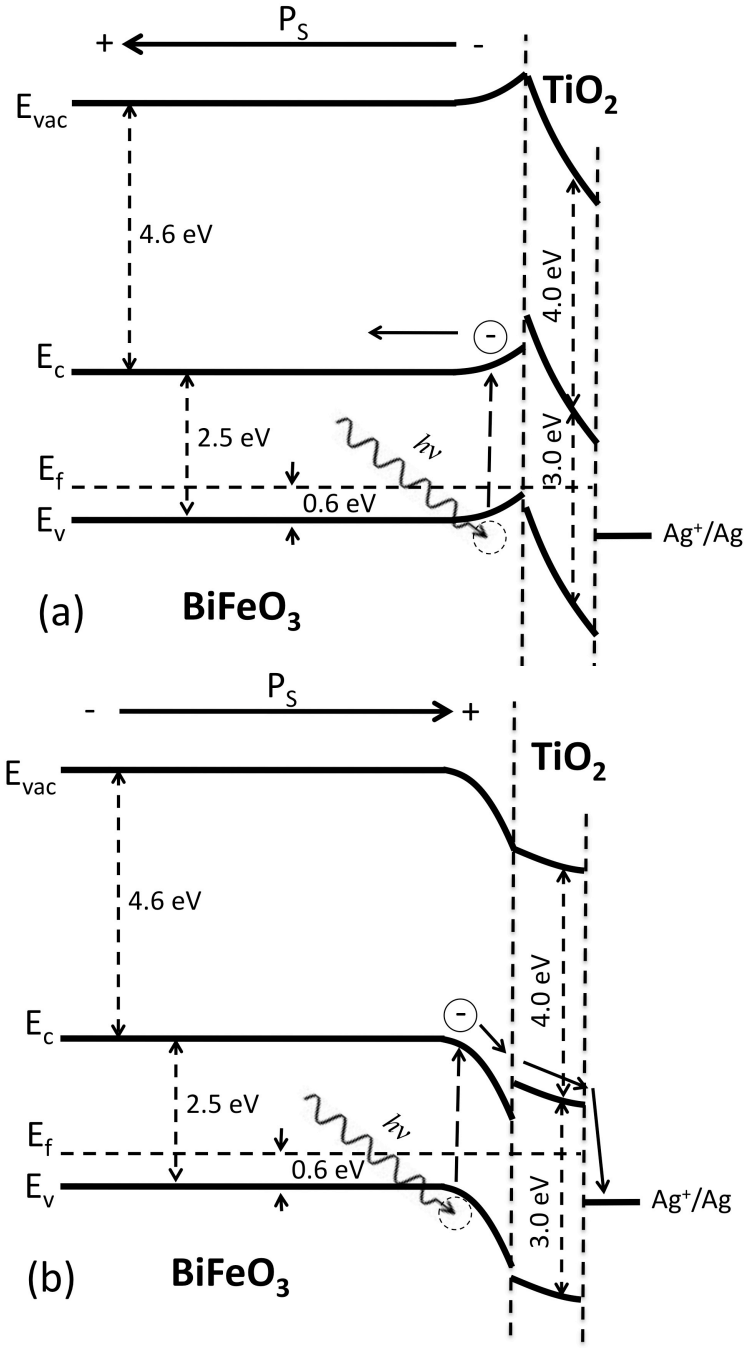

Figure 2.11 The energy level diagrams of a $BiFeO_3$ substrate and a TiO_2 film in contact with solution in the case of (a) negative domain and (b) positive domain. The bands at the $TiO_2/BiFeO_3$ interface bend upward in (a) and downward in (b) corresponding to the P_s. A photon with sufficient energy *hv* excites an electron in the $BiFeO_3$ valence band near the interface. The excited electron in (a) is repelled from the interface. The excited electron in (b) is driven to the interface, then through the film to the surface.

2.3.2.3 Photochemical reactions on ferroelectric domains

The final step in a photocatalytic process is the photochemical reaction. In a negative domain, electrons are forced into the interior of the $BiFeO_3$ substrate, and hence the Ag^+ reduction reaction is prohibited. On the contrary in a positive domain, electrons are driven to the surface of the TiO_2 film, where they participate in the Ag^+ reduction reaction. Ag^+ reduction reaction takes place only on positive domains in this model. This is tested in the current work.

2.3.3 Anisotropic photocatalytic activity

Anisotropic photocatalytic activity is an important issue in studying a crystalline photocatalyst. In the previous work, whether the activity of $TiO_2/BaTiO_3$ is dependent on the phase and the orientation of the TiO_2 surface planes was studied.[42] It was concluded that the photocatalytic activity of $TiO_2/BaTiO_3$ is independent of the phase and orientation of the TiO_2 film, even though the photocatalytic activity of both materials are anisotropic.[36,62-67] Because $BiFeO_3$ is different from $BaTiO_3$ in many aspects, it cannot be concluded a priori that $TiO_2/BiFeO_3$ heterostructures behave as $TiO_2/BaTiO_3$ in terms of photocatalytic activity. Whether the photocatalytic activity of the $TiO_2/BiFeO_3$ heterostructure is dependent on the phase and orientation of the TiO_2 film requires a careful examination. The anisotropic photocatalytic activity of TiO_2 and some perovskites are reviewed here.

2.3.3.1 Anisotropic photocatalytic activity of TiO_2

TiO_2 is known to exhibit anisotropy in its photochemical process.[63-67] An example is given in Fig. 2.12,[65] which is an AFM topographic image showing a TiO_2 surface after photochemical deposition of silver, appearing as white dots. It is clear that some grains on the TiO_2 surface have more photochemically reduced Ag (appeared as white contrast) than other grains. When Ag is photochemically reduced on rutile TiO_2, the most reactive planes are {101}, the moderate ones are {111} and {001}, and the least reactive ones are {110} and {100}.[63,65] Hotsenpiller *et al*. suggest that a number of factors, including surface areas, Ti site densities, surface chemistries, dielectric constants, space charge potentials, carrier mobilities, and ion diffusivities, all imply higher reactivity for {001} surfaces than {100} surfaces.[63] However, one report by Ohno *et al*.[66] indicates that when Pt is reduced on rutile, {110} planes are the most reactive. They suggest that it is due to the synergistic effect of reduction on {110} and oxidation on {011}. Another report by Kobayashi *et al*.[64] shows that on TiO_2 nanowhiskers rutile {110} planes are more reactive than {001} in decomposition of oxalic acid, which is an oxidation reaction. For anatase, more reduced Pt particles were observed on {001} planes than on {101} planes.[66] The dependence of photocatalytic activity on orientation and phase of TiO_2 film supported on $BiFeO_3$ will be checked in the current work.

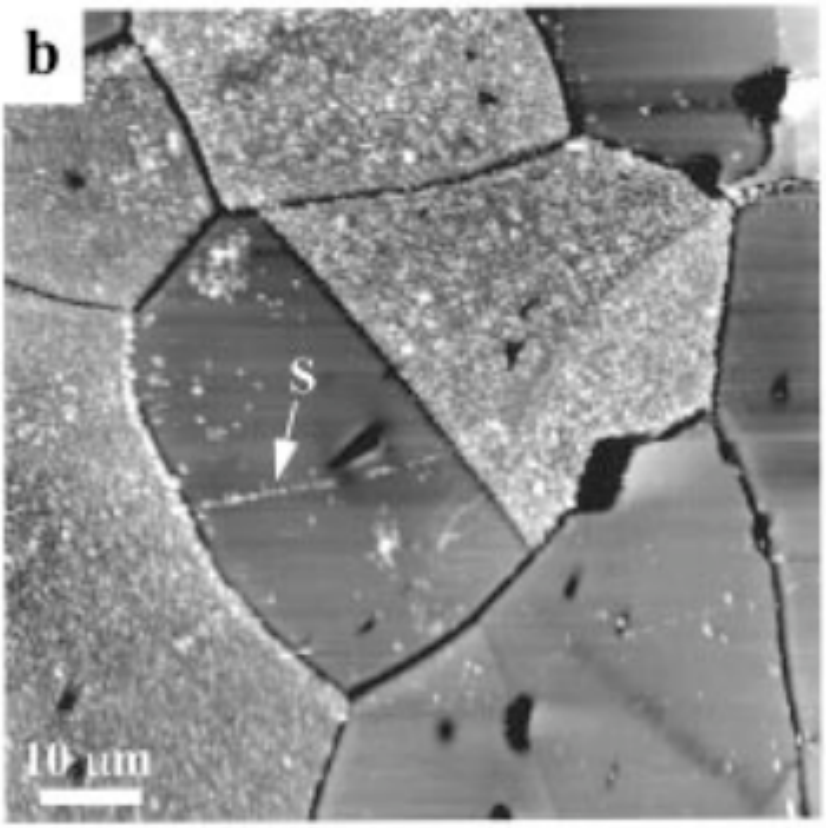

Figure 2.12 AFM image of a thermally etched TiO_2 surface after the photochemical decomposition of silver.[65] The white dots indicate silver particles on the surface. The symbol S indicates a polishing scratch.

2.3.3.2 Anisotropic photocatalytic activity of perovskites

Certain perovskites also exhibit anisotropic photocatalytic activity. It is reported by Giocondi *et al*.[68] that both reduction and oxidation are preferred on {100} planes in $SrTiO_3$. Another previous work by Giocondi *et al*.[62] indicates that the relative reactivity of the $BaTiO_3$ faces can be ranked {100} > {111} > {110}. Fig. 2.13 shows a faceted $BaTiO_3$ crystal after reaction in aqueous $AgNO_3$ solution. Three faces are marked with (100), (111), and (110). The face with the most Ag is (100) and the face with the least Ag is (110). However, the influence from its crystalline orientations is outweighed by the influence from its ferroelectricity.[36] The work by Burbure *et al*.[42] indicates that the photochemical activity of the $TiO_2/BaTiO_3$

heterostructure is approximately the same for anatase (001), rutile (100), and rutile (110) films.

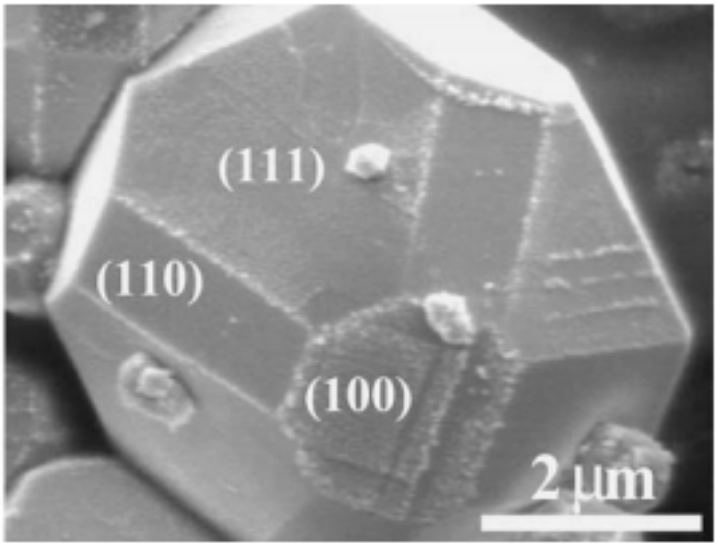

Figure 2.13 SEM image of faceted $BaTiO_3$ crystals after reaction in aqueous $AgNO_3$. The speckled white contrast corresponds to reduced Ag particles. In the three marked faces, the one with the most Ag is (100), and the one with the least Ag is (110).[62]

2.3.3.3 Epitaxial relationships of TiO_2 and $BiFeO_3$

In examining the dependence of photocatalytic activity on the orientation/phase of TiO_2, a practical difficulty of determining the orientation and phase of the thin TiO_2 film is encountered. The orientation imaging microscope (OIM) cannot determine the orientation and phase of grains in the 10 nm TiO_2 film used for this study with sufficient precision because it collects information from interaction volumes usually much deeper than 10 nm.[69-71] By establishing the epitaxial relationships of thick TiO_2 grown on $BiFeO_3$, the orientation and phase of thin TiO_2 films can be deduced from the orientation of the underlying $BiFeO_3$ substrate.

There are a number of TiO_2 films grown on perovskite substrates in the literature.[72-83] For example, anatase TiO_2 is grown on $BaTiO_3$ (BTO) according to the epitaxial relationship $(001)_A||(001)_{BTO}$ and $[100]_A||[100]_{BTO}$.[72] (Here A stands for anatase.) In fact, when anatase is epitaxially grown on perovskite (P) substrates, including $BaTiO_3$ (a = 3.992 Å[81]), $SrTiO_3$ (a = 3.905 Å[81]) and $LaAlO_3$ (a = 3.790 Å[76]), $(001)_A||(001)_P$ and $[100]_A||[100]_P$ is a commonly observed epitaxial relationship.[72-75,77,78,82,83] This relationship is generally ascribed to the nearly identical atomic arrangement in anatase TiO_2 (001) planes (a = 3.785 Å)[84] and perovskite ABO_3 (100) planes. Note that the lattice constant of $BiFeO_3$ (a = 3.962 Å)[27] is very close to these other perovskites. (100) rutile is favorably grown on (111) perovskites,[72,79,80] which is also ascribed to the close atomic matching between the two planes, where both have oxygen atoms arranged in near close packed patterns: O-O distances are 2.779/2.958 Å in rutile (100), 2.761 Å in $SrTiO_3$ (111), and 2.823 Å in $BaTiO_3$ (111). The oxygen separation in the (111) plane of $BiFeO_3$ is 2.802 Å, which is consistent with these other perovskites. Therefore, both anatase/$BiFeO_3$ and rutile/$BiFeO_3$ are expected to exhibit epitaxial relationships consistent with these TiO_2/perovskites.

References:

[1]A. Fujishima and K. Honda, "Electrochemical Photolysis of Water at a Semiconductor Electrode," *Nature*, **238**[5358] 37-38 (1972).

[2]S. R. Morrison, "Electrochemistry at Semiconductor and Oxidized Metal Electrodes," *Plenum Press, New York* (1980).

[3]T. Kawai and T. Sakata, "Photocatalytic Decomposition of Gaseous Water over TiO_2 and TiO_2-RuO_2 Surfaces," *Chem. Phys. Lett.*, **72**[1] 87-89 (1980).

[4]H. Tang, H. Berger, P. E. Schmid, and F. Levy, "Optical-Properties of Anatase (TiO_2)," *Solid State Commun.*, **92**[3] 267-71 (1994).

[5]H. Tang, F. Levy, H. Berger, and P. E. Schmid, "Urbach Tail of Anatase TiO_2," *Phys. Rev. B*, **52**[11] 7771-74 (1995).

[6]R. G. Breckenridge and W. R. Hosler, "Electrical Properties of Titanium Dioxide Semiconductors," *Phys. Rev.*, **91**[4] 793-802 (1953).
[7]J. Pascual, J. Camassel, and H. Mathieu, "Fine-Structure in the Intrinsic Absorption-Edge of TiO_2," *Phys. Rev. B*, **18**[10] 5606-14 (1978).
[8]A. J. Bard, R. Parsons, and J. Jordan, *Standard Potentials in Aqueous Solution* (Marcel Dekker, New York, 1985).
[9]M. Gratzel, "Photoelectrochemical cells," *Nature*, **414**[6861] 338-44 (2001).
[10]S. Sato and J. M. White, "Photo-Decomposition of Water over p-TiO_2 Catalysts," *Chem. Phys. Lett.*, **72**[1] 83-86 (1980).
[11]R. Asahi, T. Morikawa, T. Ohwaki, K. Aoki, and Y. Taga, "Visible-Light Photocatalysis in Nitrogen-Doped Titanium Oxides," *Science*, **293**[5528] 269-71 (2001).
[12]X. B. Chen and C. Burda, "The Electronic Origin of the Visible-Light Absorption Properties of C-, N- and S-doped TiO_2 Nanomaterials," *J. Am. Chem. Soc.*, **130**[15] 5018-19 (2008).
[13]J. L. Gole, J. D. Stout, C. Burda, Y. B. Lou, and X. B. Chen, "Highly Efficient Formation of Visible Light Tunable $TiO_{2-x}N_x$ Photocatalysts and their Transformation at the Nanoscale," *J. Phys. Chem. B*, **108**[4] 1230-40 (2004).
[14]T. Morikawa, R. Asahi, T. Ohwaki, K. Aoki, and Y. Taga, "Band-Gap Narrowing of Titanium Dioxide by Nitrogen Doping," *Jpn. J. Appl. Phys.*, **40** L561-63 (2001).
[15]R. Nakamura, T. Tanaka, and Y. Nakato, "Mechanism for Visible Light Responses in Anodic Photocurrents at N-doped TiO_2 Film Electrodes," *J. Phys. Chem. B*, **108**[30] 10617-20 (2004).
[16]K. Nishijima, B. Ohtani, X. L. Yan, T. Kamai, T. Chiyoya, T. Tsubota, N. Murakami, and T. Ohno, "Incident Light Dependence for Photocatalytic Degradation of Acetaldehyde and Acetic Acid on S-doped and N-doped TiO_2 Photocatalysts," *Chem. Phys.*, **339**[1-3] 64-72 (2007).
[17]Y. Sakatani, J. Nunoshige, H. Ando, K. Okusako, H. Koike, T. Takata, J. N. Kondo, M. Hara, and K. Domen, "Photocatalytic Decomposition of Acetaldehyde under Visible Light Irradiation over La^{3+} and N co-doped TiO_2," *Chem. Lett.*, **32**[12] 1156-57 (2003).
[18]S. Sakthivel, M. Janczarek, and H. Kisch, "Visible Light Activity and Photoelectrochemical Properties of Nitrogen-Doped TiO_2," *J. Phys. Chem. B*, **108**[50] 19384-87 (2004).
[19]V. Stengl and S. Bakardjieva, "Molybdenum-Doped Anatase and Its Extraordinary Photocatalytic Activity in the Degradation of Orange II in the UV and vis Regions," *J. Phys. Chem. C*, **114**[45] 19308-17 (2010).
[20]W. J. Youngblood, S. H. A. Lee, K. Maeda, and T. E. Mallouk, "Visible Light Water Splitting Using Dye-Sensitized Oxide Semiconductors," *Acc. Chem. Res.*, **42**[12] 1966-73 (2009).
[21]B. Oregan and M. Gratzel, "A Low-Cost, High-Efficiency Solar-Cell Based on Dye-Sensitized Colloidal TiO_2 Films," *Nature*, **353**[6346] 737-40 (1991).
[22]F. Sauvage, D. H. Chen, P. Comte, F. Z. Huang, L. P. Heiniger, Y. B. Cheng, R. A. Caruso, and M. Graetzel, "Dye-Sensitized Solar Cells Employing a Single Film of Mesoporous TiO_2 Beads Achieve Power Conversion Efficiencies Over 10%," *ACS Nano*, **4**[8] 4420-25 (2010).

[23]J. Joo, S. G. Kwon, T. Yu, M. Cho, J. Lee, J. Yoon, and T. Hyeon, "Large-Scale Synthesis of TiO_2 Nanorods via Nonhydrolytic Sol-Gel Ester Elimination Reaction and Their Application to Photocatalytic Inactivation of E. coli," *J. Phys. Chem. B*, **109**[32] 15297-302 (2005).

[24]X. H. Wang, J. G. Li, H. Kamiyama, Y. Moriyoshi, and T. Ishigaki, "Wavelength-Sensitive Photocatalytic Degradation of Methyl Orange in Aqueous Suspension over Iron(III)-Doped TiO_2 Nanopowders under UV and Visible Light Irradiation," *J. Phys. Chem. B*, **110**[13] 6804-09 (2006).

[25]X. T. Hong, Z. P. Wang, W. M. Cai, F. Lu, J. Zhang, Y. Z. Yang, N. Ma, and Y. J. Liu, "Visible-Light-Activated Nanoparticle Photocatalyst of Iodine-Doped Titanium Dioxide," *Chem. Mater.*, **17**[6] 1548-52 (2005).

[26]F. Kubel and H. Schmid, "Structure of a Ferroelectric and Ferroelastic Monodomain Crystal of the Perovskite $BiFeO_3$," *Acta Crystallogr. B*, **46** 698-702 (1990).

[27]W. B. Pearson, J. Trotter, B. Beagly, E. Banks, and C. E. Nordman, *Structure Reports*, Vol. 28 (Oosthoek, Scheltema & Holkema, Utrecht, 1963).

[28]J. R. Teague, R. Gerson, and W. J. James, "Dielectric Hysteresis in Single Crystal $BiFeO_3$," *Solid State Commun.*, **8**[13] 1073-74 (1970).

[29]V. V. Shvartsman, "Large Bulk Polarization and Regular Domain Structure in Ceramic $BiFeO_3$," *Appl. Phys. Lett.*, **90**[17] 172115 (2007).

[30]F. Zavaliche, "Polarization Switching in Epitaxial $BiFeO_3$ films," *Appl. Phys. Lett.*, **87**[25] 252902 (2005).

[31]S. H. Baek, C. M. Folkman, J. W. Park, S. H. Lee, C. W. Bark, T. Tybell, and C. B. Eom, "The Nature of Polarization Fatigue in $BiFeO_3$," *Adv. Mater.*, **23**[14] 1621-25 (2011).

[32]A. M. Schultz, Y. L. Zhang, P. A. Salvador, and G. S. Rohrer, "Effect of Crystal and Domain Orientation on the Visible-Light Photochemical Reduction of Ag on $BiFeO_3$," *ACS Appl. Mater. Inter.*, **3**[5] 1562-67 (2011).

[33]F. S. Chen, "Optically Induced Change of Refractive Indices in $LiNbO_3$ and $LiTaO_3$," *J. Appl. Phys.*, **40**[8] 3389-96 (1969).

[34]S. Dunn, P. M. Jones, and D. E. Gallardo, "Photochemical Growth of Silver Nanoparticles on c^- and c^+ Domains on Lead Zirconate Titanate Thin Films," *J. Am. Chem. Soc.*, **129**[28] 8724-28 (2007).

[35]J. L. Giocondi and G. S. Rohrer, "Spatial Separation of Photochemical Oxidation and Reduction Reactions on the Surface of Ferroelectric $BaTiO_3$," *J. Phys. Chem. B*, **105**[35] 8275-77 (2001).

[36]J. L. Giocondi and G. S. Rohrer, "Spatially Selective Photochemical Reduction of Silver on the Surface of Ferroelectric Barium Titanate," *Chem. Mater.*, **13**[2] 241-42 (2001).

[37]P. M. Jones, D. E. Gallardo, and S. Dunn, "Photochemical Investigation of a Polarizable Semiconductor, Lead-Zirconate-Titanate," *Chem. Mater.*, **20**[18] 5901-06 (2008).

[38]S. V. Kalinin, D. A. Bonnell, T. Alvarez, X. Lei, Z. Hu, J. H. Ferris, Q. Zhang, and S. Dunn, "Atomic Polarization and Local Reactivity on Ferroelectric Surfaces: A New Route Toward Complex Nanostructures," *Nano Lett.*, **2**[6] 589-93 (2002).

[39]N. V. Burbure, "Influence of Ferroelectric Substrates on the Photochemical Reactivity of Titanium Dioxide Thin Films," *PhD Thesis* (2009).
[40]N. V. Burbure, P. A. Salvador, and G. S. Rohrer, "Influence of Dipolar Fields on the Photochemical Reactivity of Thin Titania Films on $BaTiO_3$ Substrates," *J. Am. Ceram. Soc.*, **89**[9] 2943-45 (2006).
[41]N. V. Burbure, P. A. Salvador, and G. S. Rohrer, "Photochemical Reactivity of Titania Films on $BaTiO_3$ Substrates: Origin of Spatial Selectivity," *Chem. Mater.*, **22**[21] 5823-30 (2010).
[42]N. V. Burbure, P. A. Salvador, and G. S. Rohrer, "Photochemical Reactivity of Titania Films on $BaTiO_3$ Substrates: Influence of Titania Phase and Orientation," *Chem. Mater.*, **22**[21] 5831-37 (2010).
[43]S. H. Wemple, "Polarization Fluctuations and Optical Absorption Edge in $BaTiO_3$," *Phys. Rev. B*, **2**[7] 2679-89 (1970).
[44]L. Hafid, G. Godefroy, A. Elidrissi, and F. Michelcalendini, "Absorption-Spectrum in the Near UV and Electronic Structure of Pure Barium Titanate," *Solid State Commun.*, **66**[8] 841-45 (1988).
[45]S. R. Basu, "Photoconductivity in $BiFeO_3$ Thin Films," *Appl. Phys. Lett.*, **92**[9] 091905 (2008).
[46]T. Choi, S. Lee, Y. J. Choi, V. Kiryukhin, and S.-W. Cheong, "Switchable Ferroelectric Diode and Photovoltaic Effect in $BiFeO_3$," *Science*, **324**[5923] 63-66 (2009).
[47]F. Gao, "Preparation and Photoabsorption Characterization of $BiFeO_3$ Nanowires," *Appl. Phys. Lett.*, **89**[10] 102506 (2006).
[48]Z. J. Shen, W. P. Chen, G. L. Yuan, J. M. Liu, Y. Wang, and H. L. W. Chan, "Hydrogen-Induced Degradation in Multiferroic $BiFeO_3$ Ceramics," *Mater. Lett.*, **61**[22] 4354-57 (2007).
[49]R. Q. Guo, L. Fang, W. Dong, F. G. Zheng, and M. R. Shen, "Magnetically Separable $BiFeO_3$ Nanoparticles with a Gamma-Fe_2O_3 Parasitic Phase: Controlled Fabrication and Enhanced Visible-Light Photocatalytic Activity," *J. Mater. Chem.*, **21**[46] 18645-52 (2011).
[50]S. Li, Y. H. Lin, B. P. Zhang, J. F. Li, and C. W. Nan, "$BiFeO_3/TiO_2$ Core-Shell Structured Nanocomposites as Visible-Active Photocatalysts and Their Optical Response Mechanism," *J. Appl. Phys.*, **105**[5] (2009).
[51]L. Forro, O. Chauvet, D. Emin, L. Zuppiroli, H. Berger, and F. Levy, "High-Mobility N-Type Charge-Carriers in Large Single-Crystals of Anatase (TiO_2)," *J. Appl. Phys.*, **75**[1] 633-35 (1994).
[52]A. Imanishi, E. Tsuji, and Y. Nakato, "Dependence of the Work Function of TiO_2 (Rutile) on Crystal Faces, Studied by a Scanning Auger Microprobe," *J. Phys. Chem. C*, **111**[5] 2128-32 (2007).
[53]F. Lenzmann, J. Krueger, S. Burnside, K. Brooks, M. Gratzel, D. Gal, S. Ruhle, and D. Cahen, "Surface Photovoltage Spectroscopy of Dye-Sensitized Solar Cells with TiO_2, Nb_2O_5, and $SrTiO_3$ Nanocrystalline Photoanodes: Indication for Electron Injection from Higher Excited Dye States," *J. Phys. Chem. B*, **105**[27] 6347-52 (2001).
[54]H. Yang, H. M. Luo, H. Wang, I. O. Usov, N. A. Suvorova, M. Jain, D. M. Feldmann, P. C. Dowden, R. F. DePaula, and Q. X. Jia, "Rectifying Current-Voltage

Characteristics of $BiFeO_3$/Nb-Doped $SrTiO_3$ Heterojunction," *Appl. Phys. Lett.*, **92**[10] (2008).
[55]S. Y. Yang, L. W. Martin, S. J. Byrnes, T. E. Conry, S. R. Basu, D. Paran, L. Reichertz, J. Ihlefeld, C. Adamo, A. Melville, Y. H. Chu, C. H. Yang, J. L. Musfeldt, D. G. Schlom, J. W. Ager, and R. Ramesh, "Photovoltaic Effects in $BiFeO_3$," *Appl. Phys. Lett.*, **95**[6] (2009).
[56]S.R.Morrison, "Electrochemistry at Semiconductor and Oxidized Metal Electrodes," *Plenum Press, New York* (1980).
[57]A. J. Bard, "Photoelectrochemistry," *Science*, **207**[4427] 139-44 (1980).
[58]R. F. Pierret, *Semiconductor Device Fundamentals* (Addison-Wesley, 1996).
[59]F. A. Grant, "Properties of Rutile (Titanium Dioxide)," *Rev. Mod. Phys.*, **31**[3] 646-74 (1959).
[60]J. Wang, J. B. Neaton, H. Zheng, V. Nagarajan, S. B. Ogale, B. Liu, D. Viehland, V. Vaithyanathan, D. G. Schlom, U. V. Waghmare, N. A. Spaldin, K. M. Rabe, M. Wuttig, and R. Ramesh, "Epitaxial $BiFeO_3$ Multiferroic Thin Film Heterostructures," *Science*, **299**[5613] 1719-22 (2003).
[61]M. E. Lines and A. M. Glass, *Principles and Applications of Ferroelectrics and Related Materials* (Clarendon Press, Oxford, 1977).
[62]J. L. Giocondi and G. S. Rohrer, "The Influence of the Dipolar Field Effect on the Photochemical Reactivity of $Sr_2Nb_2O_7$ and $BaTiO_3$ Microcrystals," *Top. Catal.*, **49**[1-2] 18-23 (2008).
[63]P. A. M. Hotsenpiller, J. D. Bolt, W. E. Farneth, J. B. Lowekamp, and G. S. Rohrer, "Orientation Dependence of Photochemical Reactions on TiO_2 Surfaces," *J. Phys. Chem. B*, **102**[17] 3216-26 (1998).
[64]M. Kobayashi, V. Petrykin, M. Kakihana, and K. Tomita, "Hydrothermal Synthesis and Photocatalytic Activity of Whisker-Like Rutile-Type Titanium Dioxide," *J. Am. Ceram. Soc.*, **92**[1] S21-S26 (2009).
[65]J. B. Lowekamp, G. S. Rohrer, P. A. M. Hotsenpiller, J. D. Bolt, and W. E. Farneth, "Anisotropic Photochemical Reactivity of Bulk TiO_2 Crystals," *J. Phys. Chem. B*, **102**[38] 7323-27 (1998).
[66]T. Ohno, K. Sarukawa, and M. Matsumura, "Crystal Faces of Rutile and Anatase TiO_2 Particles and Their Roles in Photocatalytic Reactions," *New J. Chem.*, **26**[9] 1167-70 (2002).
[67]T. Taguchi, Y. Saito, K. Sarukawa, T. Ohno, and M. Matsumura, "Formation of New Crystal Faces on TiO_2 Particles by Treatment with Aqueous HF Solution or Hot Sulfuric Acid," *New J. Chem.*, **27**[9] 1304-06 (2003).
[68]J. L. Giocondi, P. A. Salvador, and G. S. Rohrer, "The Origin of Photochemical Anisotropy in $SrTiO_3$," *Top. Catal.*, **44**[4] 529-33 (2007).
[69]D. Chen, J.C. Kuo, and W.T. Wu, "Effect of Microscopic Parameters on EBSD Spatial Resolution," *Ultramicroscopy*, **111** 1488-94 (2011).
[70]T. C. Isabell and V. P. Dravid, "Resolution and Sensitivity of Electron Backscattered Diffraction in a Cold Field Emission Gun SEM," *Ultramicroscopy*, **67**[1-4] 59-68 (1997).
[71]M. M. Nowell, "Ion Beam Preparation of Passivated Copper Integrated Circuit Structures for Electron Backscatter Diffraction/Orientation Imaging Microscopy Analysis," *J. Electron. Mater.*, **31**[1] 23-32 (2002).

[72]N. V. Burbure, P. A. Salvador, and G. S. Rohrer, "Orientation and Phase Relationships between Titania Films and Polycrystalline $BaTiO_3$ Substrates as Determined by Electron Backscatter Diffraction Mapping," *J. Am. Ceram. Soc.*, **93**[9] 2530-33 (2010).
[73]S. Chen, M. G. Mason, H. J. Gysling, G. R. Pazpujalt, T. N. Blanton, T. Castro, K. M. Chen, C. P. Fictorie, W. L. Gladfelter, A. Franciosi, P. I. Cohen, and J. F. Evans, "Ultrahigh-Vacuum Metalorganic Chemical-Vapor-Deposition Growth and in-Situ Characterization of Epitaxial TiO_2 Films," *J. Vac. Sci. Technol. A*, **11**[5] 2419-29 (1993).
[74]H. Du, P. J. Fisher, M. Skowronski, P. A. Salvador, and O. Maksimov, "Growth and Structural Characterization of Epitaxial $Ba_{0.6}Sr_{0.4}TiO_3$ Films Deposited on $REScO_3$(110) (RE = Dy, Gd) Substrates using Pulsed Laser Deposition," *J. Cryst. Growth*, **310**[7-9] 1991-98 (2008).
[75]P. Fisher, O. Maksimov, H. Du, V. D. Heydemann, M. Skowronski, and P. A. Salvador, "Growth, Structure, and Morphology of TiO_2 Films Deposited by Molecular Beam Epitaxy in Pure Ozone Ambients," *Microelectron. J.*, **37**[12] 1493-97 (2006).
[76]S. Geller and V. B. Bala, "Crystallographic Studies of Perovskite-Like Compounds .2. Rare Earth Aluminates," *Acta Crystallogr.*, **9**[11] 1019-25 (1956).
[77]C. C. Hsieh, K. H. Wu, J. Y. Juang, T. M. Uen, J. Y. Lin, and Y. S. Gou, "Monophasic TiO_2 Films Deposited on $SrTiO_3$(100) by Pulsed Laser Ablation," *J. Appl. Phys.*, **92**[5] 2518-23 (2002).
[78]R. J. Kennedy and P. A. Stampe, "The Influence of Lattice Mismatch and Film Thickness on the Growth of TiO_2 on LaAlO3 and $SrTiO_3$ Substrates," *J. Cryst. Growth*, **252**[1-3] 333-42 (2003).
[79]A. Lotnyk, S. Senz, and D. Hesse, "Epitaxial Growth of TiO_2 Thin Films on $SrTiO_3$, $LaAlO_3$ and Yttria-Stabilized Zirconia Substrates by Electron Beam Evaporation," *Thin Solid Films*, **515**[7-8] 3439-47 (2007).
[80]A. Lotnyk, S. Senz, and D. Hesse, "Orientation Relationships of $SrTiO_3$ and $MgTiO_3$ Thin Films Grown by Vapor-Solid Reactions on (100) and (110) TiO_2 (rutile) Single Crystals," *J. Phys. Chem. C*, **111**[17] 6372-79 (2007).
[81]A. Okazaki and M. Kawamina, "Lattice-Constant of Strontium-Titanate at Low-Temperatures," *Mater. Res. Bull.*, **8**[5] 545-50 (1973).
[82]W. Sugimura, T. Yamazaki, H. Shigetani, J. Tanaka, and T. Mitsuhashi, "Anatase-Type TiO_2 Thin Films Produced by Lattice Deformation," *Jpn. J. Appl. Phys. Part 1*, **36**[12A] 7358-59 (1997).
[83]S. Yamamoto, T. Sumita, T. Yamaki, A. Miyashita, and H. Naramoto, "Characterization of Epitaxial TiO_2 Films Prepared by Pulsed Laser Deposition," *J. Cryst. Growth*, **237** 569-73 (2002).
[84]R. W. G. Wyckoff, *Crystal Structures*, Vol. 1, 2nd ed. (John Wiley & Sons, 1963).

Chapter 3 Hypothesis

(1) In the $TiO_2/BiFeO_3$ heterostructure, electrons photogenerated by blue light irradiation migrate under the influence of ferroelectric polarization from the $BiFeO_3$ substrate to the TiO_2 surface, where they participate in the photochemical reduction of Ag^+ in aqueous solution.

Based on the energy level diagram of $TiO_2/BiFeO_3$ in aqueous solution, predicted with knowledge from literature, electrons are expected to behave as described by this hypothesis. Experimental verification of the predicted energy bands would lay the foundation of further study of the dependence of photocatalytic activity on the phase and orientation of TiO_2 film.

(2) The strength of polarization is the dominating factor of photocatalytic activity for the $TiO_2/BiFeO_3$ heterostructure; the phase and orientation of TiO_2 are less important.

Currently, we consider the influence of ferroelectric polarization as the dominating factor of $TiO_2/BiFeO_3$'s photocatalytic activity. The band bending induced by spontaneous polarizations significantly affects the transport of electrons as shown in Fig. 2.13. The strongest downward band bending is thought to occur when the normal of the $BiFeO_3$ surface is in parallel with its polarization vector along [111]. This is thought to be the easiest possible condition for electrons in $BiFeO_3$ to move to the surface. The phase and orientation of TiO_2 film grains plays a less significant role in determining the photocatalytic activity.

(3) Anatase (A) is epitaxially grown on $BiFeO_3$ (BFO) with a relationship of $(112)_A$ || $(111)_{BFO}$ and $[1\bar{1}0]_A$ || $[1\bar{1}0]_{BFO}$. Rutile (R) is epitaxially grown on $BiFeO_3$ with $(100)_R$ || $(111)_{BFO}$.

TiO_2 films are expected to be epitaxially deposited on polycrystalline $BiFeO_3$ substrates in fashions consistent with TiO_2 on other perovskites mentioned in Chapter 2. The understanding of epitaxial relationships provides a means to deduce the phase and orientation of TiO_2 grains in very thin films from $BiFeO_3$ substrates in the study of dependence of photocatalytic activity on phase and orientation of TiO_2.

Chapter 4 Experimental work

In this chapter, the measurement of photocatalytic activity of the $TiO_2/BiFeO_3$ heterostructures and related samples is described. By measuring and comparing the surface topography of a sample, before and after the photochemical reduction of Ag, using the atomic force microscopy (AFM) technique, the photocatalytic activity is quantified relative to the amount of reaction products (measured by height) and qualified relative to the spatial location. Piezoresponse force microscopy (PFM) technique is used to identify the ferroelectric domain structures of a bare $BiFeO_3$ sample and a $TiO_2/BiFeO_3$ sample, which is compared with the spatial pattern of the Ag reaction product to uncover their correlations. The local crystal structure and orientation relationships of TiO_2 and $BiFeO_3$ are determined using electron backscatter diffraction (EBSD) data. The methodology used to determine the orientation relationships will be explained in detail in chapter 7, having been developed in this work while EBSD itself will be described here. The details of sample preparation, the photochemical reaction, and the characterization techniques are described in the following sections.

4.1 Preparation of $TiO_2/BiFeO_3$ and related samples

The substrates of $BiFeO_3$ and other related materials are fabricated as disc-shaped pellets, polished, and deposited with TiO_2 films for the heterostructured samples.

4.1.1 Synthesis of $BiFeO_3$, $BaTiO_3$, and TiO_2 substrate and target pellets

Polycrystalline $BiFeO_3$ pellet substrates are fabricated via a solid state route. First, the $BiFeO_3$ powder was synthesized from Bi_2O_3 (Alfa Aesar 99.99%) and Fe_2O_3 (Alfa Aesar 99.945%) powders.[1,2] According to the phase diagram of Bi_2O_3 and Fe_2O_3 in Fig. 4.1, equimolar amounts of both powders were immersed in ethanol with yttria stabilized zirconia (YSZ) balls in a sealed 500 ml plastic bottle for ball-milling. The YSZ balls are one of the hardest and least porous grinding media that are not likely to contaminate the powders in the process. After ball-milling for 24 h, the slurry in the bottle was dried at 85° either in an oven or on a hot plate for 12 – 24 h. The dried powder mixture was loaded in an Al_2O_3 crucible and was calcined in a furnace at 700 °C for 3 h for the Bi_2O_3 and the Fe_2O_3 to form $BiFeO_3$ through reaction. The heating from room temperature (RT, ~ 25°C) to 700°C was controlled at 10 °C min^{-1}. The X-ray diffraction (XRD) pattern in Fig. 4.2 taken with an X'Pert PRO MPD X-ray Diffractometer (PANalytical, Almelo, Netherlands) indicated that the majority phase was $BiFeO_3$. Small amounts of minority phases were detected, including $Bi_2Fe_4O_9$, $Bi_{25}FeO_{40}$, and Fe_2O_3.

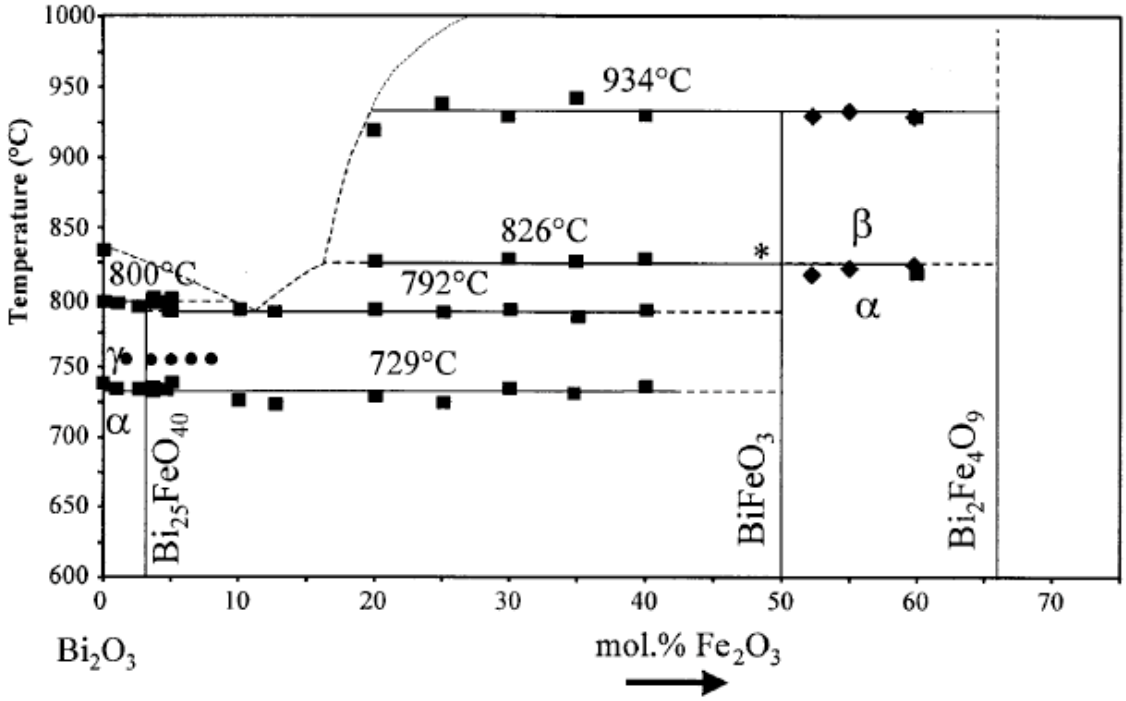

Figure 4.1 Phase diagram of Bi_2O_3 and Fe_2O_3 by Maitre *et al.*[3]

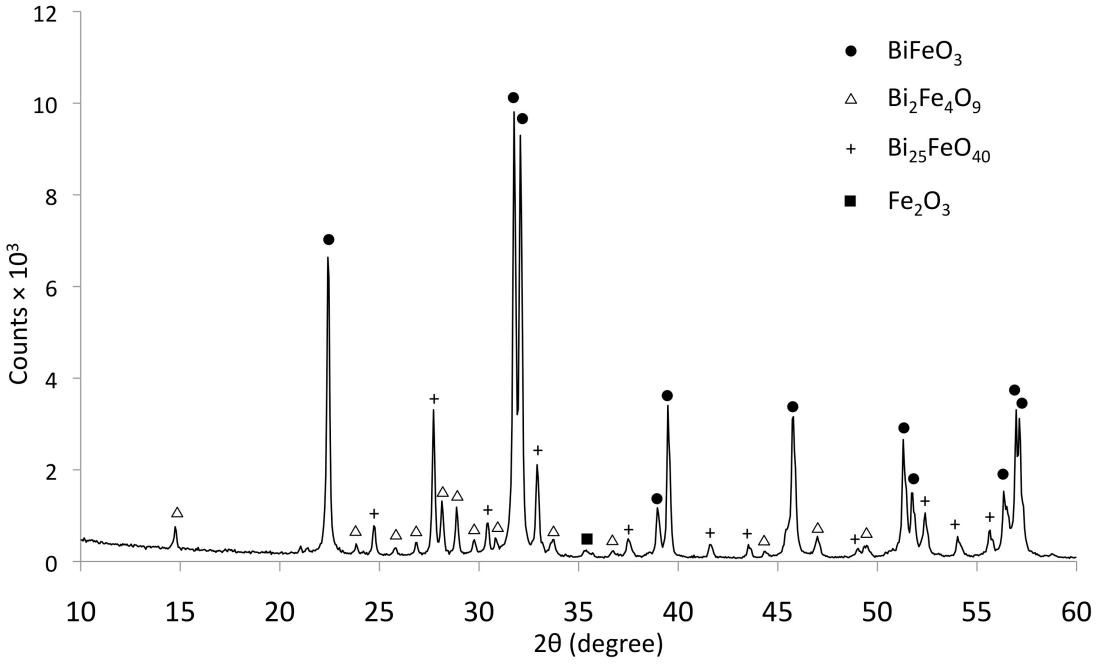

Figure 4.2 XRD pattern of $BiFeO_3$ powder after calcination. The peaks designated by different symbols correspond to different phases according to the legends on the up right corner.

Next, the $BiFeO_3$ powder was compressed to form green pellets. Because the powder grains were coarsened and agglomerated during the calcination step, the $BiFeO_3$ powder was hand ground in a mortar and then ball-milled for another 24 h, using the same procedure as described above to reduce the grain size. After drying at 85°C, the powder was mixed with binder (95% ethanol, Pharmco-AAPER) and compressed uniaxially in a cylindrical die at a load of 105 MPa to form pellets ~ 1 cm in diameter and 1.4 – 3 mm thick. The binder was used to avoid breakage of the green $BiFeO_3$ pellets. Stearic acid (95% purity, Research Chemicals Ltd.) mixed with excessive ethanol (95% purity, Pharmco-AAPER) was used to lubricate the die. The compressed pellets were transferred to a crucible and were immersed in the parent $BiFeO_3$ powder (to prevent contamination from the crucible and the air during the next stage of heating).

The pellet was heated (at 10 °C min^{-1}) to 600°C for 12 h to burn off the binder in the pellet, then (at 5 °C min^{-1}) to 780°C for 12 h for sintering, and (at 5 °C min^{-1}) to 850°C for 3 h for grain growth.[2] Finally, the pellet was step cooled to room temperature.

The pellets were polished using a Logitech autopolisher (Logitech, Glasgow, Scotland). In a typical procedure, a pellet was first lapped flat with an aqueous Al_2O_3 suspension (grain size = 3 or 9 μm, Logitech) for ~ 15 min and then polished with a 0.02 μm colloidal SiO_2 suspension (MasterMet 2, Buehler) for ~ 30 min. Acetone and de-ionized water were used to clean the polished surface after polishing. Each pellet had one surface polished. To repair damage from polishing on the surface, the polished pellets were heated at a rate of 10°C min^{-1} to 600°C for 3 h. X-ray

diffraction at this step is shown in Fig. 4.3 and it indicates that most of the impurity phases have decreased in intensity as compared to right after calcination. Such pellets should be useful in our experiments.

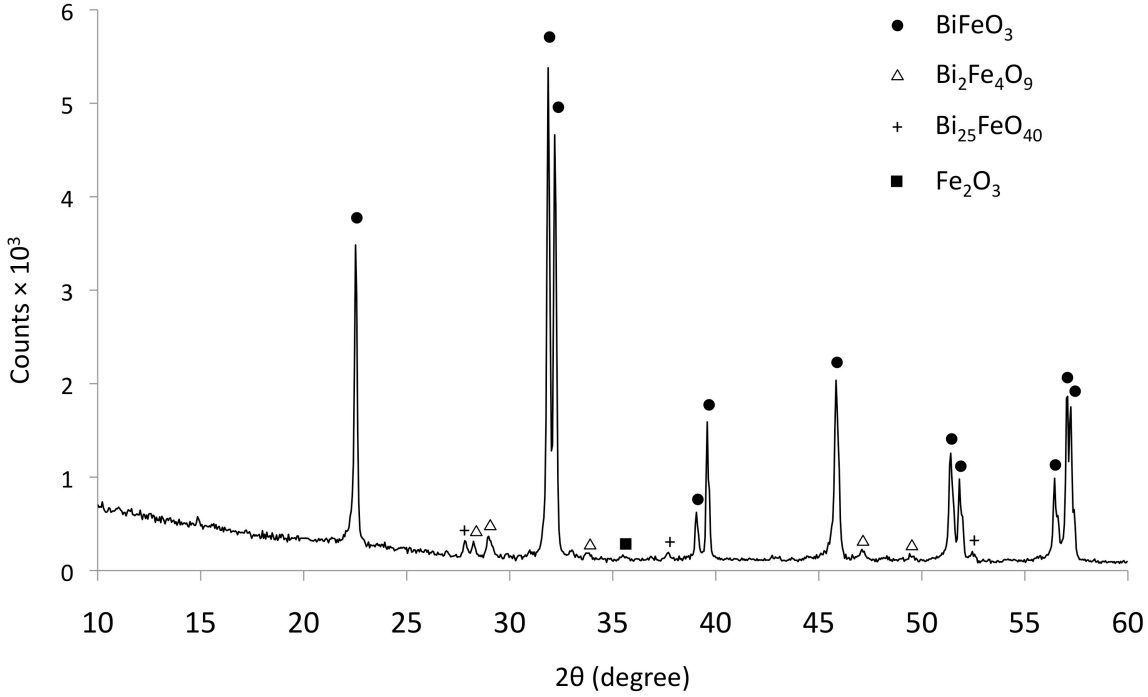

Figure 4.3 XRD pattern of a polished $BiFeO_3$ pellet after annealing. The peaks designated by different symbols correspond to different phases according to the legends.

One pure $BaTiO_3$ substrate, one pure TiO_2 substrate, one pure TiO_2 target (used in PLD as described in section 4.1.2), and one Fe-doped (2 at%) TiO_2 target were synthesized using similar procedures as for $BiFeO_3$. $BaTiO_3$ powder (Alfa Aesar 99.7%) was compressed to form pellets ~ 1 cm in diameter. The sintering procedures for all pellets are given in Table 4.1. The $BaTiO_3$ pellet was polished and then annealed at 1200 °C for 6 h.[4-8] High-purity rutile TiO_2 powder was compressed to form a disc ~ 1 cm in diameter and sintered at 1400 °C for 12 h. The TiO_2 pellet was polished and annealed at 1200 °C for 4 h.[9] Using a 1 inch die, the high-purity

TiO_2 powder and the same powder mixed with Fe_2O_3 powder in molar ratio 98:1 were compressed to form two larger pellets. The sintering procedure was the same as for the TiO_2 substrate. The two pellets were polished using the autopolisher. Table 4.1 summarizes the synthetic steps of each sample mentioned above.

	$BiFeO_3$	$BaTiO_3$	TiO_2	Fe-TiO_2
Calcination	700°C 3h	-	-	-
Hand grinding	Yes	-	-	-
Ball-milling	12 – 24h	-	-	-
Burn off	600°C 12h	900°C 10h	-	-
Sintering	780°C 12h	1230°C 10h	1400°C 12h	1350°C 8h
Grain growth	850°C 3h	1360°C 3h	-	-
Annealing after polishing	600°C 3h	1200°C 6h	-	-

Table 4.1 Summary of synthesis of pellet samples in this work.

4.1.2 PLD of TiO_2 film

Flat TiO_2 films with good crystallinity are grown using PLD technique.[1,4-8] A brief schematic illustration of the PLD setup is in Fig. 4.4. When a pulsed laser comes into the chamber and hits the target surface, a plume of the target material is struck out and directed at the substrate. The atoms in the plume arrive at the substrate, diffuse on the surface at an elevated temperature, and crystallize to form a film.

The deposition condition is adopted with minor adjustments from the work in which TiO_2 films were successfully deposited on polycrystalline $BaTiO_3$ substrates.[4-8] Before deposition, the surface of the substrate was cleaned by sonication in a bath of methanol for 5 – 10 min twice. The substrate was glued on the substrate holder using silver paste heated to 120 °C. The TiO_2 target was

mounted such that the target-to-substrate distance in the deposition chamber was maintained at ~ 6 cm for all the depositions. The chamber was pumped down to ~ 10^{-5} Torr with the substrate at 120 °C. A flow of oxygen was introduced into the chamber to maintain the pressure at 5 mTorr during the following heating and deposition steps. The substrate was heated at a rate of 25 °C min^{-1} to reach a temperature of 500 – 700 °C. This temperature range was tested to be suitable for TiO_2 film crystallization.

During the deposition, a KrF (λ = 248 nm) laser was pulsed at 3 Hz with an energy density of 2 J cm^{-2}. Before the actual deposition, the TiO_2 target was cleaned and conditioned by laser ablation for 10 min (1800 pulses at 3 Hz). A TiO_2 film is deposited on the substrate with its thickness determined by the number of laser pulses. The deposition rate of TiO_2 was ~ 0.0067 nm per pulse, which was pre-determined by depositing a TiO_2 film on a $LaAlO_3$ single crystal using 3000 laser pulses and measuring its thickness using the X-ray reflectivity technique.[10,11] After deposition, the chamber was cooled at a rate of 25 °C min^{-1} to reach room temperature ~ 25 °C) in a stagnant oxygen atmosphere with a pressure of 5 Torr. Table 4.2 summarizes the deposited films in this work.

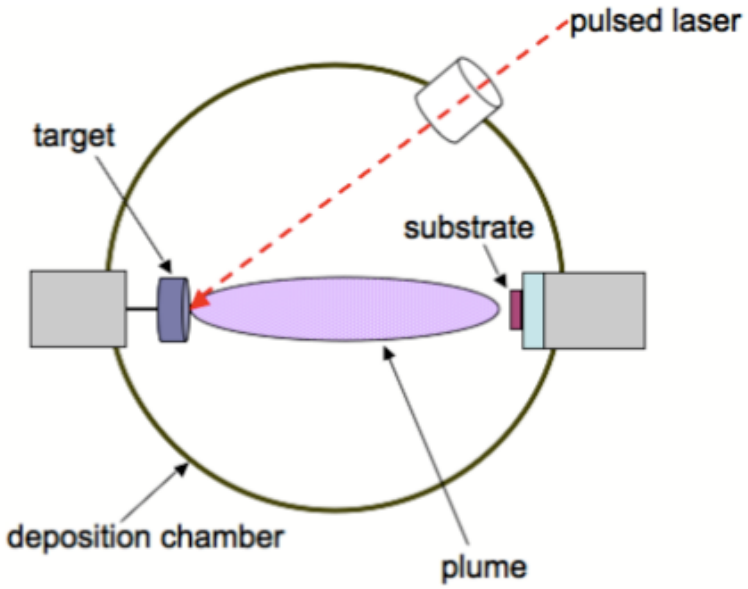

Figure 4.4 Schematic Schematic of PLD setup. A pulsed laser ablates the surface of a target (composed of the film material) and a plume of ablated material is directed towards the surface of the substrate, which is heated to a certain temperature. Adapted from ref.[4]

Substrate	Film	Thickness (nm)
$BiFeO_3$	TiO_2	10
$BiFeO_3$	TiO_2	20
$BiFeO_3$	TiO_2	80
$SrTiO_3$ (100)	TiO_2	20
$SrTiO_3$ (100)	Fe-doped TiO_2	10
$BaTiO_3$	TiO_2	20
$BiFeO_3$	TiO_2	100

Table 4.2 Prepared film/substrate samples.

4.2 Photochemical reaction setup: reduction of Ag^+ in solution

The photochemical reduction of Ag^+ from $AgNO_3$ solution deposits Ag particles as the products on the surfaces of the samples. The Ag particles can be detected during an AFM topographic scan (described in section 4.3.1) and

topographic information can be used as a quantitative measurement of the photocatalytic activity of the samples.

The setup of the photochemical reaction is depicted in Fig. 4.5. In a typical procedure, a 0.115 M $AgNO_3$ solution was prepared by dissolving appropriate amount of $AgNO_3$ crystallites in 50 mL of de-ionized water in a beaker. A viton O-ring was placed on a disc-shaped pellet. The $AgNO_3$ solution was added to fill the space bound by the O-ring and the sample surface. A quartz slip was placed on top of the O-ring to seal the space and was held by the surface tension of the liquid. A blue LED with emission energy of 2.53 – 2.70 eV (LUXEON, Philips Lumileds, San Jose, CA) was plugged to an external power source and held in a fixed position with its lens facing downward. The reaction assembly was brought as close as possible to the lens of the blue LED. The LED was switched on at 750 mA for 60 s or at 100 mA for 20 min in different experiments.

After the LED was switched off, the quartz slip and the O-ring were removed from the sample. The sample was rinsed by sequential immersion in two baths of de-ionized water to dilute the remnant solution adhered on the surface. After rinsing, a stream of clean nitrogen was directed at the surface to blow dry the remaining liquid. The reacted sample surface was ready to be examined by AFM. It was confirmed that the reaction product was metallic Ag by scanning the surface of a $BiFeO_3$ sample reacted for several hours (to increase the total amount of reaction product) with XRD.

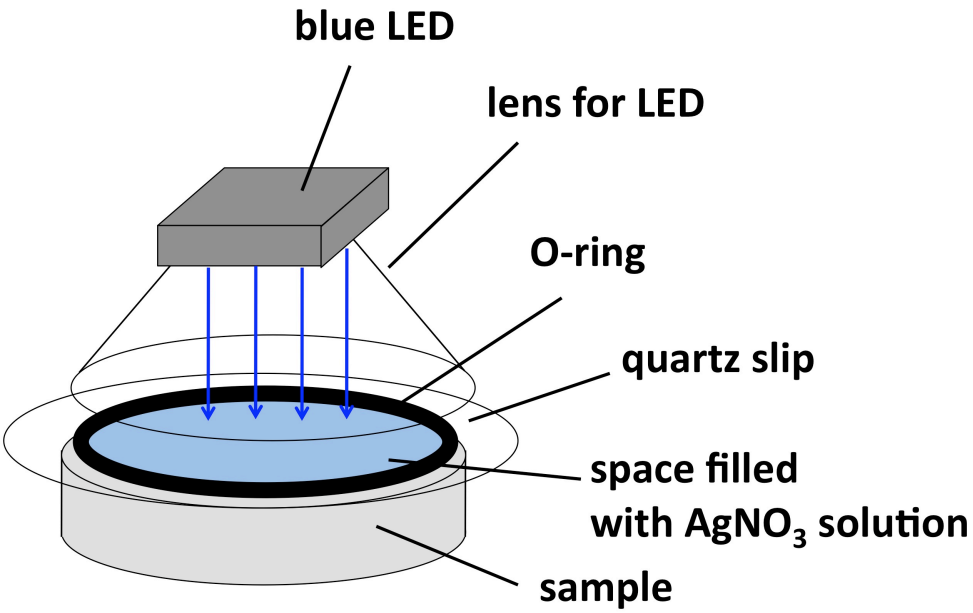

Figure 4.5 Schematic of the reaction setup. Parts of the assembly are labeled and explained in section 4.2. The blue light emitted from the LED goes through the lens, the quartz slip, and the $AgNO_3$ solution to reach the sample.

4.3 Methods of characterization

4.3.1 Measurement of photocatalytic activity with AFM

Measurement of photocatalytic activity using AFM in the present work is presented in this section. The photocatalytic activity of a local grain on the surface of a pellet is measured for the amount of reduced Ag particles. When Ag particles are deposited on the surface, the topography of the surface is changed. As the surface region with reduced Ag particles is "heightened" by those particles, bright contrast in the AFM topographic image appears in that region after reaction as compared to the image of the clean surface before reaction.

An example from previous work[7] is given in Fig. 4.6. The image in Fig. 4.6(a) shows the clean surface of a (110)-oriented rutile TiO_2 grain. The image in Fig.

4.6(b) shows the surface of the same grain (as can be located by tracing the grain boundary in the lower left corner) after conducting the Ag reduction reaction for 15 s using UV light.[7] From the comparison of these two images, it is obvious that stripes of bright contrasts in a near vertical direction appear after the photochemical reaction. Those bright contrasts are attributed to the reduced Ag particles, distributed in a spatially distinctive pattern. In measuring the amount of the Ag particles, the height profiles of a same location, indicated by the blue and the red lines in Fig. 4.6(a,b), are extracted from the AFM data and presented in the plot in Fig. 4.6(c). In the plot, the red (blue) line represents the after (before) reaction height profile. They are aligned by locating the valley of the grain boundary on the left. The spiked features in the red line correspond to the bright contrasts in (b), which are the indication of Ag particles. By subtracting the blue profile from the red profile, the actual heights, or thicknesses, of the reduced Ag particles are obtained. In this example, the heights of the Ag particles are mainly in the range of 75 to 125 nm. This range value is considered as a quantitative measurement of the photocatalytic activity of that grain.

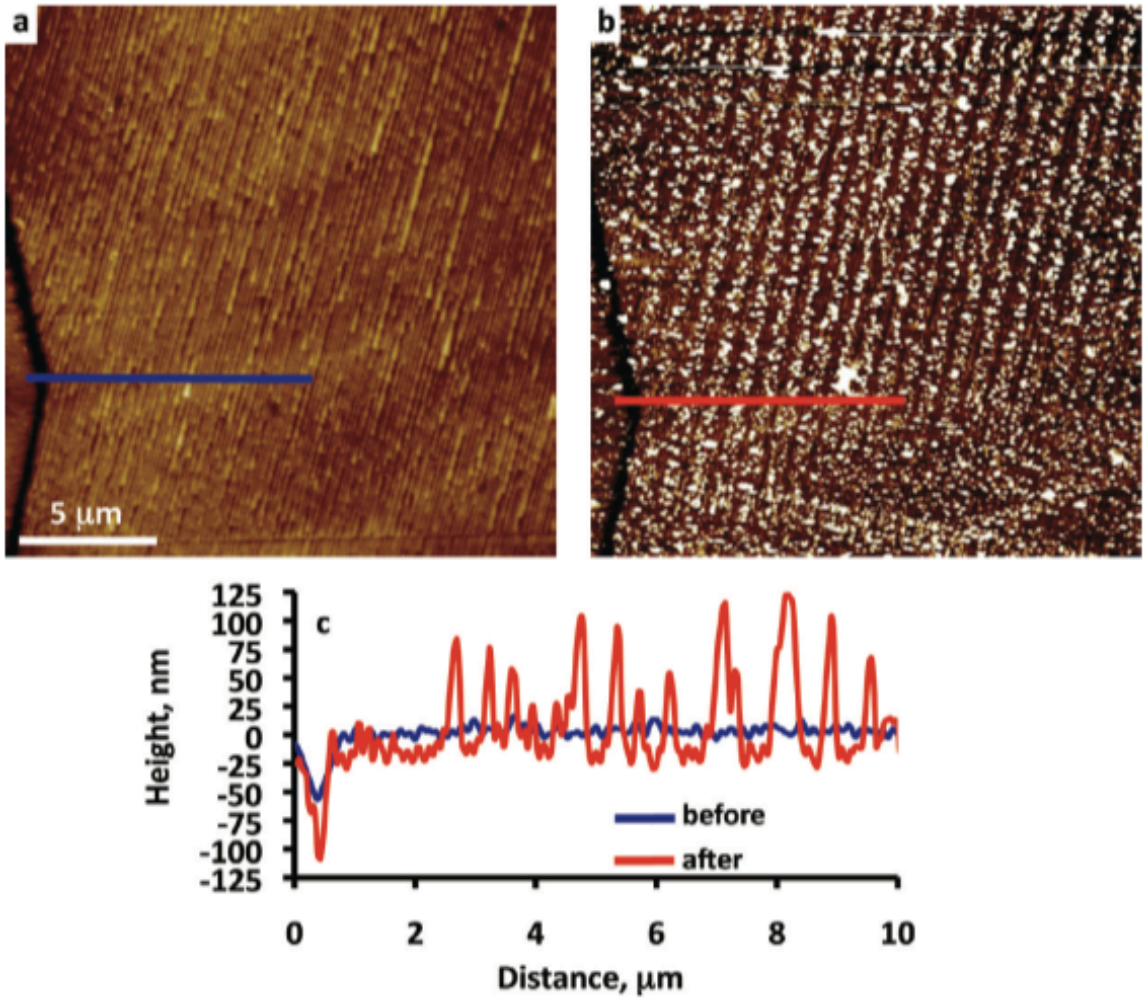

Figure 4.6 AFM topographic images of the same location on the surface of a 15 nm thick (110)-oriented rutile TiO_2 surface supported by (110) oriented $BaTiO_3$ before (a) and after (b) a photochemical reaction in aqueous $AgNO_3$ solution. The black-to-white contrast is 80 nm in (a) and 90 nm in (b). Panel (c) shows the heights of features along the blue line in (a) and the red line in (b). Adapted from ref.[7]

In chapter 5, the measured heights of reduced Ag particles on TiO_2 film of different thicknesses are compared to reveal the influence of film thickness on photocatalytic activity. In chapter 8, the heights of Ag particles on differently oriented grains in the $BiFeO_3$ substrate and in the TiO_2 film are compared to study

the anisotropy in photocatalytic activity. The concept of measurement and comparison of photocatalytic activity is presented in Fig. 4.7.

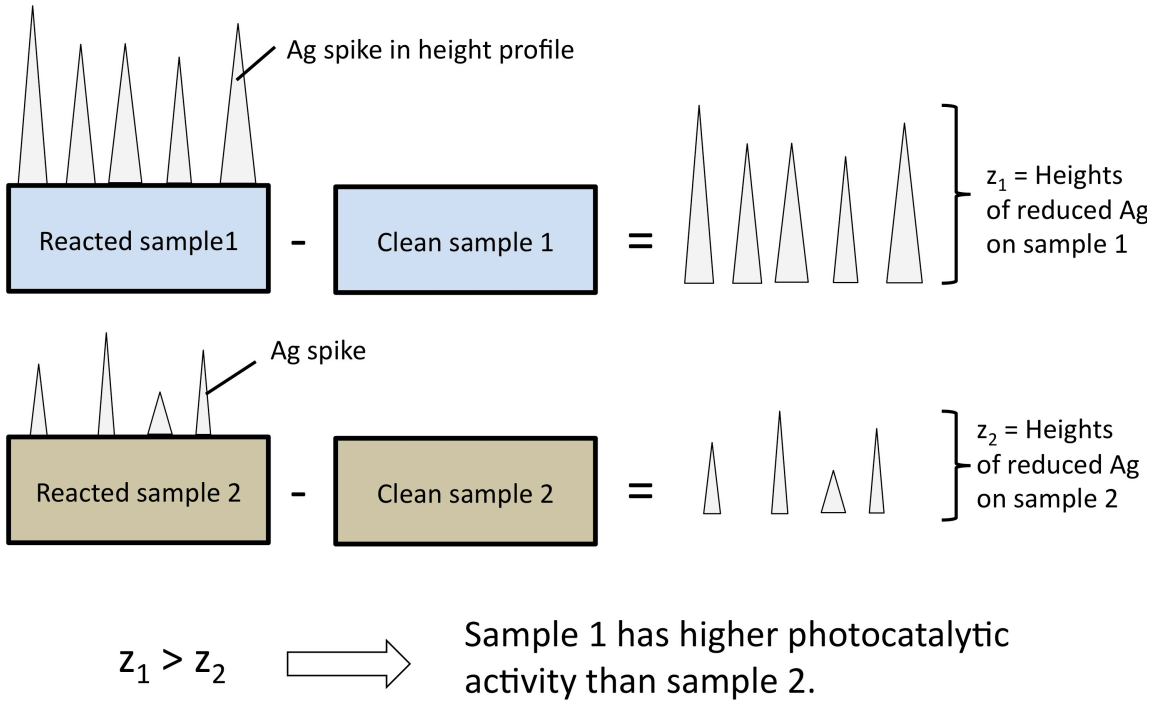

Figure 4.7 Visualized concept of measurement and comparison of photocatalytic activity in this work. The height profile after reaction subtracts the one before reaction renders the height profile of reduced Ag particles. Comparison of the height ranges z_1 and z_2 from two samples shows which sample is more photocatalytically active.

AFM topographic images were taken in the semi-contact mode using either a NTegra (NT-MDT, Santa Clara, CA) microscope, a Solver NEXT (NT-MDT, Santa Clara, CA) microscope, or a Dimension 3100 (Veeco, Plainview, NY) microscope. The probe oscillates at a resonance frequency and intermittently makes brief contact with the surface in this mode. As the tip of the probe gets closer to the surface, its oscillation amplitude decreases. The microscope adjusts the height of the probe to maintain a constant oscillatory amplitude and the change of height is continuously recorded to reflect the surface topography. After scanning, the raw images are

processed, mainly flattened to compensate for the slope from sample mounting, for better presentation.

4.3.2 Imaging ferroelectric domain structures with PFM

The photochemical reaction sites are thought to be directly correlated to the ferroelectric domain structure of the $BiFeO_3$ substrate. By comparison of the pattern of reduced Ag particles to the domain structure, such a correlation can be established.

Piezoresponse force microscopy is a scanning probe technique capable of imaging ferroelectric domain structures. An oscillatory voltage is applied to the tip of the probe, which is in contact with the sample as it scans. The electric field induces a local deformation in the ferroelectric sample, which mechanically oscillates the tip vertically and laterally. Correspondingly, the vertical PFM (VPFM) senses the out-of-plane (OP) responses and the lateral PFM (LPFM) senses the in-plane (IP) responses of the ferroelectric sample.

The imaging mechanisms[12-14] of VPFM and LPFM are illustrated in Fig. 4.8. An oscillatory electric field *E* between the AFM tip and the electrode at the bottom of the ferroelectric sample is created by applying an oscillatory bias to the AFM tip. The local electromechanical response is recorded as the probe scans over the sample surface. For a domain with polarization vector *P* pointing up and left, a positive bias causes a contraction in the z direction of the crystal and a counter-clockwise torque of the tip. The oscillation of the tip is antiphase (180°) with the applied field. Conversely, for a domain with polarization vector pointing down and

right, a positive bias causes an expansion in the z direction and a clockwise torque. The oscillation of the tip is in phase (0°) with the applied field. The applied bias voltage can be expressed as:

$$V_{tip} = V_{DC} + V_{AC}\cos(\omega t) \qquad \text{Eqn (1),}$$

where V_{tip} = bias voltage on the tip,

V_{DC} = DC bias voltage,

V_{AC} = AC bias voltage, and

ω = frequency of oscillation for AC bias.

The response can be expressed as:

$$A = A_0 + A_\omega \cos(\omega t + \varphi) \qquad \text{Eqn (2),}$$

where A = total surface displacement,

A_0 = static surface displacement,

A_ω = oscillatory surface displacement,

ω = frequency of oscillatory displacement, and

φ = phase lag between the applied bias and the surface displacement.

Note that due to the dissimilar nature of vertical and lateral PFM responses, the surface displacements A_0 and A_ω are different for VPFM and LPFM.[15]

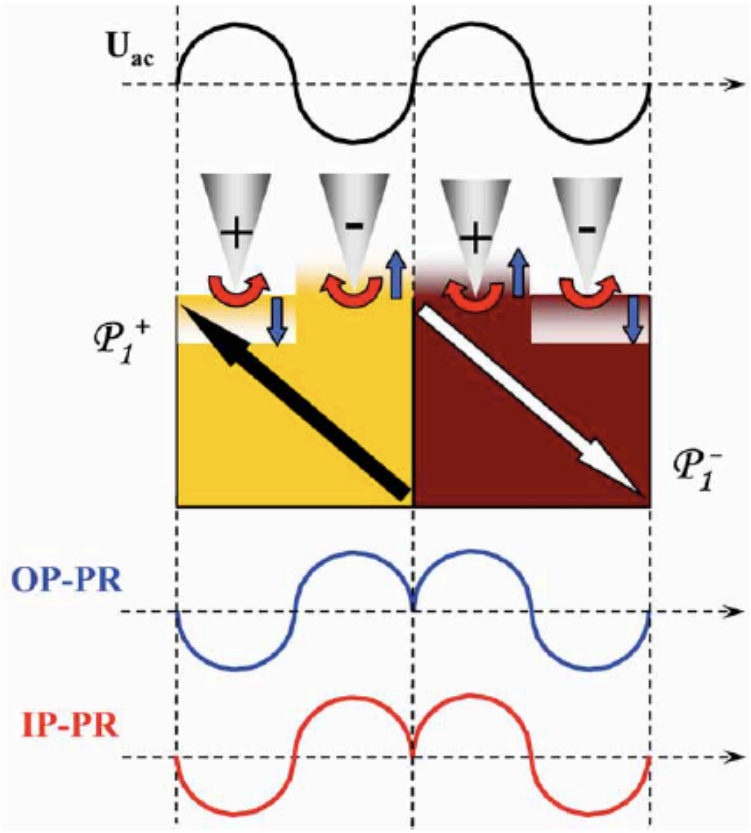

Figure 4.8 A schematic of the out-of-plane and in-plane piezoelectric response from two domains with the polarization vector pointing as shown. The black curve represents the ac bias applied to the tip, and the colored curves stand for the out-of-plane (blue) and in-plane (red) piezoresponses.[13]

In the ideal case, a VPFM phase image has two contrast levels. The contrast level at 0° indicates a local polarization pointing into the surface plane. The other contrast level at 180° indicates a local polarization pointing out of the surface plane. The VPFM magnitude signal can be interpreted as aA_{ω}/V_{AC}, where a is the constant determined by lock-in setting and sensitivity of photodiode. The interpretation of LPFM phase and magnitude responses in the ideal case is very similar.

In reality, the measured piezoresponses involve not only the electromechanical interaction, but also contributions from the electrostatic

interaction and non-local cantilever-surface interaction, according to Kalinin *et al*.[15] The local electromechanical signal can be decomposed in terms of directions with respect to the cantilever as vertical, lateral (in-plane, perpendicular to cantilever), and longitudinal (in-plane, parallel to cantilever) bias-induced surface displacements. At low ac frequencies, the vertical PFM signal arises due to vertical and longitudinal surface displacements. Additional, owing to the nature of the cantilever-based force sensor of AFM, the vertical and lateral contact mechanics are coupled such that the lateral motion of the tip also affects the vertical signal. Similarly, the lateral PFM signal is also influenced by the vertical and longitudinal surface displacements.

The PFM signals are also dependent on frequency. It is found that PFM signal, which is determined by the deflection angle of the cantilever, is the addition of vertical and longitudinal components of surface displacements, the local electrostatic force acting on the tip, and the non-local distributed electrostatic force acting along the cantilever.[15] The frequency dependency of these four contributions are k_1/ω, $k_1/\omega^{1/2}$, $1/\omega$, and $1/\omega^{3/2}$, respectively, where k_1 is the spring constant of the cantilever, and ω is the bias frequency. At lower frequencies, the non-local electrostatic contribution is weaker but the longitudinal contribution becomes more influential. At higher frequencies, it is reversed. The ratio of contribution from vertical surface displacement against that of electrostatic force at the tip is independent of the frequency.

In the above non-ideal cases, it is not clear if the interpretation of PFM signals will still hold with only a small deviation or the piezoresponses will be

dominated by the secondary effects. In a previous report, the successful determination of ferroelectric polarizations by Zavaliche *et al*.[13] was done on a (001) single crystal $BiFeO_3$ film using qualitative PFM signals and crystallographic orientation information. To my knowledge, these less ideal cases have not been investigated on bulk samples before. They will be investigated in this work.

4.3.3 Determination of grain orientations with EBSD mapping

Electron backscatter diffraction (EBSD) mapping is a scanning electron microscopy (SEM) technique that maps the crystallographic orientations of the grains in a crystalline surface. Accelerated electrons incident on a crystalline sample penetrate through the surface to be scattered within the material. Some of the scattered electrons eventually exit from the surface, and some of those are captured by the EBSD camera. Of the captured electrons, those that are diffracted by the periodic crystalline lattice are used to determine the local crystallographic orientation. In general, the depth of electron interaction volume below the surface is usually greater than 10 nm.[16-19] In this work, the orientations of TiO_2 grains in the film and the orientations of $BiFeO_3$ grains in the substrate were mapped out in the study of the orientation relationships of TiO_2 and $BiFeO_3$, similar to what has been done in previous work.[4,8]

In a typical scan, the orientation (and phase in case of TiO_2) of each grain in a 1.2×1.2 mm^2 surface area was determined in a Quanta 200 SEM (FEI, Hillsboro, OR). The sample surface was tilted at ~70° with respect to the incident beam in high vacuum (10^{-5} Torr). The beam energy was set at 25 keV; the spot size was 5.5; and

the working distance was 15 mm. The EBSD Kikuchi patterns were automatically indexed by the TSL orientation imaging microscopy data collection and analysis software (Mahwah, NJ). An example of a Kikuchi pattern obtained in this work from a $BiFeO_3$ grain is given in Fig. 4.9, where both unindexed (a) and indexed (b) patterns are given.

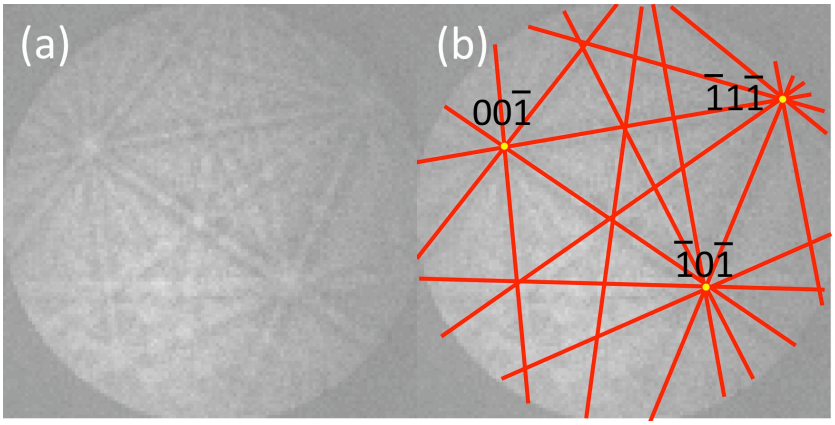

Figure 4.9 EBSD Kikuchi pattern obtained from a $BiFeO_3$ grain (a) before and (b) after indexing with the TSL software. In (b), the red lines are manually added for a clear view. The intersection points are labeled according to the software.

Because the rhombohedral structure of $BiFeO_3$ (a = 3.962 Å, α = 89°31')[20] differs from an ideal cubic structure (a = 3.962 Å) by only a slight distortion, the mapping of $BiFeO_3$ was conducted by treating the unit cell as cubic. When mapping the TiO_2 film, both anatase and rutile were recognized and their orientations were indexed in the tetragonal system. In processing the orientation data, points with a low confidence index (<0.1) were eliminated and replaced by a black dot on the map. Any adjacent points misoriented from each other by less than 5° were assumed to be part of the same grain. For example, Fig. 4.10 is a processed map showing an area on the surface of a $BiFeO_3$ substrate. Except for the black areas, each area with a constant color represents a grain of orientation indicated by the color, shown in

the standard stereographic triangle, given as the inset in Fig. 4.10. Since the orientation of each grain is known (in the form of Euler angles) for all directions in space, one can study the orientation relationships of films (TiO_2) and substrates ($BiFeO_3$), or to quantify the anisotropy in photocatalytic activity.

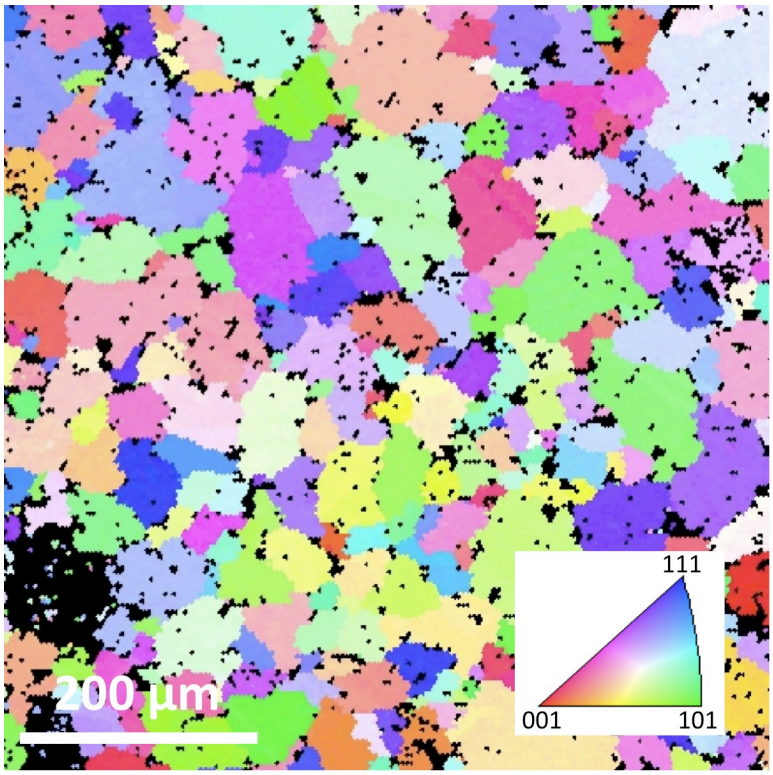

Figure 4.10 Orientation map of a $BiFeO_3$ substrate. Grains are colored according to the inset stereographic projection triangle. Black areas are for eliminated points because of low confidence indices.

References:

[1]G. S. Rohrer, Y. L. Zhang, A. M. Schultz, and P. A. Salvador, "Spatially Selective Visible Light Photocatalytic Activity of TiO_2/$BiFeO_3$ Heterostructures," *J Mater Chem,* **21**[12] 4168-74 (2011).

[2]A. M. Schultz, Y. L. Zhang, P. A. Salvador, and G. S. Rohrer, "Effect of Crystal and Domain Orientation on the Visible-Light Photochemical Reduction of Ag on $BiFeO_3$," *Acs Appl Mater Inter,* **3**[5] 1562-67 (2011).

[3]A. Maitre, M. Francois, and J. C. Gachon, "Experimental Study of the Bi_2O_3-Fe_2O_3 Pseudo-Binary System," *J Phase Equilib Diff,* **25**[1] 59-67 (2004).

[4]N. V. Burbure, "Influence of Ferroelectric Substrates on the Photochemical Reactivity of Titanium Dioxide Thin Films," *PhD Thesis* (2009).
[5]N. V. Burbure, P. A. Salvador, and G. S. Rohrer, "Influence of Dipolar Fields on the Photochemical Reactivity of Thin Titania Films on $BaTiO_3$ Substrates," *J Am Ceram Soc,* **89**[9] 2943-45 (2006).
[6]N. V. Burbure, P. A. Salvador, and G. S. Rohrer, "Photochemical Reactivity of Titania Films on $BaTiO_3$ Substrates: Origin of Spatial Selectivity," *Chem Mater,* **22**[21] 5823-30 (2010).
[7]N. V. Burbure, P. A. Salvador, and G. S. Rohrer, "Photochemical Reactivity of Titania Films on $BaTiO_3$ Substrates: Influence of Titania Phase and Orientation," *Chem Mater,* **22**[21] 5831-37 (2010).
[8]N. V. Burbure, P. A. Salvador, and G. S. Rohrer, "Orientation and Phase Relationships between Titania Films and Polycrystalline $BaTiO_3$ Substrates as Determined by Electron Backscatter Diffraction Mapping," *J Am Ceram Soc,* **93**[9] 2530-33 (2010).
[9]J. B. Lowekamp, G. S. Rohrer, P. A. M. Hotsenpiller, J. D. Bolt, and W. E. Farneth, "Anisotropic Photochemical Reactivity of Bulk TiO_2 Crystals," *J Phys Chem B,* **102**[38] 7323-27 (1998).
[10]L. G. Parratt, "Surface Studies of Solids by Total Reflection of X-Rays," *Phys Rev,* **95**[2] 359-69 (1954).
[11]M. F. Toney and S. Brennan, "Measurements of Carbon Thin-Films Using X-Ray Reflectivity," *J Appl Phys,* **66**[4] 1861-63 (1989).
[12]S. V. Kalinin and D. A. Bonnell, "Imaging Mechanism of Piezoresponse Force Microscopy of Ferroelectric Surfaces," *Phys Rev B,* **65**[12] (2002).
[13]F. Zavaliche, S. Y. Yang, T. Zhao, Y. H. Chu, M. P. Cruz, C. B. Eom, and R. Ramesh, "Multiferroic $BiFeO_3$ films: Domain Structure and Polarization Dynamics," *Phase Transit,* **79**[12] 991-1017 (2006).
[14]P. W. Hawkes and J. C. H. Spence, "Science of Microscopy," **Vol. 2**. Springer: New York, (2007).
[15]S. V. Kalinin, A. Rar, and S. Jesse, "A Decade of Piezoresponse Force Microscopy: Progress, Challenges, and Opportunities," *IEEE T Ultrason Ferr,* **53**[12] 2226-52 (2006).
[16]D. Chen, J. Kuo, and W. Wu, "Effect of Microscopic Parameters on EBSD Spatial Resolution," *Ultramicroscopy,* **111** 1488-94 (2011).
[17]T. C. Isabell and V. P. Dravid, "Resolution and Sensitivity of Electron Backscattered Diffraction in a Cold Field Emission Gun SEM," *Ultramicroscopy,* **67**[1-4] 59-68 (1997).
[18]K. Z. Troost, "Submicron Crystallography in the Scanning Electron Microscope," *Philips J Res,* **47**[3-5] 151-62 (1993).
[19]J. A. Venables and C. J. Harland, "Electron Backscattering Patterns - New Technique for Obtaining Crystallographic Information in Scanning Electron Microscope," *Philos Mag,* **27**[5] 1193-200 (1973).
[20]W. B. Pearson, J. Trotter, B. Beagly, E. Banks, and C. E. Nordman, "Structure Reports," **Vol. 28**. Oosthoek, Scheltema & Holkema: Utrecht, (1963).

Chapter 5 Visible-light photocatalytic activity of $TiO_2/BiFeO_3$

5.1 Introduction

In this chapter, the photocatalytic activity of $TiO_2/BiFeO_3$ heterostructures was observed under visible blue light irradiation. Reduced Ag particles from the photochemical reaction were detected and their patterns on the sample surfaces were imaged using atomic force microscopy (AFM). At the same time, it was found that the pattern of reduced Ag mimics the ferroeletric domain structure of the underlying $BiFeO_3$, identified using vertical piezoresponse force microscopy (VPFM). The discovery supports the hypothesis that photo-generated electrons migrate from the $BiFeO_3$ substrate through the TiO_2 film to reach the TiO_2 surface, where they participate in the reduction reaction of Ag^+. It also supports the hypothesis that the ferroelectricity influences the photocatalytic behavior of the heterostructure, specifically the reactivity at the surface of the non-ferroelectric TiO_2 film. The contents of this chapter are derived from the already published paper.[1]

5.2 Results

The heterostructures considered here consist of either rutile/$BiFeO_3$ or anatase/$BiFeO_3$, described later in Chapters 7 and 8. Therefore, we begin by evaluating the photochemical activity of each of the three phases by themselves. Please note that the photochemical reduction of silver from an aqueous $AgNO_3$ solution was conducted on every sample in this chapter for 60 s with the blue LED

operated at 750 mA and 4 V. The AFM images in Fig. 5.1 show the surface of $BiFeO_3$ (a,b), rutile (c,d), and anatase (e,f). The $BiFeO_3$ and rutile are bulk ceramic materials. The anatase sample, on the other hand, is a 20 nm film deposited on $SrTiO_3$ (100) under conditions that produce anatase (001).[2,3] The topographic contrast in the AFM images arises from a variety of sources including surface steps (S), residual polishing scratches (PS), boundaries between ferroelectric domains (DB), surface contamination (SC), and inclusions of minority phases (MP), which are labeled on the micrographs.

After the photochemical reaction, the surfaces of certain regions in $BiFeO_3$ are coated with reduced silver (white contrast). The heights of these features vary between 20 and 130 nm. This is the same reaction that has been observed previously on TiO_2,[4,5] $BaTiO_3$,[6,7] and PZT[8,9] when illuminated by UV light. Here, the reaction is initiated by visible light. On the TiO_2 surfaces, only small changes in contrast are found, corresponding either to a small amount of silver or surface contamination from immersion in the silver nitrate solution. Based on these images, it can be concluded that the $BiFeO_3$ surface reduced far more silver on the active domains than either of the TiO_2 surfaces.

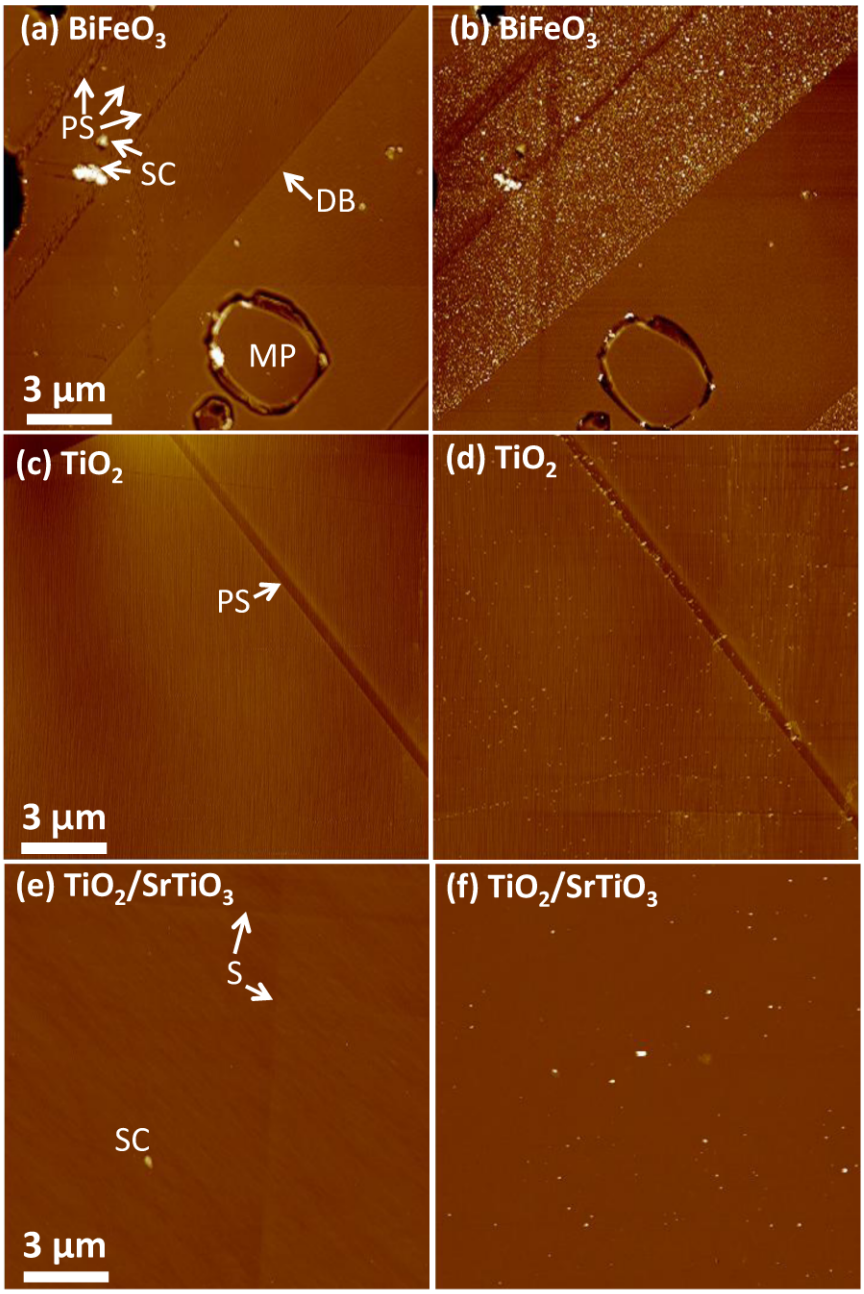

Figure 5.1 AFM topographic images of surfaces of (a) bare $BiFeO_3$ before reaction, (b) $BiFeO_3$ after reaction, (c) bare rutile TiO_2 before reaction, (d) rutile TiO_2 after reaction, (e) 20 nm anatase TiO_2 film on $SrTiO_3$ (100) before reaction, (f) 20 nm anatase TiO_2 film on $SrTiO_3$ (100) after reaction. The topographic contrast in all images is 100 nm from bright to dark.

The images in Fig. 5.2 show the correlation between the piezoresponse of the substrate (a) and heterostructure (b) and the photochemical reactivity of the TiO_2

film surface (c, d). The contrast in the VPFM phase image of the $BiFeO_3$ surface reveals the domain structure of the substrate. After depositing a 10 nm TiO_2 film, the piezoresponse of the heterostructure is the same. Therefore, the displacements in the substrate that create the VPFM signal are not significantly affected by the 10 nm TiO_2 film. (This is further elaborated on in Chapter 6, where it appears that the TiO_2, on average, does influence the VPFM images. But it has to be noted that the VPFM phase images (a, b) were taken at a frequency different from the frequency used in Chapter 6, and thus are not compared to the images in that chapter.) The image in Fig. 5.2 (c) shows the topography of the film surface. Note that some of the components of the film topography correlate exactly with the domain structure revealed by the VPFM images. After the sample is illuminated by blue light in the silver nitrate solution, new contrast appears on the surface, corresponding to reduced silver (see Fig. 5.2 (d)). Similar to the reaction on the bare substrate (Fig. 5.1 (b)), there is more silver reduced on some domains than others. A typical height differential for the silver, between regions of different activity, is 100 nm. In this case, the domains that are dark in the VPFM images reduce more silver than the domains of light contrast in VPFM.

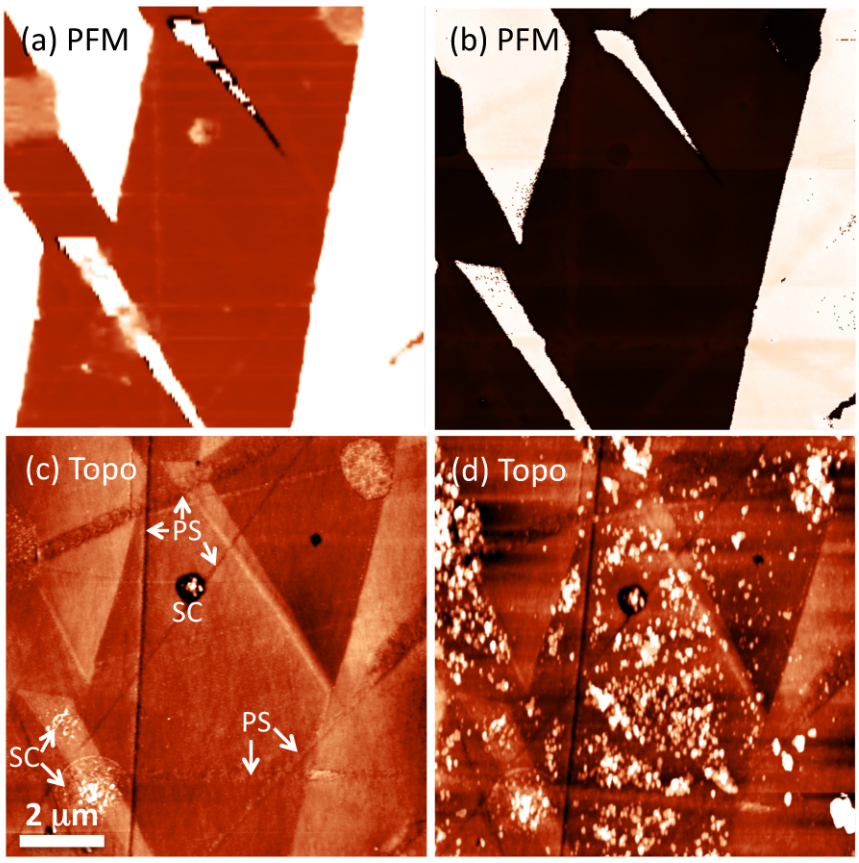

Figure 5.2 (a) VPFM phase image of bare $BiFeO_3$ surface. (b) VPFM phase image of 10 nm $TiO_2/BiFeO_3$. (c) Topographic image of 10 nm $TiO_2/BiFeO_3$ before reaction. (d) Topographic image of 10 nm $TiO_2/BiFeO_3$ after reaction. VPFM phase contrast scale is -180° to 180° from bright to dark. Topographic contrast scale is 15 nm from bright to dark.

Because the substrate and the thin TiO_2 film are both able to reduce Ag with visible light, but TiO_2 by itself can not, it is reasonable to posit that, as the film increases in thickness, the film will become less reactive as the influence of the substrate decreases. To test this idea, the experiment was repeated using TiO_2 films that were 20 nm and 80 nm thick and the results are compared in Fig. 5.3. For each case, an AFM topographic image of a surface region before reaction, a topographic image of the same region after reaction, and a height profile are given in each row in the figure. The change in contrast after reaction corresponds to reduced silver

particles. One line in blue is drawn on the image recorded before the reaction and a second in red is drawn on the same location after the reaction. The topography along these two lines is compared in the third column (a3, b3, c3) of the figure. For the 10 nm and 20 nm thick films, the maximum heights of the deposited silver are in the range of 60 to 100 nm. But for the 80 nm thick TiO_2 film, the heights of the deposited silver do not exceed 20 nm. Although much weaker than those of the 10 nm and 20 nm films, the reactivity of the 80 nm film is still stronger than those of the rutile and anatase TiO_2, shown in Fig. 5.1(d) and 5.1(f), respectively. For comparison, the maximum height of silver deposited on the bare $BiFeO_3$ surface under the same conditions is approximately 130 nm. Therefore, the amount of silver reduced by the TiO_2 film decreases with film thickness.

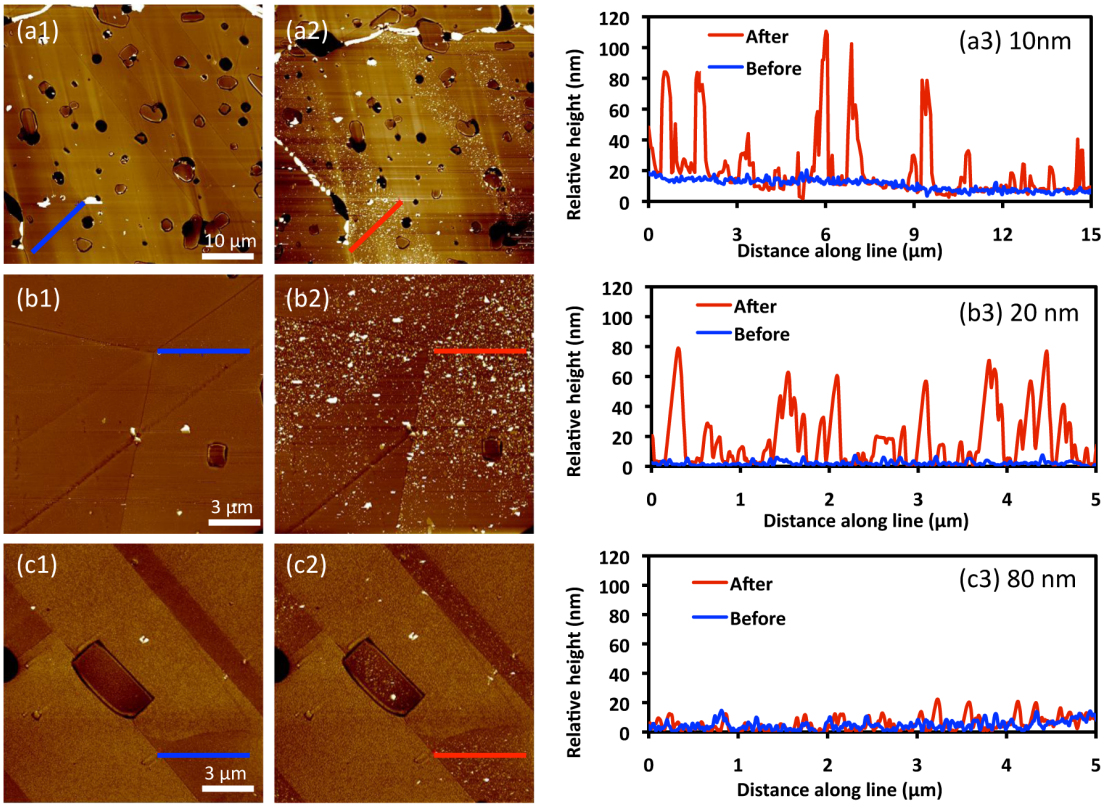

Figure 5.3 AFM Topographic images and height profiles of $TiO_2/BiFeO_3$ with TiO_2 thickness of (a) 10, (b) 20, and (c) 80 nm. Each row from left to right shows the image before reaction, the image after reaction, and a comparison of the height profiles at the same locations. The contrast scale from bright to dark is 100 nm for all images.

Ideally, the only component of the heterostructures that can absorb light and create carriers is the substrate. However, based on previous work,[10] one could hypothesize that Fe contamination (which could diffuse from the $BiFeO_3$ substrate to the TiO_2 film during growth) might increase absorption in the film. While it is impossible to eliminate contamination from the substrate as a source of activity in the TiO_2 layer, it is possible to grow Fe-doped TiO_2 films on substrates that does not absorb visible light, to explore the effects of Fe-doping and qualify if it explains the visible light activity observed in the $TiO_2/BiFeO_3$ heterostructures. The AFM images in Fig. 5.4 compare the surface of a 10 nm thick Fe-doped TiO_2 film on $SrTiO_3$ (100)

before and after the reaction. It is clear from the image in Fig. 5.4 (b) that very little silver is deposited on the Fe-doped (2 at%) TiO_2 film. Therefore, Fe-doping in the TiO_2 layer is not a likely explanation for the reactivity of the unintentionally doped TiO_2 films on the $BiFeO_3$ surface.

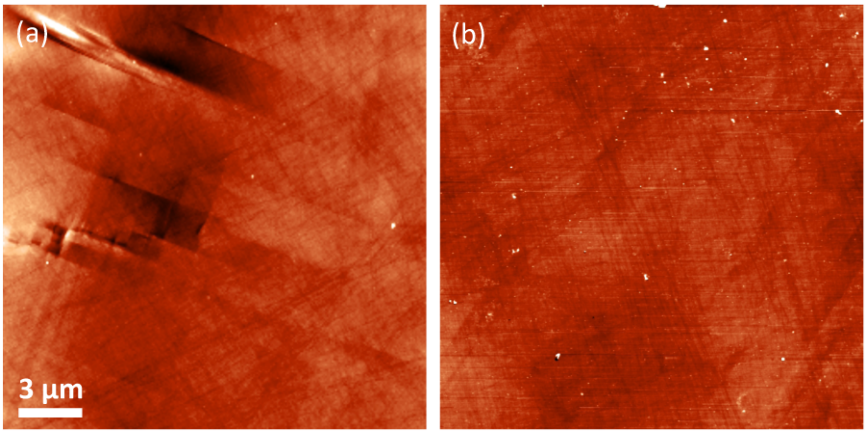

Figure 5.4 Topographic images of a 10 nm thick Fe-doped-TiO_2 film on $SrTiO_3$ (100) (a) before reaction and (b) after reaction. The contrast scale from bright to dark is 15nm. The images are not from the same area, but are representative of all areas that were imaged.

It is also feasible that the ferroelectric substrate creates charged interface states that induce the visible light activity. To test this idea, a 20 nm TiO_2 film was grown on $BaTiO_3$, which is also ferroelectric, but does not absorb visible light.[11,12] The results are shown in Fig. 5.5. The image in Fig. 5.5 (a) shows the surface of the TiO_2 film before reaction. The image shows some weak contrast that arises from the domain structure of the substrate. The image in Fig. 5.5 (b) shows some silver on the surface. However, the amount of deposited silver is much less than on films supported by $BiFeO_3$ and is similar to the silver observed on the surface of bulk TiO_2 (see Fig. 5.1). Furthermore, there is no obvious correlation between the pattern of

silver and the underlying domain structure as observed when the same structure is illuminated by UV light.[13,14]

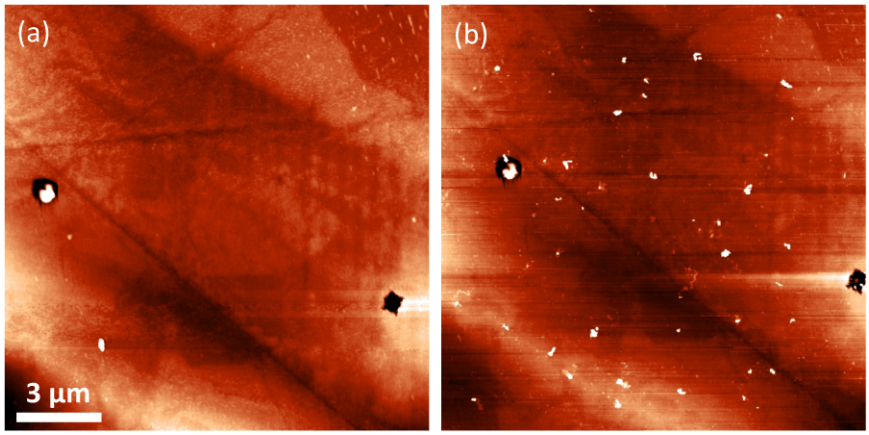

Figure 5.5 Topographic images of a 20 nm TiO_2 film on $BaTiO_3$ (a) before reaction and (b) after reaction. The contrast scale from bright to dark is 40 nm.

5.3 Discussion

The results presented here indicate that the photochemical reduction of silver, initiated by visible light, is spatially selective on the $BiFeO_3$ surface. Assuming the spatially selective reactivity is analogous to what occurs in $BaTiO_3$ and PZT, then the reduction reaction is probably associated with domains that have polarizations pointed at the surface, where bands are bent downward and electrons move down the gradient toward the surface.[6,7,9,13] The main difference is that, for $BaTiO_3$ and PZT, the same reaction can only be initiated by UV light, while it is initiated with blue light for $BiFeO_3$.

TiO_2 is relatively unreactive when illuminated by visible light. The images of bulk rutile (Fig. 5.1 (d)), anatase supported by $SrTiO_3$ (Fig. 5.1 (f)), and TiO_2 supported by $BaTiO_3$ (Fig. 5.5 (b)) after illumination suggest that a small amount of

silver is reduced, even though the band gaps are larger than the energy of illumination. The distribution of reaction product is inhomogeneous; we assume that the carriers responsible for this limited reaction are generated by absorption of light at defect states (such as oxygen vacancies, which have states below the conduction band edge). This background reactivity is presumably present in all of the experiments, but is overwhelmed by the spatially selective reactivity of the films supported by $BiFeO_3$.

The observations from the $TiO_2/BiFeO_3$ heterostructures indicate that the carriers that react on the TiO_2 film surface are created by absorption in the substrate. This is completely analogous to the conclusion reached by Burbure *et al*.[13,14] in studies of thin TiO_2 films on $BaTiO_3$ excited by UV radiation. One observation that supports this conclusion is that when TiO_2 is not supported by $BiFeO_3$, it absorbs very little light of this energy and does not reduce significant amounts of silver. The second observation is that the patterns of silver on the surface have the same configuration as the patterns of ferroelectric domains in the supporting substrate. The third supporting observation is that the reactivity of the film decreases as the thickness increases. This all indicates that light absorbed in the narrower band gap substrate creates electrons that travel through the thin film and react on the surface.

It should be mentioned that a recent study of anatase-$BiFeO_3$ nanocomposites demonstrated enhanced visible light activity compared to TiO_2 alone.[10] In that case, the enhancement was attributed to interdiffusion of the metallic components and, in particular, Fe-doping of the TiO_2. However, the results

shown in Fig. 5.4 indicate that Fe-doping in the film is, by itself, not sufficient to make the films significantly more reactive in the conditions used here. Another possible explanation is that multiple reflections and scattering at the buried interface between the ferroelectric and the supported film enhance the path length of light in the TiO_2 film and lead to enhanced absorption. However, if this were the case, then we would have expected the same result in the film supported by $BaTiO_3$ and by $SrTiO_3$; the film supported by $BaTiO_3$ is not significantly more reactive in visible light than bulk TiO_2.

Of the situations examined here, the $BiFeO_3$ substrate had the highest reactivity and the TiO_2 films all have lower reactivities. If the goal were only to have the highest reactivity for silver reduction, $BiFeO_3$ would be the best choice. However, to be useful for water photolysis, the material must be stable in aqueous solutions and its conduction band energy must be higher than the hydrogen reduction level. While these two conditions are met by TiO_2, they are not met by $BiFeO_3$,[10,15,16] as mentioned in section 2.3.1.

To understand the mechanism of visible light reactivity, plausible energy level diagrams for the heterostructures (see Fig. 2.11) are constructed as described in Chapter 2. Assuming that the energy levels at the interface are strongly influenced by the polarization, then the bands in $BiFeO_3$ bend upward when the polarization is directed away from the surface (referred to as negative domains) and downward when directed toward the surface (positive domains), as shown in Figs. 2.11 (a) and 2.11 (b), respectively. Therefore, photo-generated electrons in negative domains encounter a barrier that prevents them from reaching the surface. In positive

domains, electrons are driven to the interface. The experimental observation of spatially selective patterns of reduced silver supports this mechanism. There is, however, no direct evidence in the results. The next chapter will address this issue. Assuming this mechanism is correct, then the same mechanism should apply to other heterostructures where TiO_2 is supported by a narrow band gap, p-type substrate.

5.4 Conclusion

Thin TiO_2 films supported on $BiFeO_3$ substrates reduce silver cations from aqueous solutions when excited by visible light with energy less than TiO_2's band gap. The patterns of reduced silver on the TiO_2 surface mimic the structure of the domains found in the $BiFeO_3$ substrate. The observations indicate that electrons generated in the $BiFeO_3$ substrate can be transported to the surface of the film where they reduce silver. Electron transport to the surface is speculated to be favored in domains with a positive polarization pointed toward the surfaces.

Reference:

[1]Y. Zhang, G. S. Rohrer, A. M. Schultz, and P. A. Salvador, "Spatially Selective Visible Light Photocatalytic Activity of TiO_2/$BiFeO_3$ Heterostructures," *J. Mater. Chem.,* **21**[12] 4168-74 (2011).

[2]C. C. Hsieh, K. H. Wu, J. Y. Juang, T. M. Uen, J. Y. Lin, and Y. S. Gou, "Monophasic TiO_2 Films Deposited on $SrTiO_3$(100) by Pulsed Laser Ablation," *J. Appl. Phys.,* **92**[5] 2518-23 (2002).

[3]S. Yamamoto, T. Sumita, T. Yamaki, A. Miyashita, and H. Naramoto, "Characterization of Epitaxial TiO_2 Films Prepared by Pulsed Laser Deposition," *J. Cryst. Growth,* **237** 569-73 (2002).

[4]P. A. M. Hotsenpiller, J. D. Bolt, W. E. Farneth, J. B. Lowekamp, and G. S. Rohrer, "Orientation Dependence of Photochemical Reactions on TiO_2 Surfaces," *J. Phys. Chem. B,* **102**[17] 3216-26 (1998).

[5]J. B. Lowekamp, G. S. Rohrer, P. A. M. Hotsenpiller, J. D. Bolt, and W. E. Farneth, "Anisotropic Photochemical Reactivity of Bulk TiO_2 Crystals," *J. Phys. Chem. B,* **102**[38] 7323-27 (1998).

[6]J. L. Giocondi and G. S. Rohrer, "Spatial Separation of Photochemical Oxidation and Reduction Reactions on the Surface of Ferroelectric $BaTiO_3$," *J. Phys. Chem. B,* **105**[35] 8275-77 (2001).

[7]J. L. Giocondi and G. S. Rohrer, "Spatially Selective Photochemical Reduction of Silver on the Surface of Ferroelectric Barium Titanate," *Chem. Mater.,* **13**[2] 241-42 (2001).

[8]S. Dunn, P. M. Jones, and D. E. Gallardo, "Photochemical Growth of Silver Nanoparticles on c^- and c^+ Domains on Lead Zirconate Titanate Thin Films," *J. Am. Chem. Soc.,* **129**[28] 8724-28 (2007).

[9]D. Tiwari and S. Dunn, "Photochemistry on a Polarisable Semiconductor: What Do We Understand Today?," *J. Mater. Sci.,* **44**[19] 5063-79 (2009).

[10]S. Li, Y. H. Lin, B. P. Zhang, J. F. Li, and C. W. Nan, "$BiFeO_3/TiO_2$ Core-Shell Structured Nanocomposites as Visible-Active Photocatalysts and Their Optical Response Mechanism," *J. Appl. Phys.,* **105**[5] (2009).

[11]L. Hafid, G. Godefroy, A. Elidrissi, and F. Michelcalendini, "Absorption-Spectrum in the Near UV and Electronic Structure of Pure Barium-Titanate," *Solid State Commun.,* **66**[8] 841-45 (1988).

[12]S. H. Wemple, "Polarization Fluctuations and Optical Absorption Edge in $BaTiO_3$," *Phys. Rev. B,* **2**[7] 2679-89 (1970).

[13]A. Bhardwaj, N. V. Burbure, A. Gamalski, and G. S. Rohrer, "Composition Dependence of the Photochemical Reduction of Ag by $Ba_{1-x}Sr_xTiO_3$," *Chem. Mater.,* **22**[11] 3527-34 (2010).

[14]N. V. Burbure, P. A. Salvador, and G. S. Rohrer, "Photochemical Reactivity of Titania Films on $BaTiO_3$ Substrates: Origin of Spatial Selectivity Substrates," *Chem. Mater.,* **22**[21] 5823-30 (2010).

[15]R. Q. Guo, L. Fang, W. Dong, F. G. Zheng, and M. R. Shen, "Magnetically Separable $BiFeO_3$ Nanoparticles with a Gamma-Fe_2O_3 Parasitic Phase: Controlled Fabrication and Enhanced Visible-Light Photocatalytic Activity," *J. Mater. Chem.,* **21**[46] 18645-52 (2011).

[16]Z. J. Shen, W. P. Chen, G. L. Yuan, J. M. Liu, Y. Wang, and H. L. W. Chan, "Hydrogen-Induced Degradation in Multiferroic $BiFeO_3$ Ceramics," *Mater. Lett.,* **61**[22] 4354-57 (2007).

Chapter 6 Correlation between Polarization and Photochemical Activity of $BiFeO_3$ and $TiO_2/BiFeO_3$

6.1 Introduction

According to the energy level diagram in Fig. 2.11, electrons photogenerated in positive domains near the $TiO_2/BiFeO_3$ interfacial layers in the $BiFeO_3$ substrate can migrate to the surface of the TiO_2 film to participate in the photochemical reduction of Ag^+ cations in the $AgNO_3$ solution. A similar statement of photochemical reactivity can be claimed for a bare $BiFeO_3$ substrate without the TiO_2 film. However, there is no direct evidence to support the hypothesis that the domains with reduced Ag particles after reaction are positive ones (with respect to the surface). The goal of this chapter is to provide support to the existence of a correlation between polarization and photochemical activity.

Piezoresponse Force Microscopy (PFM) can be used to determine the polarizations of ferroelectric domains. Zavaliche's group has demonstrated that the domain polarizations of an epitaxial (001)-oriented $BiFeO_3$ film can be determined from vertical PFM (VPFM) and lateral PFM (LPFM) images together with the inherited knowledge of its crystallographic orientation.[1] In fact, nearly all of the papers in the literature discuss polarization determination of ferroelectric thin films using PFM, and no work has been reported on bulk samples. As of interest to this work, only the VPFM images were taken on the bulk bare $BiFeO_3$ and $TiO_2/BiFeO_3$ samples to determine the out-of-plane polarization. At the outset, it was unclear as to whether the VPFM signals of the bulk samples would correlate directly to the

polarization direction or if they would be dominated by the secondary effects mentioned in section 4.3.2. The answer to this will be investigated in this chapter.

Combining the knowledge of crystallographic orientation with VPFM responses could, in principle, help determine domain polarizations even if VPFM does not unambiguously resolve the issue. The crystallographic orientation of $BiFeO_3$ grains can be detected using EBSD techniques. The details of methodology developed in this work are described in the following experimental section. This chapter describes attempts to identify domain polarizations of the bare $BiFeO_3$ substrate and the $TiO_2/BiFeO_3$ heterostructure, using VPFM phase and magnitude signals and crystallographic orientation. Though absolute identifiers are still lacking, correlations could be made that allow for a reasonable speculation to the orientation for the preferred reactive domains.

6.2 Experimental

EBSD was used to map the orientation of the grains on the surface of the bare $BiFeO_3$ substrate, as well as of a $BiFeO_3$ substrate before a 10 nm TiO_2 film was deposited. VPFM images were taken on a number of grains for both the bare substrate and the heterostructure. After a 20-min Ag reduction reaction, AFM topographic images were taken on the same grains.

Two approaches to determine domain polarizations are discussed in this chapter. The VPFM approach uses only the VPFM information. The Boundary Pattern approach uses VPFM information combined with crystallographic orientation information.

The VPFM approach uses both VPFM phase and magnitude responses. Ideally, the VPFM phase response for negative domains is zero and for positive domains is 180°. The VPFM magnitude response is proportional to the magnitude of out-of-plane polarization. By knowing both VPFM phase and magnitude one can tell the out-of-plane polarity and strength of the domain polarization. In reality, as discussed in section 4.3.2, the vertical electromechanical responses are complicated by local and non-local electrostatic influences and longitudinal signals. Because there is no established method of isolating the desired vertical electromechanical responses, the measured VPFM signals in this work are viewed statistically to determine the domain polarizations.

The Boundary Pattern approach uses crystallographic orientation and VPFM images to determine polarization. The strategy is to determine the types of domain boundaries in VPFM images first, then to determine polarization in each domain. The orientation of all possible domain boundary planes in a $BiFeO_3$ grain can be predicted if the orientation of that grain is known. When those domain boundary planes intersect with the surface plane, the lines of intersection can be calculated. The calculated domain boundary vectors should consistently match the boundary traces observed in the VPFM image.

EBSD provides the crystallographic orientation of a grain with respect to its surface in the form of (hkl) [uvw], where (hkl) is the Miller index of the surface plane and [uvw] is the Miller index of the vector in the surface plane that points vertically downward, forming a 90° angle with the scanning direction clockwise. As mentioned in section 2.2.1, 71° and 109° domain boundaries are on {100} and {110}

planes and 180° boundaries can be on any planes in the [111] zone. The vectors of these domain boundary planes intersecting the surface plane can be calculated by crossing the normal vector of the surface plane [hkl] with the normal vector of each domain habit plane. The angle between each calculated vector and [uvw] is then calculated. As for the VPFM images, the angles between traces of domain boundaries and the vertically downward vector can be measured using ImageJ (http://imagej.nih.gov/ij). Based on a comparison of the measured angles and the calculated angles, one can determine the type of domain boundary for each boundary trace in the VPFM images. Because the pattern of domain boundaries in an image imposes restrictions on choices of polarizations across each boundary, a finite list of domain configurations can be proposed. An example of this approach will be given in section 6.3.2 to explain this complex procedure.

Finally, the polarizations determined from both approaches can be compared to AFM images recorded after the reduction of Ag to check if there is a correlation between out-of-plane polarization and photochemical activity.

6.3 Results and Discussion

6.3.1 VPFM Approach

A total of 95 domains from 30 grains in bare $BiFeO_3$ and 161 domains from 42 grains in $TiO_2/BiFeO_3$ were examined. Fig. 6.1 shows the VPFM phase, VPFM magnitude and AFM topographic images of a grain in bare $BiFeO_3$ (a, b, c, respectively) and a grain in $TiO_2/BiFeO_3$ (d, e, f, respectively), as two examples. The first grain (the one in the bare $BiFeO_3$) is oriented along $(2\ \bar{2}\ 15)$, which is ≈ 11 °

away from the low index (001) plane. The second grain (the one in the heterostructure) is oriented along $(\bar{1}\bar{1}\ 15\ 29)$, which is ≈ 6 ° away from $(\bar{1}12)$. In the VPFM phase images (a, d), the values listed are the average phase value for each domain. Similarly, in the VPFM magnitude images (b, e), the values listed are the average magnitudes. The types of boundary planes were determined, as described in section 6.3.2, and their Miller indices are listed on each boundary in (a, d). In the AFM topographic images (c, f), the average height of the reduced Ag particles, with respect to the surface before reaction, are listed on reactive domains (for non-reactive grains no number is given). The domains were categorized as "reactive" if the height of Ag particles was > 20 nm, and as "unreactive" if the height was < 20 nm.

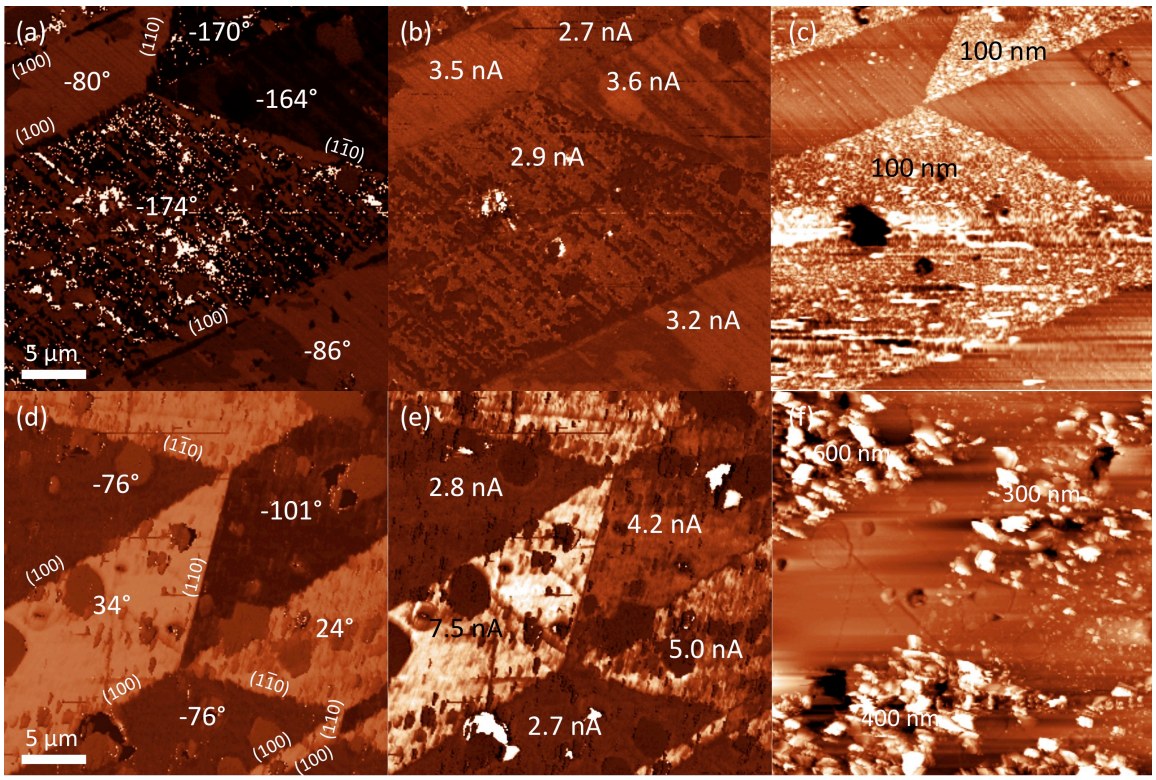

Figure 6.1 VPFM phase image, VPFM magnitude image, and AFM topographic image after silver reduction reaction of the same area for the bare $BiFeO_3$ sample (a, b, c, respectively) and for the $TiO_2/BiFeO_3$ sample (d, e, f, respectively). The values are approximately the average signal readings in the labeled domains. The contrast bar from bright to dark is 360° for (a, d), 8 nA for (b), 5 nA for (e), 200 nm for (c), and 500 nm for (f), respectively.

6.3.1.1 VPFM Phase Angle

Obviously, the VPFM phase responses in (a, d) are neither 0° nor 180°. Consequently, the out-of-plane domain polarization cannot be unambiguously assigned using only the VPFM phase response. Nevertheless, it was found that reactive domains in any given VPFM phase image tended to show similar phase responses. In the example of the bare $BiFeO_3$ substrate shown in Fig. 6.1(a,b,c), the domains of -170° and -174° are reactive and those of -80° and -86° are unreactive.

The domain of -164°, however, is unreactive. As for the $TiO_2/BiFeO_3$, the domains of -76° and -101° are reactive, as opposed to the unreactive ones of 24° and 34°. This was true for most of the 72 grains investigated, indicating that specific types of domains were indeed reactive over others.

This observation led to a hypothesis that the VPFM phase responses of most reactive domains and most unreactive domains are separated, statistically speaking. To test this hypothesis, reactivity was plotted as a function of phase angle, and these plots are given in Fig. 6.2 for the bare substrate (a) and the heterostructure (b). The phases of reactive and unreactive domains in the bare $BiFeO_3$ substrate are distributed over ranges of 177 ° to 180 ° and -180° to -52°. Note that the two ranges are connected at 180°/-180°. The phases of reactive and unreactive domains in the $TiO_2/BiFeO_3$ heterostructure are all spread out over the whole 360° range. (The difference in the two ranges for the phase values is not surprising since the the 10 nm TiO_2 film could significantly influence the tip-surface interaction, as well as the electrostatic contribution to the VPFM signals.) The observation that reactive and unreactive domains are not separated in phase-angle space indicates that the absolute VPFM phase response, from grain to grain, is not strongly correlated to the reactivity of a domain, in both specimens.

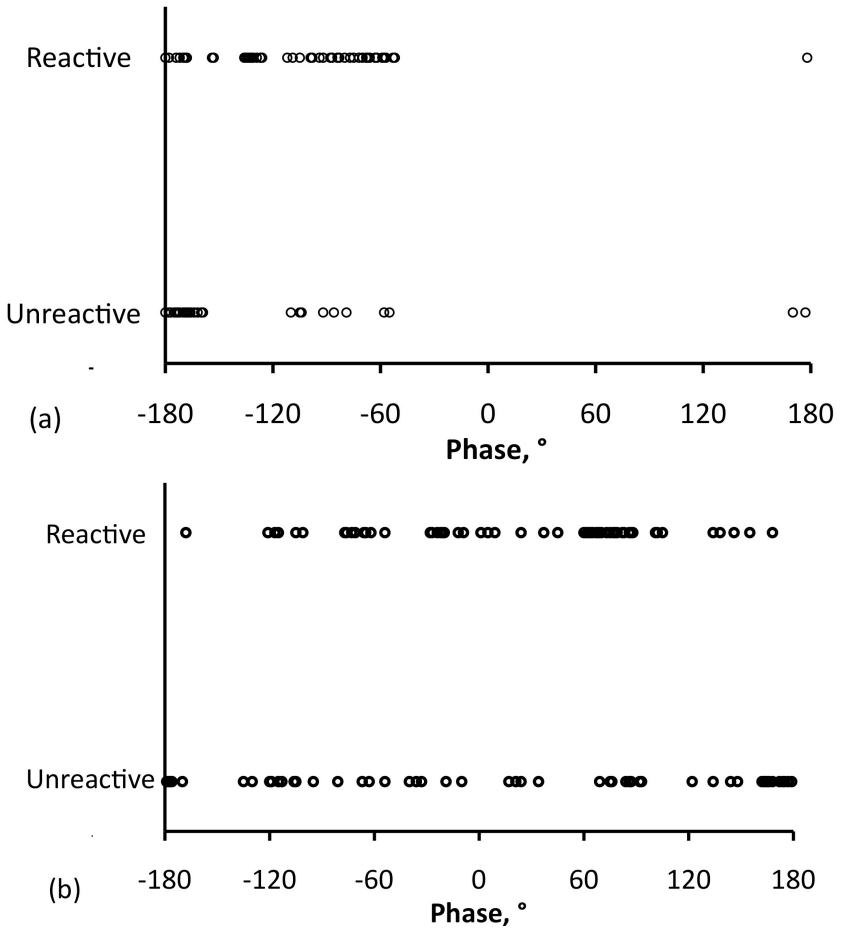

Figure 6.2 Plots of reactivity against VPFM phase for (a) the bare $BiFeO_3$ substrate and (b) the $TiO_2/BiFeO_3$ heterostructure.

A second method was used to assess the overall set of observations from a collective perspective. The relative phase difference between reactive and unreactive domains in each VPFM phase image was calculated by subtracting the average phase reading of all unreactive domains from the average phase reading of all reactive domains. The phase difference was confined in the range -180° to 180° so that if a calculated value was greater than 180° or less than -180°, 360° was subtracted from or added to it. The entire -180° to 180° range was further subdivided into twelve 30° slots. Fig. 6.3 shows two bar charts of these collected

phase differences for both (a) the bare $BiFeO_3$ substrate and (b) the $TiO_2/BiFeO_3$ heterostructure. In Fig. 6.3, the number written above the bar indicates the observation frequency of the phase difference within that 30° range. For the 30 images of the bare $BiFeO_3$, 8 images are excluded because the domains in them were either all reactive or all unreactive (and therefore no differences could be determined). For the remaining images, 82% of them (18 out of 22) have positive phase differences, which means the average phase of reactive domains is leading that of unreactive domains. Of the 42 images of the $TiO_2/BiFeO_3$ specimen, 9 were excluded, in which 2 had single domains, 4 had all reactive or all unreactive domains, and 3 had reactive domains of which some leading and others lagging unreactive domains in phase (leading or lagging is inconsistent). For the remaining images, 85% of them (28 out of 33) have negative phase differences, which means the average phase of reactive domains is lagging that of unreactive domains.

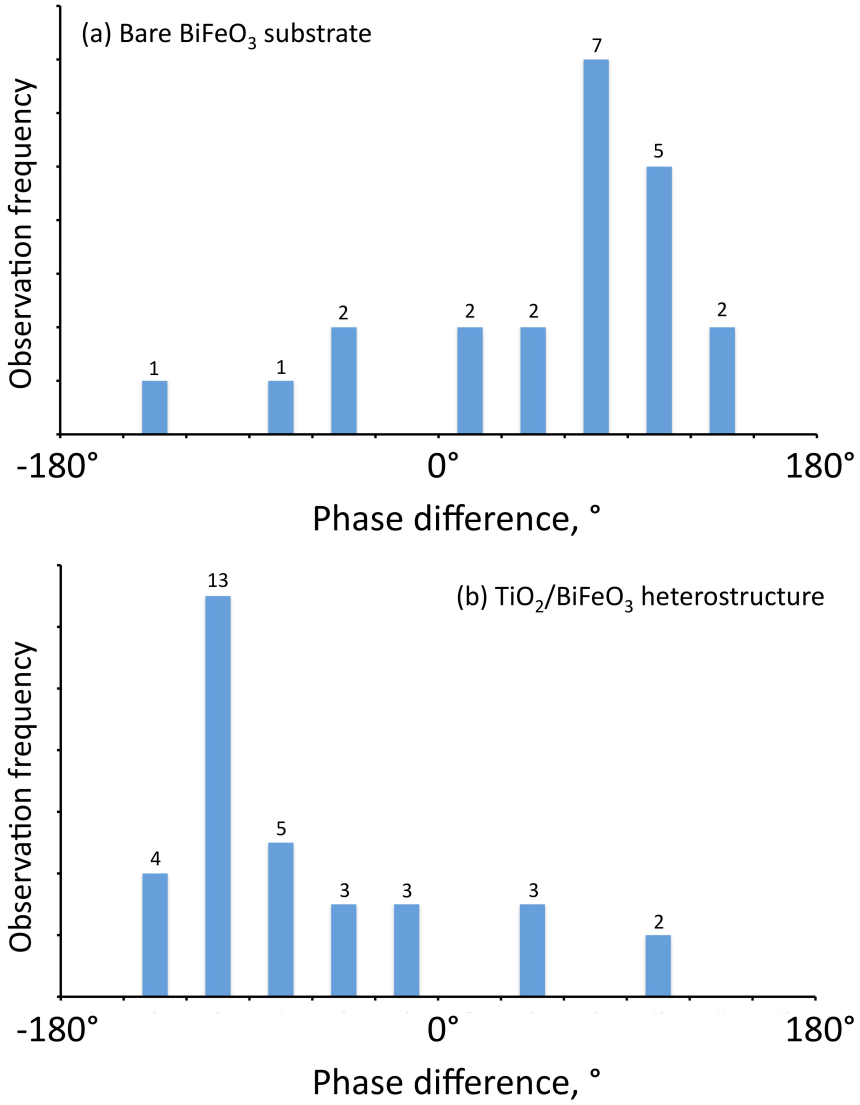

Figure 6.3 Diagrams of phase difference between reactive and unreactive domains in each VPFM phase image for (a) the bare $BiFeO_3$ substrate and (b) the $TiO_2/BiFeO_3$ heterostructure.

In the literature, zero to negative VPFM phase values are observed for positive domains and the phase difference between positive and negative domains is close to 180°.[2-5] However, it has to be mentioned that most reports performed PFM measurements on epitaxial ferroelectric films on single crystal substrates or

single crystals of uniform thickness. The uniform crystallinity and crystal orientation of those samples ensured the consistency of material properties other than local polarizations at the surface, such that the influence of the relevant material properties on the PFM responses was consistent. The uniform thickness of those samples also ensured a relatively constant electric field across the samples and, consequently, a more easily interpretable electromechanical response throughout the samples. Lacking these two merits, owing to the bulk and polycrystalline nature of the samples in this work, the VPFM phases of the bare $BiFeO_3$ and the $TiO_2/BiFeO_3$ were complicated by the influence of secondary sources, which remain to be explored. There is no quantitative analysis of these influences on PFM phase signals available in the literature.[6] This remains a challenging issue and is not the focus of the current work.

This work reports the VPFM phase responses on bulk polycrystalline $BiFeO_3$ and $BiFeO_3$ with a TiO_2 film for the first time. It is clear that interpretation of the phase angles is challenging and is affected strongly by secondary factors. This inhibits a clear interpretation of the overall results. However, several things are worth summarizing. The reactivity of the sample surface is domain dependent. The absolute values in a given image did not correlate with the values in any other image, but within any image phase values could be correlated with reactivity. By examining the overall set, it was observed that (on average) reactive domains lead unreactive domains in phase in bare $BiFeO_3$, and they tend to lag unreactive ones in the case of $TiO_2/BiFeO_3$. This implies that the TiO_2 film inverts (on average) the phase response for the underlying $BiFeO_3$ domains. While this further complicates

the interpretation of the VPFM phase signal, it indicates that one should focus on the underlying substrate to make correlations with reactivity and polarization. If one were to apply the standard interpretation, domains with phase at or near 0 ° would be negative and those at or near ±180 ° would be positive. The standard interpretation would not tell the polarity from relative phase difference, because the difference is always 180° (see section 4.3.2), which means leading by 180 ° is equivalent to lagging by 180 °. Apparently, the standard interpretation cannot be well applied to the results in this work.

6.3.1.2 VPFM Magnitude

It was also observed that the reactive domains in a VPFM magnitude image tended to show smaller VPFM magnitude responses than unreactive ones, as obvious in the examples shown in Fig. 6.1. This led to another hypothesis that domains with smaller VPFM magnitudes are more likely to be reactive than those with larger responses. The numbers of reactive and unreactive domains were counted and are plotted against their VPFM magnitudes for the bare $BiFeO_3$ (a) and the $TiO_2/BiFeO_3$ (b) in Fig. 6.4. The magnitudes were subdivided into four slots (<3, 3-4, 4-5, and >5 nA), and the numbers of reactive (unreactive) domains are given by red (blue) bars in Fig. 6.4 (with the actual number observed written as well).

For the 95 domains in the bare $BiFeO_3$, more than half (54%) of them (51) have PFM magnitudes < 3 nA. 92% of these domains (47 out of 51) with magnitude less than 3 nA are reactive. For the other 44 domains that had magnitudes > 3 nA, only 18 % were reactive (8 out of 44). Also, 85% of the total reactive domains (47

out of 55), had magnitudes < 3 nA. The probability that a domain with a small (large) VPFM magnitude is reactive in the bare $BiFeO_3$ substrate is high (low).

Two things can also be observed from the plot; both the total number of domains decreases quickly with increasing magnitude, and the relative ratio of reactive grains decreases quickly with increasing magnitude. The percentage of the total population for the 4 slots is: 54 % <3 nA, 32 % between 3-4 nA, 8 % between 4-5 nA, and 6 % above 5 nA. More to the point of reactivity, the relative ratio of reactive to unreactive grains drops as the magnitude increases: 23% (7 out of 30) are reactive in range of 3 ~ 4 nA, only 13% (1 out of 8) in range of 4 ~ 5 nA, and there are no reactive domains (0 out of 6) with magnitude greater than 5 nA (it should be noted that the error on the percentage is large for the latter two sets). It is apparent that the percentage of reactive domains decreases as the magnitude increases.

For the 161 domains in $TiO_2/BiFeO_3$, similar trends are observed, but an increased number of domains have higher magnitudes, and an increased proportion of those grains are reactive. Only 40 % (64) of all domains have PFM magnitudes < 3 nA, but 72% of these domains (46 out of 64) are reactive. For the other 60 % of domains (97) that had magnitudes > 3 nA, only 49 % were reactive (48). In the heterostructure, only 49% of the total reactive domains (46 out of 94), had magnitudes < 3 nA. While the probability that a domain with a small VPFM magnitude is reactive in the heterostructure is still high, the probability that a domain with a larger (> 3 nA) VPFM magnitude is not low, as compared to the bare substrate.

Two other things are apparent when compared to the bare substrate, there are relatively more domains with higher PFM magnitudes and the ratio of reactive ones to unreactive ones decreases more slowly as the magnitude increases. The percentage of the total population for the 4 slots is 40 % <3 nA, 21 % between 3-4 nA, 25 % between 4-5 nA, and 15 % above 5 nA. The chance of a domain being reactive is 72% (46 out of 64), 68% (23 out of 34), 47% (18 out of 38), and 28% (7 out of 25) for the four magnitude ranges in the increasing sequence. Although the overall trend is less significant than that for the bare $BiFeO_3$ substrate, the percentage of reactive domains decreases with increasing magnitude in the $TiO_2/BiFeO_3$ heterostructure.

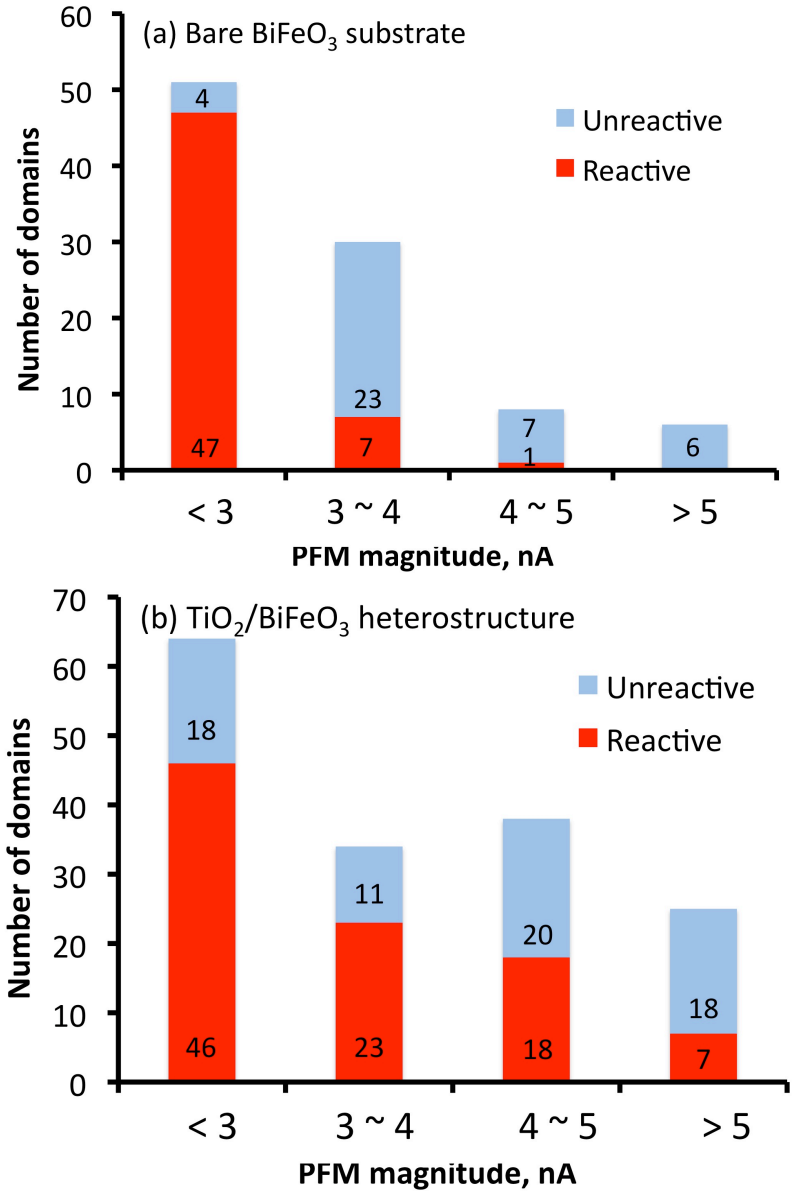

Figure 6.4 Plots of domain numbers against VPFM magnitude for (a) the bare $BiFeO_3$ substrate and (b) the $TiO_2/BiFeO_3$ heterostructure.

The goal of this work is to correlate the PFM signals to polarization, not simply the magnitude to reactivity. The magnitude is dependent on the frequency at which sample oscillates. The green curve in Fig 6.5 shows the resonance frequency dependence of the magnitude for a typical AFM tip contacting a neutral sample (domain) surface. The general curve is bell-shaped with the maximum at the first

harmonic frequency. According to Huey,[7] the position of the first harmonic is dependent on contact stiffness, which varies with a number of material properties, including type of material, crystallographic orientation, stress state, etc. In the case of VPFM on ferroelectric $BiFeO_3$, we speculate that the polarization influences the position of the first harmonic (though the bell-shaped nature is assumed to be similar for simplicity), and that different signs of polarization move the frequency in different directions from the neutral surface. Similar shifts in resonance frequency have been observed for $BaTiO_3$ nanowires[8] and PZT.[9] Prior works also suggest that stronger polarization results in larger shift.[9,10] The negative (positive) domain shifts the first harmonic to a lower (higher) frequency, as shown in Fig. 6.5.

In the experiments described above, all of the images were taken at an operation frequency of 70 kHz, which was less than the measured first harmonic frequency of ~ 75 kHz for the tip-surface interaction. In Fig. 6.5, this operational frequency is shown as a vertical dashed line. Given the shifts described above, a negative domain would then exhibit a larger magnitude at 70 kHz, while a positive domain would then exhibit a smaller magnitude at 70 kHz. In this scenario then, the correlation of the reactive domains to magnitudes signals arises from the correlation to polarization direction, with the polarization that lowers the magnitude (positive) being the more reactive polarization direction. Other factors also contribute to the response, but it is argued that the polarization dominates for the bare $BiFeO_3$ sample, and therefore a very strong correlation exists. These other factors are more important in the $TiO_2/BiFeO_3$ system, and therefore the correlation is weaker (but not absent) in the heterostructure.

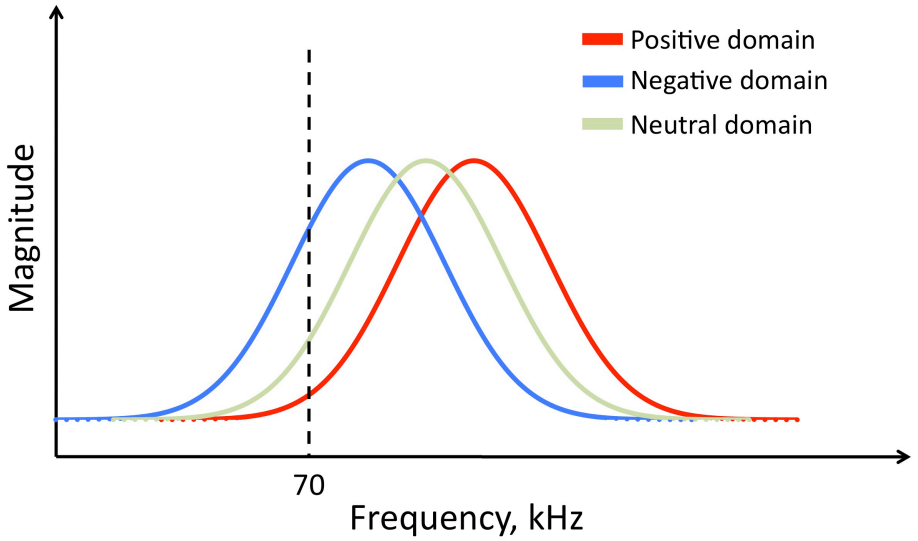

Figure 6.5 Schematic diagram of magnitude against frequency.

6.3.1.3 VPFM Summary

A strong correlation is observed between the VPFM magnitude and the reactivity of domains in the bare $BiFeO_3$ and the heterostructured $TiO_2/BiFeO_3$ substrates. For the bare $BiFeO_3$, domains with low VPFM magnitudes (< 3 nA), represent slightly more than half of all domains (54 %) and are very likely to be reactive (92% of domains <3 nA). For the $TiO_2/BiFeO_3$, domains with low VPFM magnitudes (< 3 nA), represent only 40 % of all domains and are likely to be reactive (72% if <3 nA). Furthermore, the probability of reactivity decreases with increasing magnitude. It is speculated that the low-magnitude domains are correlated with positive polarizations, but further work is needed to establish this correlation.

Unfortunately, it is difficult to determine the out-of-plane domain polarizations based on the VPFM phase angles on the bulk samples, though this is the more common approach reported in the thin-film $BiFeO_3$ literature. This can be understood from the complex response arising from the bulk polycrystal, but results here in the observation that the absolute VPFM phase is not clearly correlated to the reactivity of a domain. Still, reactive domains tend to (on average) lead unreactive domains in phase in bare $BiFeO_3$, and they tend to lag unreactive ones in the case of $TiO_2/BiFeO_3$. Focusing on the $BiFeO_3$, as described above, the standard interpretation implies that domains with phase at or near 0 ° are negative and those at or near ±180 ° are positive. But this does not work for the domain phase angles measured in Fig. 6.2 (a). Therefore, the combined data of absolute phase and magnitude to determine the polarity of a domain is as useful as the data of magnitude alone.

6.3.2 Boundary Pattern Approach

Compared to direct measurements of a PFM response, the Boundary Pattern approach to correlating polarization direction to reactivity is more complicated. It makes use of the orientation of the grains determined using EBSD and geometrical information about domain patterns in the VPFM images. The following example demonstrates the procedure.

The Euler angles of the example $BiFeO_3$ grain, whose VPFM phase and magnitude images were given in Fig. 6.6, were determined from its EBSD data using the TSL OIM Data Collection software (Mahwah, NJ) to be ϕ_1=240.9°, Φ=10.6°, ϕ_2=128.6°. After rounding up to integers, these Euler angles were converted to $(2\ \bar{2}\ 15)\ [13\ \bar{2}\ \bar{2}]$ in the form of (hkl)[uvw] using the software simulation function. Here, $(2\ \bar{2}\ 15)$ is the crystallographic representation of the habit plane in the $BiFeO_3$ pseudo-cubic lattice, and is only about 11 ° away from the low index plane (001); $[13\ \bar{2}\ \bar{2}]$ is the vector in the $(2\ \bar{2}\ 15)$ plane that forms a 90° angle clockwise with the scanning direction. $(2\ \bar{2}\ 15)$ is the plane shown in Fig. 6.6 and $[13\ \bar{2}\ \bar{2}]$ is the vector pointing vertically downward in both (a) and (b).

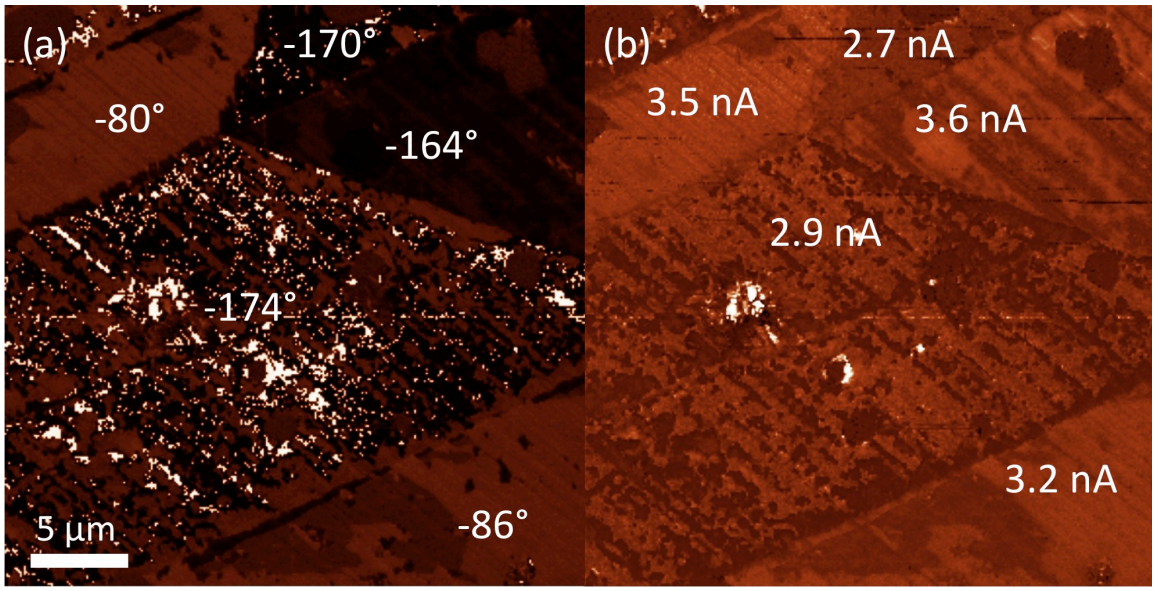

Figure 6.6 (a) VPFM phase image and (b) VPFM magnitude image of the example grain. Average phase and magnitude responses of the domains are shown. The contrast is 360° from bright to dark for the phase image in (a) and 8 nA from bright to dark for the magnitude image in (b).

Next, the angles of all possible domain boundary vectors in $(2\ \bar{2}\ 15)$ with respect to $[13\ \bar{2}\ \bar{2}]$ were calculated. The Miller indices of possible domain boundaries were summarized by Streiffer.[9] 71° boundaries are formed on (100), (010) and (001) planes, and 109° boundaries are formed on (110), (101), (011), $(1\bar{1}0)$, $(10\bar{1})$ and $(01\bar{1})$ planes. Their traces in VPFM images are straight. The 180° boundaries are usually not formed on a single plane and appear as curves in VPFM images. Nevertheless, a recent report shows that straight 180° boundaries also exist.[10] The calculated angles for all {001} and {011} boundary plane are listed in Table 6.1. Note that, since a vector of a domain boundary line in the surface plane is equivalent to its 180° rotation, each boundary line is associated with two angles.

Boundary plane	Calculated vector in surface plane	Angle with $[13\ \bar{2}\ \bar{2}]$, °
(100)	[0 15 2]	+100, -80
(010)	$[\overline{15}\ 0\ 2]$	+9, -171
(001)	$[\bar{2}\ \bar{2}\ 0]$	+54, -126
(110)	$[\overline{15}\ 15\ 4]$	+144, -36
(101)	$[\bar{2}\ 13\ 2]$	+108, -72
(011)	$[\overline{17}\ \bar{2}\ 2]$	+16, -164
$(1\bar{1}0)$	[15 15 0]	+54, -126
$(10\bar{1})$	[2 17 2]	+93, -87
$(01\bar{1})$	$[\overline{13}\ 2\ 2]$	+180, 0

Table 6.1 Vectors of domain boundary lines in the surface plane $(2\ \bar{2}\ 15)$ and angles between the vectors and $[13\ \bar{2}\ \bar{2}]$ for the example grain. Positive angles indicate counterclockwise rotation from $[13\ \bar{2}\ \bar{2}]$ and negative ones indicate clockwise rotation.

The angle between each domain boundary line and an imaginary vertical downward vector in Fig. 6.6 was measured. Because each angle in Table 6.1 is associated with a specific domain boundary plane, the Miller index for every domain boundary line could be determined by matching measured angles to calculated angles. The domain pattern in Fig. 6.6 was redrawn in Fig. 6.7. The boundary line at the lower right corner was approximately -64° away from the dashed vertically downward vector, measured using ImageJ. Because -64° was closest to -80°, this boundary was determined as (100). The 16° discrepancy came mainly from the misalignment of the EBSD and the VPFM lab references during sample mounting, and was consistently found for every domain boundary line in this image. All of the domain boundaries were labeled with the determined plane indices.

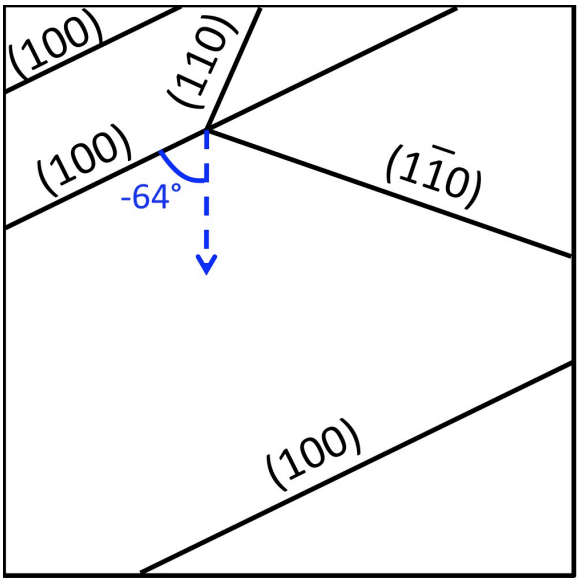

Figure 6.7 Determined domain boundaries in the example domain pattern.

With the determined domain boundaries, the next step was to assign a consistent set of polarization vectors for each domain. In ferroelectric $BiFeO_3$, there are four pairs of anti-parallel polarization vectors along four body diagonals of the unit cell, corresponding to eight distinct variants. They can be designated as <111> vectors in the unit cell. Each domain boundary plane can only be formed between certain polarization vectors,[9] as described below.

The 71° domain boundaries can only be formed on {110} planes, between polarization vectors that are not in the boundary planes. For example, the (110) plane can only exist between the polarization pairs $[111]/[1\bar{1}1]$and $[\bar{1}\bar{1}1]/[\bar{1}\bar{1}\bar{1}]$. Notice that the third index of (110) is zero, and that the sign of the third index in both pairs of polarization vectors is different. This is similar for (101) and (011) boundary planes. From the above analysis, it is established that a general rule to deduce the polarization vector of a domain next to a domain having a known polarization

vector and sharing a known {110} type of boundary plane is to change the sign of the index in the known polarization vector that corresponds to the index that is zero in the domain boundary plane.

The case of 109° domain boundary is similar. It can only be formed on {100} types of lattice planes, between polarization vectors that are not in the boundary planes. As an example, (100) domain boundary can only exist between the domain pairs $[111]/[1\bar{1}\bar{1}]$, $[11\bar{1}]/[1\bar{1}1]$, $[\bar{1}11]/[\bar{1}\bar{1}\bar{1}]$ and $[\bar{1}1\bar{1}]/[\bar{1}\bar{1}1]$. Notice that the second and the third indices of the (100) boundary are both zeros, and that the signs of the second and the third indices in each pair of the polarization vectors are different. This is also similar for (010) and (001) boundary planes. Therefore, a general rule to deduce the polarization vector of a domain next to a domain having a known polarization vector and sharing a known {100} type of boundary plane is to change the sign of the two indices in the known polarization vector that correspond to the indices that are zero for the domain boundary plane.

The most complicated case is the 180° domain boundaries. Apparently they are formed between reversed polarization vector pairs $[111]/[\bar{1}\bar{1}\bar{1}]$, $[11\bar{1}]/[\bar{1}\bar{1}1]$, $[1\bar{1}1]/[\bar{1}1\bar{1}]$ and $[\bar{1}11]/[1\bar{1}\bar{1}]$. Because the electric neutrality must be maintained at the boundary, both polarization vectors must have zero normal components at the boundary plane. Equivalently, both polarization vectors must be in that domain boundary plane. For example, domain boundary (hkl) can exist between $[111]/[\bar{1}\bar{1}\bar{1}]$ as long as $[hkl]\bullet[111]=0$ or h+k+l=0. The number of possible (hkl) is infinite, so the 180° domain boundary can be either a curve or a straight line in a general surface plane. Caution must be taken here that 180° boundary planes {hkl} can be {110}

planes, just as 71° boundary planes. A domain boundary is 180° in a VPFM image under two conditions: 1. it appears curvy; 2. it appears straight and the known polarization vector is in the domain boundary plane, e.g. $[111]$ and $(1\bar{1}0)$. The general rule to deduce the polarization of a domain next to a known domain sharing a 180° boundary is simply to reverse the known polarization vector.

Following the above rules, polarizations were assigned in the pattern in Fig. 6.7. For this example, there are eight consistent solutions that allow polarizations and boundary planes to result in physically reasonable configurations (they follow the rules above). These eight solutions are shown in Fig. 6.8, where the polarization vector is overlayed in boldface in the center of the domains. Note that the solution groups in Fig. 6.8 (a1-a4) and those grouped in Fig. 6.8 (b1-b4) are simply reversed solutions (opposite polarizations), respectively. The most common numbers of consistent polarization assignments for a given image were four and eight.

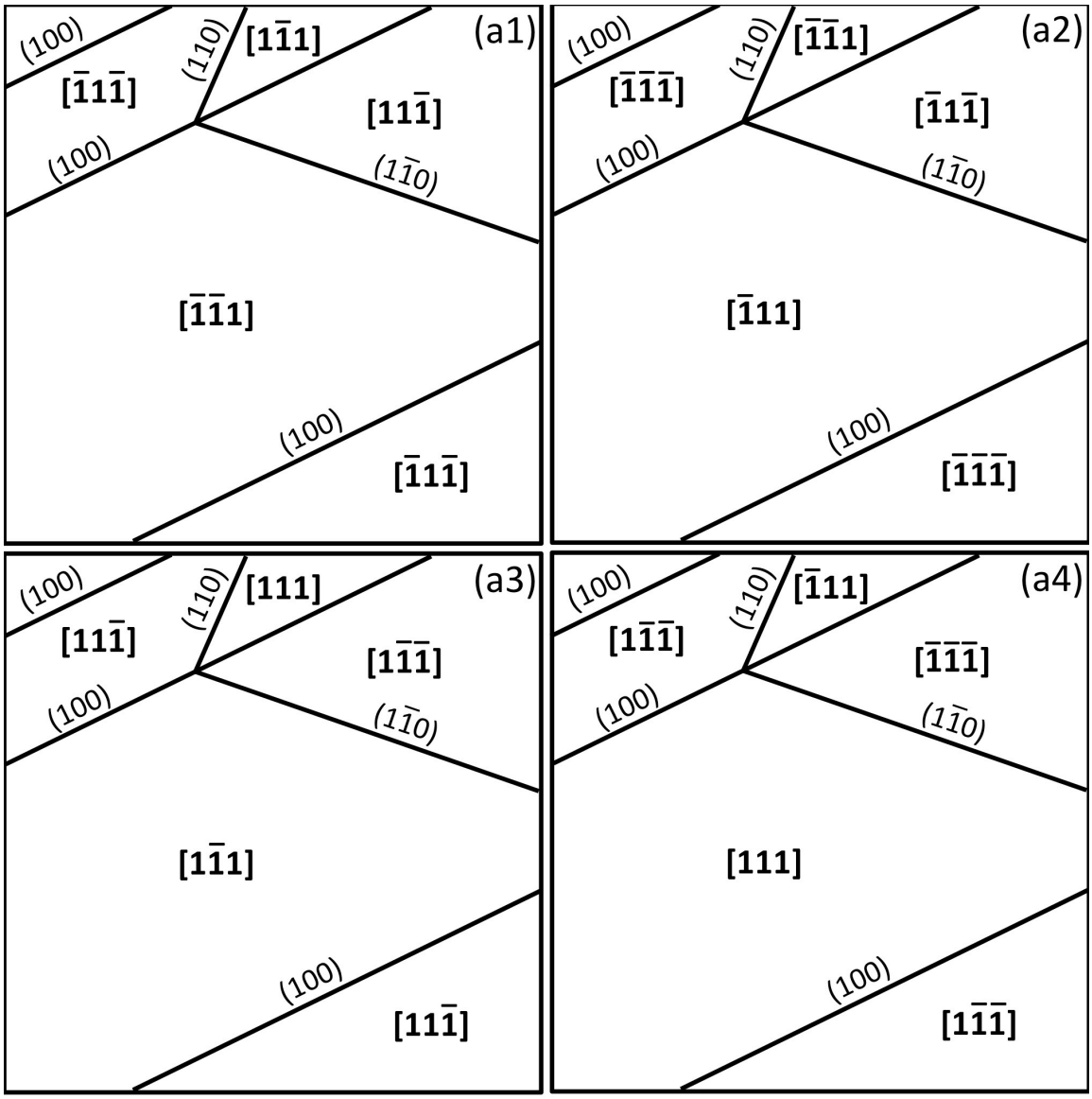
(a1)
(100)
(110)
[1$\bar{1}$1]
[$\bar{1}$1$\bar{1}$]
[11$\bar{1}$]
(100)
(1$\bar{1}$0)
[$\bar{1}\bar{1}$1]
(100)
[$\bar{1}$1$\bar{1}$]
(a2)
(100)
(110)
[$\bar{1}\bar{1}$1]
[$\bar{1}\bar{1}\bar{1}$]
[$\bar{1}$1$\bar{1}$]
(100)
(1$\bar{1}$0)
[$\bar{1}$11]
(100)
[$\bar{1}\bar{1}\bar{1}$]
(a3)
(100)
(110)
[111]
[11$\bar{1}$]
[1$\bar{1}\bar{1}$]
(100)
(1$\bar{1}$0)
[1$\bar{1}$1]
(100)
[11$\bar{1}$]
(a4)
(100)
(110)
[$\bar{1}$11]
[1$\bar{1}\bar{1}$]
[$\bar{1}\bar{1}\bar{1}$]
(100)
(1$\bar{1}$0)
[111]
(100)
[1$\bar{1}\bar{1}$]

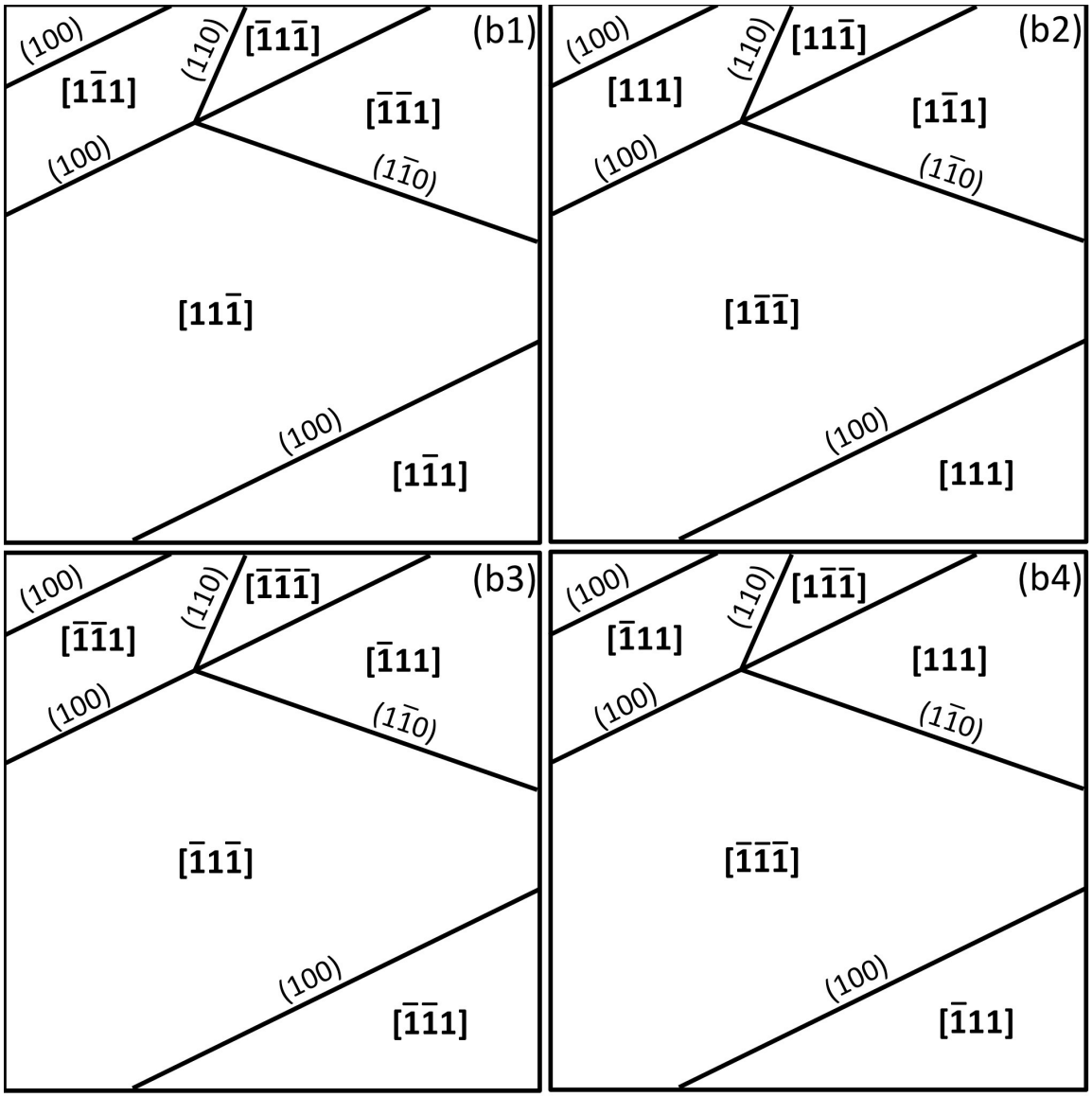

Figure 6.8 Eight solutions (a1-a4, b1-b4) to domain polarization assignment for the example. Indices by square brackets indicate polarization vectors. Indices by round brackets indicate domain boundaries.

The out-of-plane polarization vectors for the domains were calculated by projecting each domain vector to the out-of-plane surface normal $[2\ \bar{2}\ 15]$. When only the polarity of out-of-plane polarizations was concerned, each domain was assigned + or - to indicate whether its polarization was outward or inward in all eight solution patterns as shown in Fig. 6.9. The polarities of the domains shown in

Fig. 6.8 (a1-a4) are all represented in Fig. 6.9 (a), and the polarities of the domains shown in Fig. 6.8 (b1-b4) are all represented in Fig. 6.9 (b). Again, these two solutions represent the exact opposite assignment to the net polarity of the out-of-plane polarization. It should be immediately clear that this approach does not establish the absolute sign of the polarization in any given domain, but it does afford one to make correlations to reactive domains and the type of polarity across a given image.

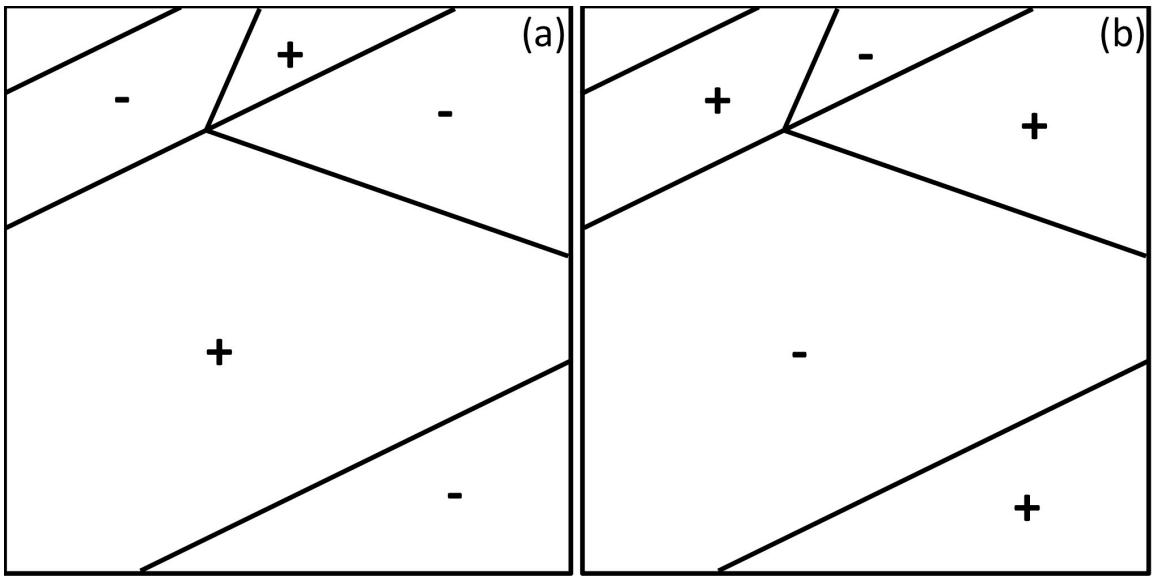

Figure 6.9 Two general solutions (a, b) from Fig. 6.8 with determined out-of-plane polarity of polarizations + or -.

The two solutions given in Fig. 6.9 were compared to the AFM topographic image of the reacted surface shown in Fig. 6.10. It was found that the Ag pattern was consistent with either solution, indicating that Ag particles were deposited only on domains of a specific polarity. For the bare $BiFeO_3$ substrate, 24 different locations were examined using this approach, and all of them have solutions that matched with the reduced Ag patterns, indicating that only one type of polarity per image

was active in silver reduction. For the $TiO_2/BiFeO_3$ heterostructure, 17 different locations yielded consistent out-of-plane polarity solutions, and all these solutions "matched" the silver pattern to a polarity. Collectively, these observations support that assertion that one type of polarity supports the reduction of Ag.

It is of interest to note that two other locations in the heterostructure yielded no consisten polarity solution owing to the existence of "triple junction points," as shown in the dashed white box in Fig. 6.10. At the "triple junction point", a curved 180° domain boundary line ends in the middle of a straight boundary line. Regardless of the type of that straight boundary line, there is no obvious assignment of polarizations that can satisfy such a domain structure. How such domains structures develop is beyond the scope of the current work, but this remains a challenging topic in the future to better understand the domain structure of $BiFeO_3$.

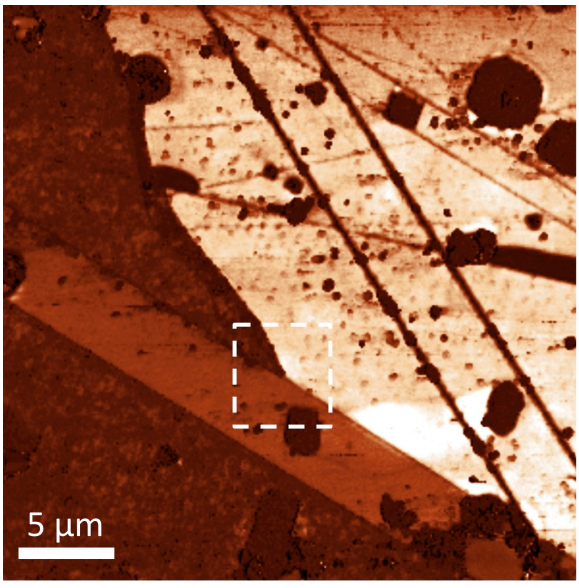

Figure 6.10 VPFM magnitude image of one grain without solution.

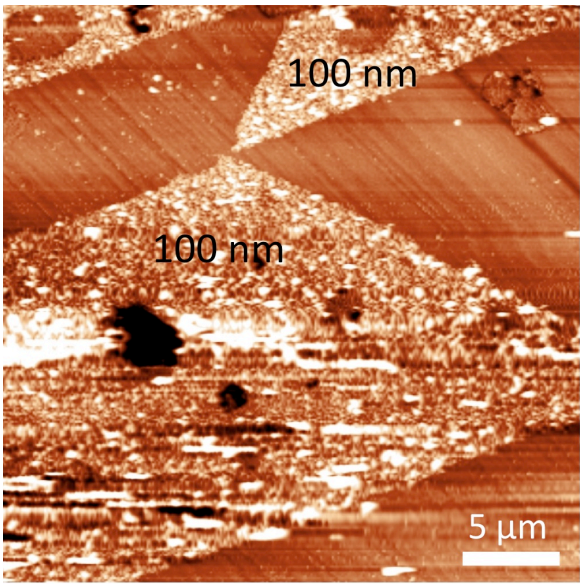

Figure 6.11 AFM topographic image of the example grain after Ag reduction reaction. Ag particles appear as bright features in a spatially selective pattern. The contrast is 500 nm from bright to dark.

The observations made using PFM, described in the previous section 6.3.1, indicated that reactive domains have lower VPFM magnitudes than unreactive domains. In this section, we made direct correlations between the crystallography and domain patterns indicating that the reactive domains are consistent with a single type of out-of-plane polarity. Comparison of Fig. 6.6 (b) and Fig. 6.11 shows that this grain is consistent with the prediction. It is of interest to combine these two sets of observations.

The strength of out-of-plane polarization for each assignment in Fig. 6.8 (a1-a4) can be calculated and normalized to the full strength along any {111} direction. The normalized out-of-plane polarization is shown in Fig. 6.12 (a1-a4) for the polarization vector maps shown respectively in Fig. 6.8 (a1-a4). Now, one can compare these maps to the VPFM magnitudes shown in Fig. 6.6 (b). It is suggested in

the literature (1) that polarization affects the magnitude response of VPFM,[8,9] and (2) that positive/negative shifts of the position of first harmonic are larger for larger out-of-plane positive/negative polarizations.[9,10] Therefore, the normalized out-of-plane polarization should decrease (its range being 1 to -1) as the measured VPFM magnitude increases. Indeed, a consistent solution is found: the one shown in Fig. 6.12 (a2). This correlation further corroborates the strong correlation observed in the VPFM magnitude response as a better indicator of the out-of-plane polarization than the phase response.

It should be pointed out that, distinguishing the consistent solutions of the polarization vectors to the VPFM magnitude images does not always result in a single solution. Many of the VPFM images have only two types of domains, as shown in Fig. 6.13 for a grain oriented along $(\bar{3}\ 10\ 37)$. In these cases, multiple solutions can be fitted to the amplitude maps. The important point in this work is that solutions that correspond to the proper crystallography of domains can also be correlated with the VPFM amplitude maps of domains and the reactivity of domains. These clear observations support the hypothesis that the polarization of the domain is the primary selector for grain reactivity, though the absolute polarization remains unclear. We speculate that these domains are the positive domains based on the frequency shift mechanism in Fig. 6.5.

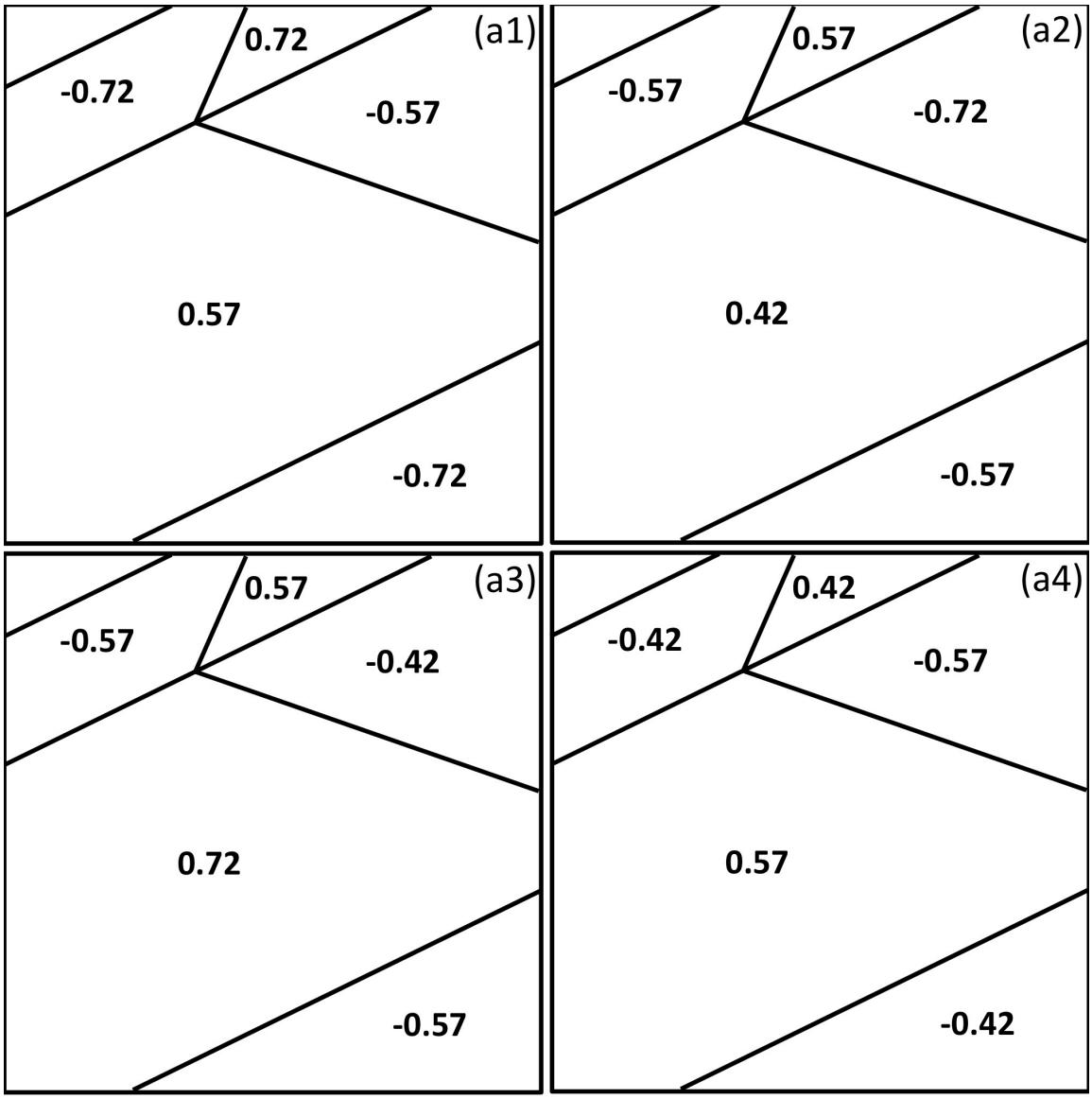

Figure 6.12 Domain patterns for the example grain with normalized out-of-plane polarization strength.

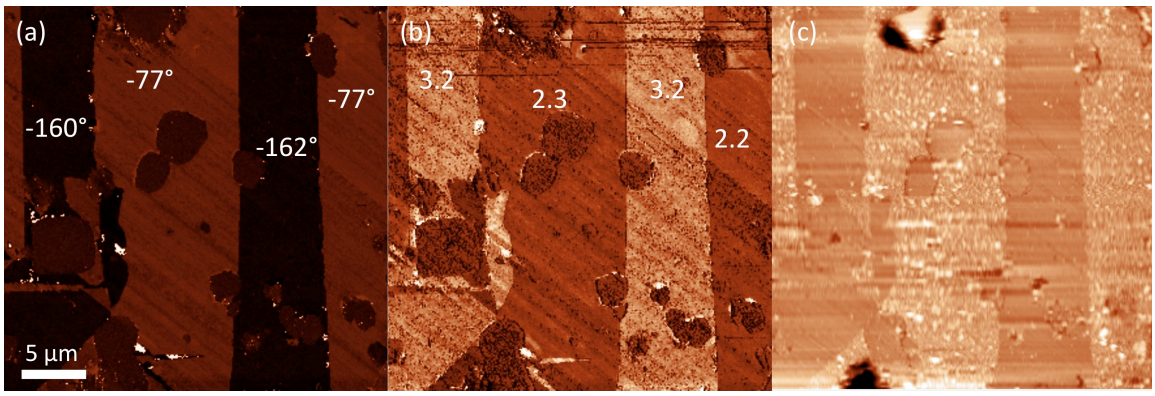

Figure 6.13 VPFM phase image, VPFM magnitude image, and AFM topographic image after silver reduction reaction of a grain for the bare $BiFeO_3$ sample (a, b, c). The contrast bar from bright to dark is 360° for (a), 5 nA for (b), and 500 nm for (c).

Part of the two data sets in this chapter will later be examined further in Chapter 8 together with data sets for a different bare $BiFeO_3$ substrate and a different $TiO_2/BiFeO_3$ to establish connections between grain orientation and reactivity.

6.4 Conclusion

Under the experimental conditions used in this work, the VPFM phase signal is not strongly correlated to the reactivity of a domain for either the bare $BiFeO_3$ substrate or the $TiO_2/BiFeO_3$ heterostructure. Statistical interpretation of the phase differences between reactive and unreactive domains suggest that the TiO_2 films invert the relative phase signal between the two specimens. While a correlation between the phase lead/lag of the reactive domains could be generated, the phase response was clearly complicated by the geometry of the overall bulk sample / domains in the polycrystal.

In contrast, a strong correlation existed for domains with low VPFM magnitudes, as they were considerably more likely to be reactive for both the bare $BiFeO_3$ (92% if <3 nA) and the TiO_2-coated $BiFeO_3$ (72% if <3 nA). This can be interpreted consistently assuming the direction of the polarization affected the first harmonic resonance frequency strongly (Fig. 6.5), resulting in low magnitudes for one polarization direction. We speculate this is the positive domain, similar to the cases of $BaTiO_3$ and PZT.[8,9]

By combing the VPFM maps with EBSD data of the grain orientations, consistent solutions were generated for the polarization vector in domains. Importantly, a consistent solution could always be found within the small subset of possible solutions, for which the reactive domains corresponded to a single-type of out-of-plane polarity (or its opposite). This was taken as strong evidence that all positive domains and all negative domains photochemically react the same way, which also supports the strong correlation made in the VPFM magnitude response and our proposed interpretation. It remains now to unambiguously determine the absolute sign of the polarization.

References:

[1]F. Zavaliche, S. Y. Yang, T. Zhao, Y. H. Chu, M. P. Cruz, C. B. Eom, and R. Ramesh, "Multiferroic BiFeO3 Films: Domain Structure and Polarization Dynamics," *Phase Transit,* **79**[12] 991-1017 (2006).

[2]B. J. Rodriguez, A. Gruverman, A. I. Kingon, R. J. Nemanich, and O. Ambacher, "Piezoresponse Force Microscopy for Polarity Imaging of GaN," *Appl. Phys. Lett.,* **80**[22] 4166-68 (2002).

[3]Z. Y. Wang, J. Hu, and M. F. Yu, "One-Dimensional Ferroelectric Monodomain Formation in Single Crystalline $BaTiO_3$ Nanowire," *Appl. Phys. Lett.,* **89**[26] (2006).

[4]A. Gruverman, J. S. Cross, and W. S. Oates, "Peculiar Effect of Mechanical Stress on Polarization Stability in Micrometer-Scale Ferroelectric Capacitors," *Appl. Phys. Lett.,* **93**[24] (2008).
[5]J. Guyonnet, H. Bea, F. Guy, S. Gariglio, S. Fusil, K. Bouzehouane, J. M. Triscone, and P. Paruch, "Shear Effects in Lateral Piezoresponse Force Microscopy at 180 Degrees Ferroelectric Domain Walls," *Appl. Phys. Lett.,* **95**[13] (2009).
[6]L. Yang and K. Dayal, "Real-Space Phase-Field Simulation of Piezoresponse Force Microscopy Accounting for Stray Electric Fields," *Model. Simul. Mater. Sci. Eng.,* **20**[3] (2012).
[7]B. D. Huey, "AFM and Acoustics: Fast, Quantitative Nanomechanical Mapping," *Annu. Rev. Mater. Res.,* **37** 351-85 (2007).
[8]W. S. Yun, J. J. Urban, Q. Gu, and H. Park, "Ferroelectric Properties of Individual Barium Titanate Nanowires Investigated by Scanned Probe Microscopy," *Nano Lett.,* **2**[5] 447-50 (2002).
[9]C. H. Ahn, T. Tybell, L. Antognazza, K. Char, R. H. Hammond, M. R. Beasley, O. Fischer, and J. M. Triscone, "Local, Nonvolatile Electronic Writing of Epitaxial $Pb(Zr_{0.52}Ti_{0.48})O_3/SrRuO_3$ Heterostructures," *Science,* **276**[5315] 1100-03 (1997).
[10]S. V. Kalinin and D. A. Bonnell, "Local Potential and Polarization Screening on Ferroelectric Surfaces," *Phys. Rev. B,* **63**[12] (2001).
[11]S. K. Streiffer, C. B. Parker, A. E. Romanov, M. J. Lefevre, L. Zhao, J. S. Speck, W. Pompe, C. M. Foster, and G. R. Bai, "Domain Patterns in Epitaxial Rhombohedral Ferroelectric Films. I. Geometry and Experiments," *J. Appl. Phys.,* **83**[5] 2742-53 (1998).
[12]Y. J. Qi, Z. H. Chen, C. W. Huang, L. H. Wang, X. D. Han, J. L. Wang, P. Yang, T. Sritharan, and L. Chen, "Coexistence of Ferroelectric Vortex Domains and Charged Domain Walls in Epitaxial $BiFeO_3$ Film on $(110)_o$ $GdScO_3$ Substrate," *J Appl Phys,* **111**[10] (2012).

Chapter 7 Orientation relationships of TiO_2 and $BiFeO_3$

7.1 Introduction

The orientation relationships (ORs) of TiO_2 and $BiFeO_3$ are investigated in this chapter. In chapter 5, TiO_2/$BiFeO_3$ heterostructures were shown to exhibit spatially selective reactivity under visible light illumination, which do not initiate photochemical reactions with bulk TiO_2 and TiO_2/$BaTiO_3$ heterostructures. In Chapter 6, we showed that the out-of-plane polarity of the domains in $BiFeO_3$ had a strong correlation with reactivity of the bare substrate and the heterostructure. Besides polarity, the orientations of both TiO_2 and $BiFeO_3$ may affect the activity of the specimens (see section 2.3.3.1 & 2.3.3.2). For the bulk substrate, this is generally straightforward using EBSD mapping.[1,2] On the other hand, this is more challenging for the TiO_2 film as the orientation and phase of an ultra thin (10 nm) TiO_2 could not be directly determined using the EBSD in the lab. Instead, the titania orientations of thin films could be deduced from the orientations of the $BiFeO_3$ substrate, if clear and consistent orientation relationships (ORs) can be established between the film and substrate.

The question of determining or predicting orientations of films growing on general high-index surfaces is of general interest to the film growth community, but there is little information available for hetero-polymorphic film growth on general surfaces. Moreover, since titania has a well-known competition between the rutile and anatase polymorphs, especially when grown as films on perovskites,[1] one must take care to determine both phase and orientation when depositing on general

polycrystals. We have largely become interested in this approach to control for phase and orientation when interpreting reactivity in high-throughput physical property measurements (as described in Chapters 5, 6, and 8). This was recently established as a viable method for doing the same in $TiO_2/BaTiO_3$ photochemical systems.[2]

That approach was generalized further herein, and we call this general technique Combinatorial Substrate Epitaxy (CSE). CSE is developed in this chapter to determine the ORs using EBSD data of each grain in a heterostructure having a thick (100 nm) TiO_2 film on a $BiFeO_3$ substrate. Based on the calculation of angles between crystallographic vectors (e.g. $[100]$ in TiO_2 and $[100]$ in $BiFeO_3$) in each pair of the grains, we establish that the majority of epitaxial grains exist in a small subset of possible orienations: we describe the one important OR for anatase/$BiFeO_3$ and the two for rutile/$BiFeO_3$. The phase boundary for anatase and rutile is clearly delineated, as is the instability of (111) surfaces for epitaxial growth. The contents of this chapter are derived from the published paper,[3] and are expounded on later (Chapter 8) to demonstrate that phase and orientation are less important actors than polarization (Chapter 6) in determining the reactivity of the heterostructures.

7.2 Experimental

At first, the orientation of each grain within an area of approximately 1.2 × 1.2 mm^2 on the surface of the $BiFeO_3$ substrate was determined using EBSD. After a 100 nm thick TiO_2 film was deposited using PLD, the orientation of each grain within the same area in the TiO_2 film was determined using a similar EBSD

procedure.

The procedure for finding the ORs begins by manually matching substrate grains with film grains by visual inspection of orientation maps, such as those shown in Fig. 7.1. For example, based on the similar position and shape, one can deduce that the grains marked by the same symbols (A–D) on the substrate (Fig. 7.1 (a)) and in the film (Fig. 7.2 (a)) correspond to pairs. This makes it possible to create a list of matched pairs, in which the unique "grain identification numbers" assigned arbitrarily by the TSL software to associate the substrate/film pairs. For this study, 150 substrate grain pairs were identified.

The remainder of the analysis is automated and based on the list of matched grain identification numbers. The orientation maps can be exported from the TSL software as text files that list the coordinates, orientation (in the form of Euler angles), phase, and grain identification number for every point in the map. A program developed in our lab (get_pairs) searches these files for grain identification numbers in the pre-established list of matched pairs and records the Euler angles for the corresponding substrate and film grains. Both the raw data and the software (CSE_software_v1.0) for all operations are provided at URL http://dx.doi.org/10.1016/j.actamat.2012.07.060

A second program (ORs) allows the ORs to be determined in the following way. The user selects a trial direction in the crystal reference frame of the substrate and another in the crystal reference frame of the film. For each substrate/film pair, these directions are transformed to the laboratory reference frame. The angle between these directions is then computed for each pair. In the calculation of the

angle between the directions, it is important to recognize the crystal symmetry in each phase. In the calculation, the angles between all possible pairs of crystallographically indistinguishable directions are computed and the minimum angle is selected. As long as the film is epitaxial on the substrate, then the minimum angle between the two reference directions is constant in all of the substrate/film pairs. It is relatively simple to find the directions with the minimum misalignment, and this specifies one component of the OR. The process is repeated for directions perpendicular to the aligned axes to find the second component of the OR. An example of this procedure will be illustrated in the section 7.3.

7.3 Results and Discussion

A representative portion of the orientation and phase data is shown in Fig. 7.1 and Fig. 7.2. In Fig. 7.1, the regions of constant color are grains with a constant orientation in the substrate. The average grain size in the substrate is approximately 50 μm, determined from spherical equivalent diameter of the grain areas. The orientation map for the film is shown in Fig. 7.2(a) and contains orientations for both anatase and rutile grains; both crystals belong to tetragonal systems whose orientations are indicated by colors given by the same inset stereographic triangle. The locations indexed as rutile (anatase) TiO_2 are shown in green (red) in Fig. 7.2(b). The black areas in Figs. 7.1 and 7.2(a, b) are regions where there was low (<0.1) confidence in the indexing. The large black cross is the fiducial marker scratched into the surface. More than 95 % of the substrate area was indexed with good confidence. The remaining poorly indexed areas usually corresponded to

pores or inclusions of other phases. The distribution of colors in Fig. 7.1 indicates that there is no preferred orientation in the substrate.

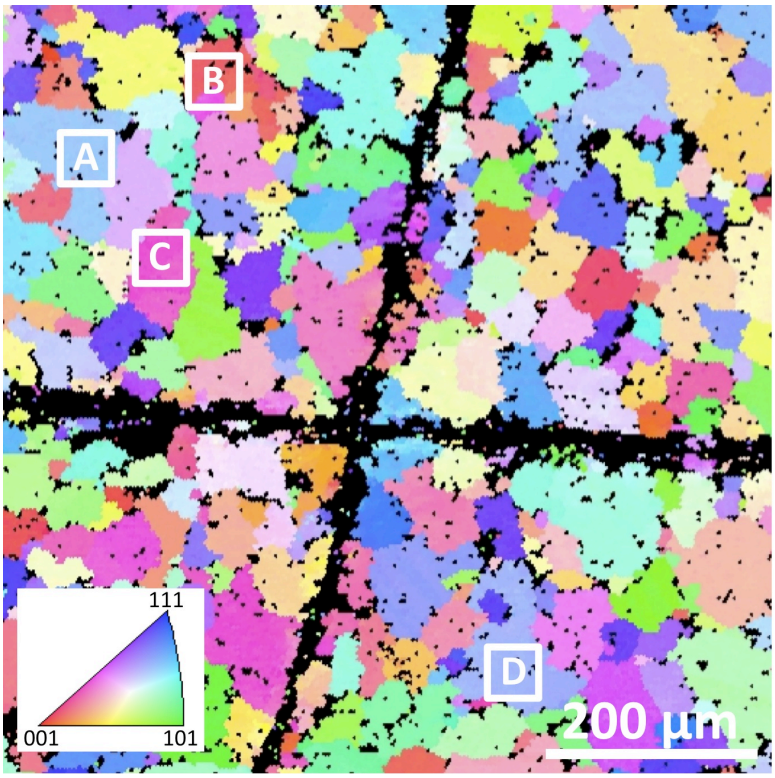

Figure 7.1 The orientation map of the $BiFeO_3$ substrate. The colors show the orientations of the grains with respect to the surface normal, according to the stereographic projection given in the inset triangle. Black color indicates unidentifiable areas. The grains marked with symbols (A, B, C, and D) are grains matching to the marked grains in Fig. 7.2.

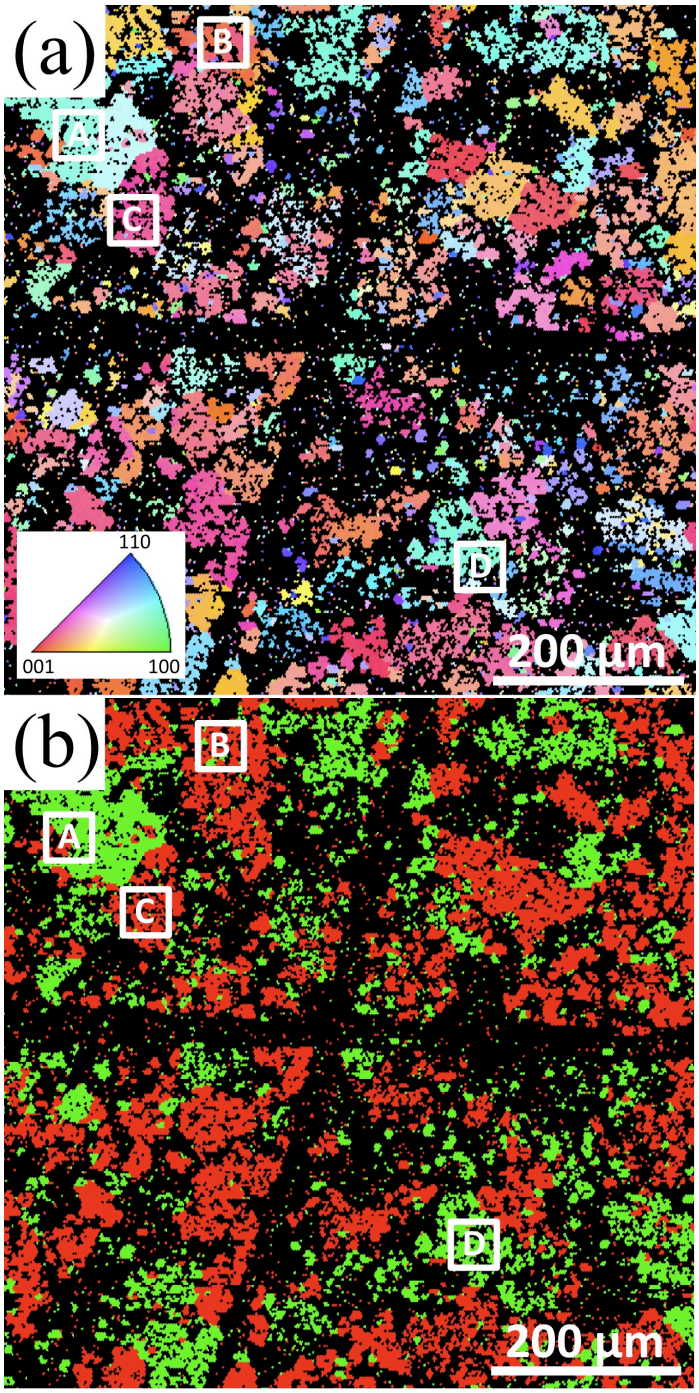

Figure 7.2 (a) The orientation map of the TiO_2 film registered on the same area of the substrate given in Fig. 7.1. Surface normal orientations of anatase and rutile are shown by the colors in the inset triangle. (b) The phase map of the TiO_2 film from the same area as that in (a). Red indicates anatase grains, green indicates rutile grains. In both maps, black indicates unidentifiable areas and the grains marked with the same symbols (A, B, C, and D) are grains matching to the marked grains in Fig. 7.1.

Fig. 7.3 shows examples of EBSD patterns registered from the substrate and the film for comparison. As expected, the EBSD patterns registered from the film were found to generally be of poorer quality than those from the substrate. The EBSD patterns for both of anatase and rutile TiO_2 are more diffuse than the one for the $BiFeO_3$ substrate. Local strain, defects, and possible mosaicity in the local orientation in the epitaxial layer are likely factors that contribute to the reduced quality of the patterns from the film, which results in an increased number of unindexable points. A second source of unindexed points would be the existence of nanosized grains of different orientations (including potentially degenerate in-plane orientations of the same out-of-plane orientation) interfering with each other's pattern. If a single substrate grain supports film grains that have multiple orientations and sizes comparable to or less than the beam resolution (approximately 20 nm in an ideal sample[4] and probably lower here), it will not be possible to assign reliable orientations to the patterns. Even if a few points in such a region are reliably indexed, contiguous areas with a consistent orientation are needed to make a reliable correlation to a supporting substrate grain. These factors combined lead to only about 70 % of the orientations being indexed reliably in the film, as compared to more than 95 % of the orientations in the substrate. Notice that a large portion of the unindexed regions in the film corresponds to the substrate grains oriented near (111). This ratio of indexed grains is sufficient to explore the preferred relationships between substrate grain orientation and film phase / orientation, though we need to determine if correlations exist between the film indexability and the substrate orientation.

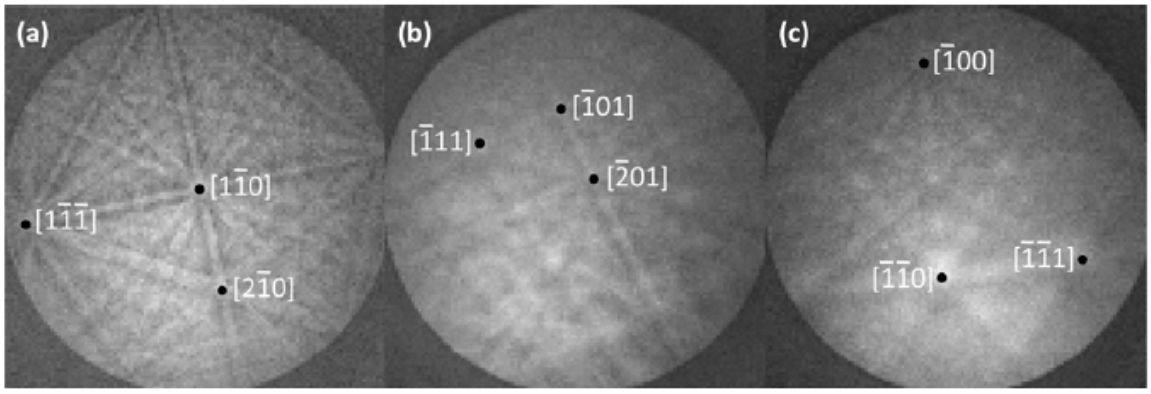

Figure 7.3 Sample EBSD patterns for (a) a $BiFeO_3$ grain in the substrate (ϕ_1 = 189°, Φ = 84°, ϕ_2 = 184°), (b) an anatase TiO_2 grain (ϕ_1 = 48°, Φ = 15°, ϕ_2 = 155°) and (c) a rutile TiO_2 grain (ϕ_1 = 180°, Φ = 82°, ϕ_2 = 290°) in the film.

Fig. 7.4 is a summary of the 150 pairs of well-indexed substrate/film orientations. The standard stereographic triangle in Fig. 7.4 (a) includes all distinguishable orientations in the cubic system, i.e., in the substrate reference frame. Within this triangle, information concerning the film found at that substrate orientation is given. Substrate orientations on which anatase was identified are marked with open circles. Substrate orientations on which rutile was identified are marked with either an open or a closed square. Substrate orientations on which anatase or rutile outlier was identified are marked with an additional x. There is a clear separation between the $BiFeO_3$ orientations that support the growth of anatase and those that support the growth of rutile. There is a band in which the measurements overlap, but considering that the typical orientation resolution in EBSD is ± 2 °,[4] this is not unexpected even if the underlying correlation was sharper. Grains orientated within 35 ° of $[001]_{BFO}$ support the growth of anatase while those closer to the $[101]_{BFO}$ and $[111]_{BFO}$ directions support the growth of rutile. Note that

there is an empty region near $[111]_{BFO}$. The absence of reliably and consistently indexed film grains in this region account for a large portion of the missing 25 % of indexable area for the film, as most of the unindexed regions in the film correspond to the areas of $BiFeO_3$ (111) grains in the substrate.

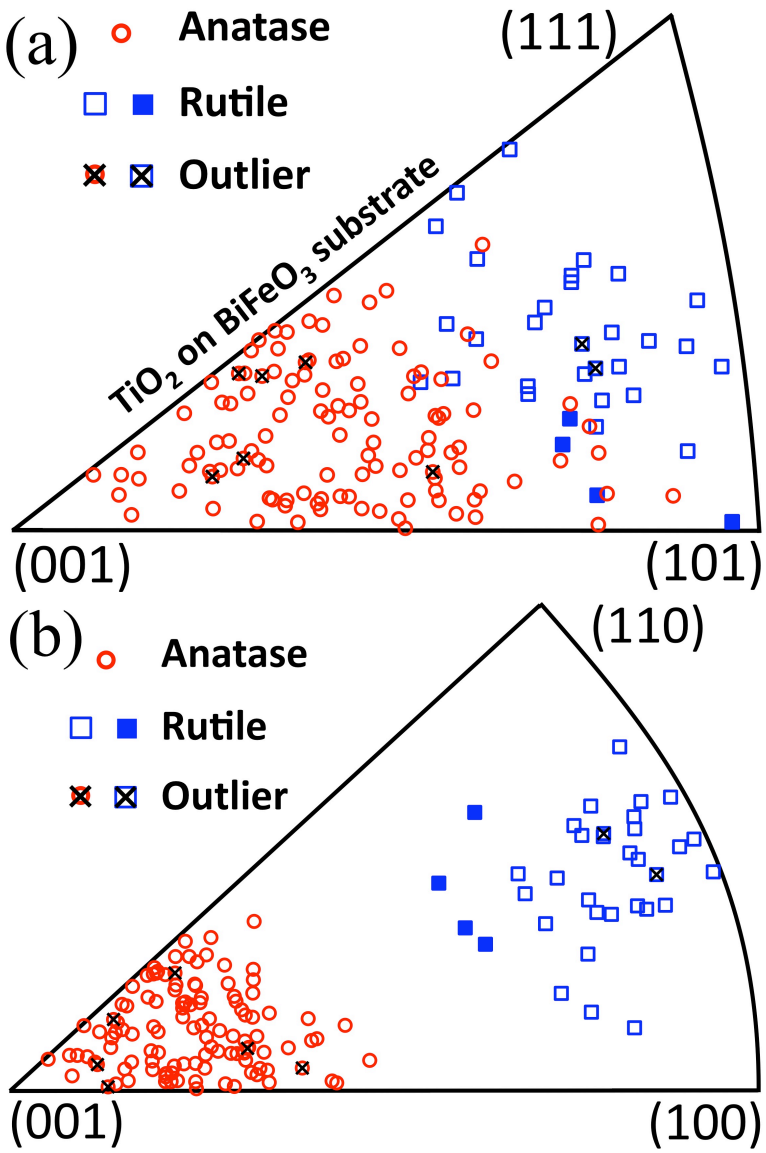

Figure 7.4 (a) Orientations of $BiFeO_3$ grains that supported epitaxial TiO_2 growth in the standard stereographic triangle for the cubic system. (b) Orientations of anatase/rutile TiO_2 grains in the standard stereographic triangle for tetragonal systems. Red symbols mark orientations that supported anatase and blue mark those that supported rutile. Black x's mark outliers whose orientations are not consistent with the majority.

After a careful manual inspection of TiO_2 film on a $BiFeO_3$ grain oriented near $(111)_{BFO}$, three EBSD patterns were observed in distinct locations within the same grain as shown in Fig. 7.5. All of them are for rutile, but they do not suggest a consistent OR. Therefore, it was concluded that $BiFeO_3$ grains near $(111)_{BFO}$ support growth of polycrystalline rutile, though why epitaxy was not observed is unclear.

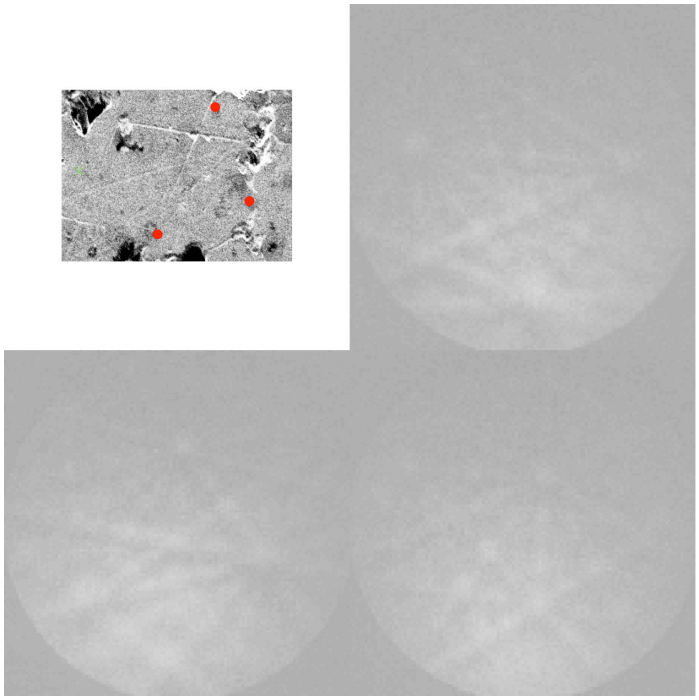

Figure 7.5 SEM image of a $BiFeO_3$ grain oriented near (111) and three EBSD Kikuchi patterns at different locations within the grain pinpointed by the red dots.

Regarding the outlier (with x) anatase grains, they are scattered among the orientations allowing anatase growth. As for the two outlier rutile grains, even though they are next to each other, they are closely mixed with other points having consistent ORs in the triangle. No conclusion of preferred location of outliers in the orientation triangle can be drawn.

The orientations of all of the indexed films are illustrated in Fig. 7.4 (b). In this case, the stereographic triangle includes all distinguishable orientations in the tetragonal system. Again, all of the anatase orientations are denoted with red circles, all of the rutile orientations are denoted with blue symbols, and the outliers are denoted with additional black x's. These data provide some information about the orientation relations. The anatase that grows on $BiFeO_3$ in the vicinity of [001] is also clustered near the anatase [001] orientation. The rutile that grows on other orientations of $BiFeO_3$ has orientations that are nearly perpendicular to [001]. The locations of the anatase and rutile outliers are scattered in this triangle. The data in Fig. 7.4 (b) also makes it clear that not all orientations of rutile and anatase can be grown epitaxially on $BiFeO_3$.

To determine the ORs, one starts by comparing the alignment of the closest-packed planes. Both the perovskite structure and the anatase structure can be considered as consisting of cubic close-packed arrangements of oxygen ions. In perovskite, the closest-packed planes are (111) and the analogous planes in anatase are (112). The angle between these two planes for the 115 substrate/anatase pairs is shown in Fig. 7.6 (a), where the horizontal axis is simply the order in which the data were recorded. The average misorientation (standard deviation) for the majority of the pairs is 2.6 ° (1.2 °). The same calculation was repeated for the perpendicular $[1\bar{1}0]$ axes. In this case, 110 of the substrate/film pairs have $[1\bar{1}0]$ axes misoriented by an average angle (standard deviation) of 3.2 ° (1.8 °). Therefore, based on 96% of the observations, we assign the OR to be $(112)_A \parallel (111)_{BFO}$ and

$[1\bar{1}0]_A$ || $[1\bar{1}0]_{BFO}$, regardless of the interface plane normal. While the observed average misorientations are not exactly zero, it is reasonable that deviations of a few degrees would result from a combination of experimental uncertainty in the orientation measurements and misalignment of the sample during the two measurements. Note that there are some obvious outliers in Fig. 7.6. These points are marked by black x's in Fig. 7.4. All five of these points could be described (with an average misorientation of 8 °) to have an OR of $(100)_A$ || $(210)_{BFO}$. This may be a secondary OR that is occasionally stabilized during growth, but was not investigated further.

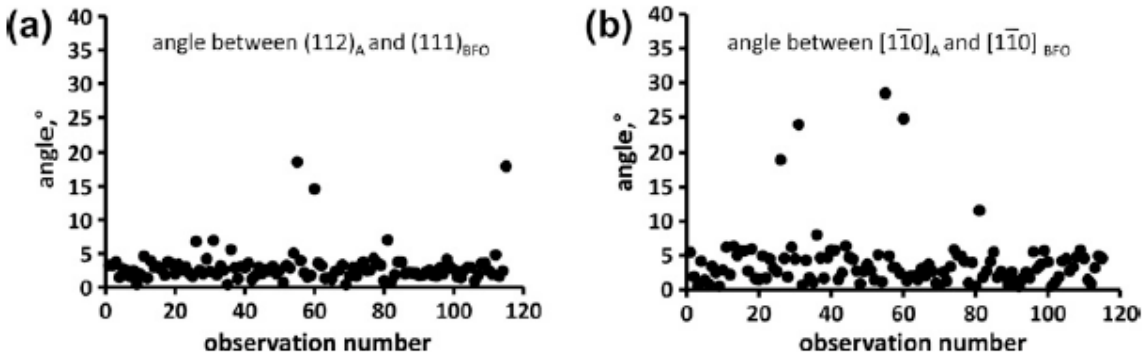

Figure 7.6 Angles between low index substrate and film orientations. (a) Angle between $(112)_A$ and $(111)_{BFO}$, (b) Angle between $[1\bar{1}0]_A$ and $[1\bar{1}0]_{BFO}$.

The process was repeated for the 35 observed substrate / rutile pairs. The results, shown in Fig. 7.7, indicate two ORs. First, the angles between [111] in $BiFeO_3$ and [100] in rutile are shown in Fig. 7.7 (a). The average of these angles is 1.3 ° and there are two significant outliers. Next, looking at perpendicular axes, we find that nearly all of the $[1\bar{1}0]$ axes in $BiFeO_3$ are, on average, 3 ° from the [001] direction in rutile. However, there are six significant outliers, two that showed significant deviations in Fig. 7.7 (a) and four others. The four new outliers have some

characteristics in common. First, they are in the same region of orientation space, near the border between the anatase field and the rutile field (these are the points indicated by the solid squares in Fig. 7.4). Second, they have an approximately 30 ° misorientation from $[1\bar{1}0]$. Noting that the $[\bar{1}2\bar{1}]$ direction is also in the (111) plane and 30 ° from $[1\bar{1}0]$, the angles between $[\bar{1}2\bar{1}]$ and $[001]$ were calculated. For the four points in question, the average angle between $[\bar{1}2\bar{1}]$ and $[001]$ is 1.8 °. From these observations, we conclude that there are two ORs. The dominant relationship representing 83% of the substrate/grain pairs is $(100)_R \,||\, (111)_{BFO}$ and $[001]_R \,||\, [1\bar{1}0]_{BFO}$.

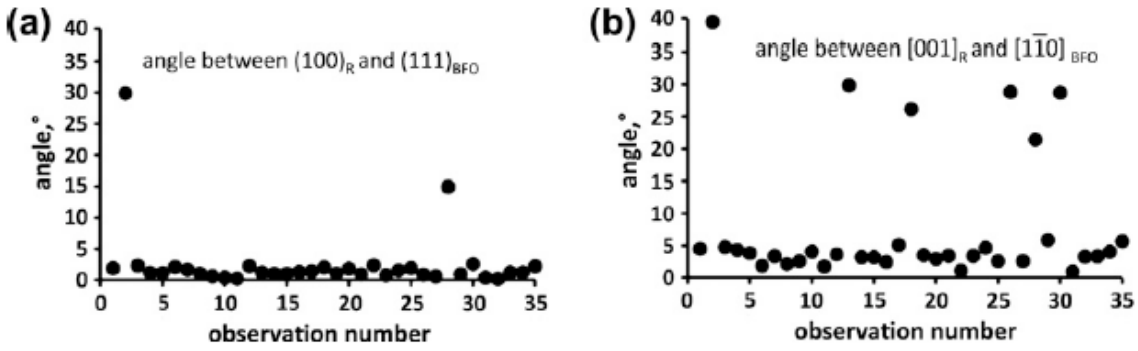

Figure 7.7 Angles between low index substrate and film orientations. (a) Angle between $(100)_R$ and $(111)_{BFO}$, (b) Angle between $[001]_R$ and $[1\bar{1}0]_{BFO}$.

As for the case of anatase, approximately 5% of the observations (two cases) are outliers. These points are marked by black x's in Fig. 7.4. Calculations show that for these two cases, $(100)_R \,||\, (210)_{BFO}$ are misaligned by an average of 6 ° ± 1 °. However, as before, these minority observations were not considered further.

The $BiFeO_3$ structure can be thought of a cubic close packed (ccp) network of

BiO_3 atoms, with Fe in one-quarter of the octahedral interstices. Anatase can be thought of as a ccp network of O with Ti in one-half of the octahedral interstices. Rutile can be thought of as a hexagonally close packed (hcp) network of O with Ti in one half of the octahedral interstices. Considering these nearly closest-packed (eutactic) networks,[5] the dominant observed ORs can be interpreted as having parallel closest-packed planes and closest-packed directions, as illustrated in Fig. 7.8 (a) and (b). For example, anatase can be thought of as two (distorted) ccp cells stacked along the [001] direction. Therefore, the closest-packed planes of O atoms are (112) and this is the plane that is parallel to (111) in $BiFeO_3$. The closest-packed directions in both of these planes are $[1\bar{1}0]$ and these directions are also aligned (see Fig. 7.8 (a)). Rutile has its closest-packed layers in (100) planes that are stacked in an hcp sequence; these layers are parallel to the closest-packed (111) plane of the substrate. In this case, the ABC stacking of close-packed layers in $BiFeO_3$ changes to AB stacking of the layers in rutile. Therefore, the vast majority of the observed ORs can be described by saying that the closest-packed planes in the substrate and film are parallel and, within these planes, the closest-packed directions are parallel.

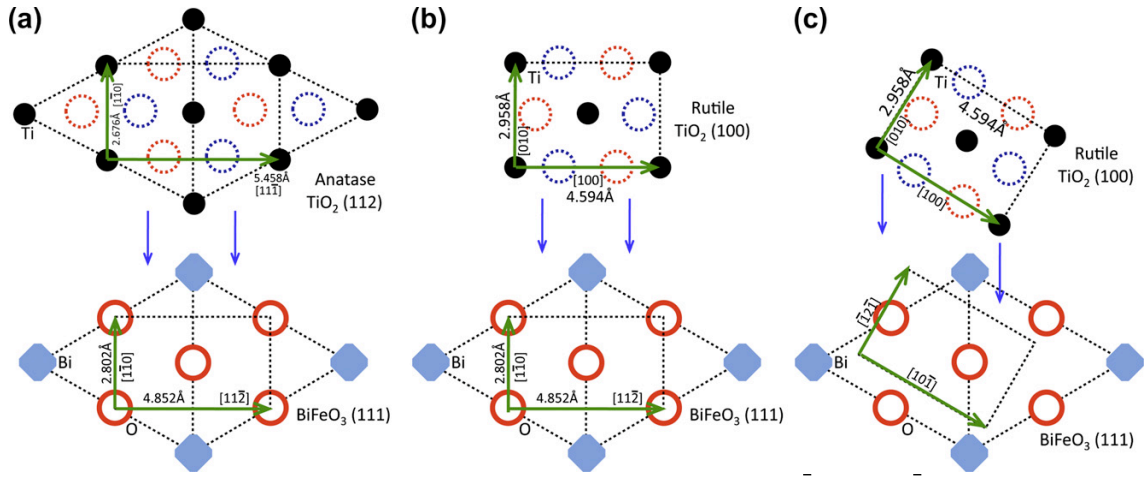

Figure 7.8 (a) Schematic of the OR $(112)_A$ || $(111)_{BFO}$ and $[1\bar{1}0]_A$ || $[1\bar{1}0]_{BFO}$. (b) Schematic of the OR $(100)_R$ || $(111)_{BFO}$ and $[001]_R$ || $[1\bar{1}0]_{BFO}$. (c) Schematic of the OR $(100)_R$ || $(111)_{BFO}$ and $[001]_R$ || $[\bar{1}2\bar{1}]_{BFO}$. In all drawings, light blue diamonds, red circles with complete lines, and black circles are Bi, O and Ti, respectively. The dashed blue circles are O in the closest-packed layer above the plane and the dashed red circles are O in the closest-packed layer below the plane.

For the growth of anatase on perovskite substrates, the OR is usually reported as $(001)_A$ || $(001)_P$ and $[100]_A$ || $[100]_P$ for growth on (001) substrates[2,6-14] and $(012)_A$ || $(110)_P$ and $[100]_A$ || $[001]_P$ for growth on (110) substrates.[10,15-18] Although the indices of the planes for both ORs differ from one another and from our assignment, all three are essentially identical from a crystallographic perspective. In other words, when $(112)_A$ || $(111)_{BFO}$, this brings the (012) plane of anatase parallel to the (110) plane of perovskite. It also brings the two (001) planes into near-perfect alignment. To demonstrate that our data support all three descriptions, the angles between the $(112)_A$ and $(110)_{BFO}$ planes were calculated for the 115 substrate anatase pairs; the average misorienation (standard deviation) was 2.8 ° (1.3 °). When the analysis is repeated for $(100)_A$ and $(100)_{BFO}$ the average

misorienation (standard deviation) was 2.5 ° (1.4 °), and for $(001)_A$ and $(001)_{BFO}$ the average misorienation (standard deviation) was 7.3 ° (2.4 °). In other words, our experiments on high-index surfaces of $BiFeO_3$ are consistent with previous growth experiments on (001) and (110) perovskite substrates. However, it is argued here that describing the OR as $(112)_A$ || $(111)_{BFO}$, and $[1\bar{1}0]_A$ || $[1\bar{1}0]_{BFO}$ is preferred because it emphasizes the continuity of the closest-packed networks.

For the growth of rutile on perovskite, the alignment of the closest-packed planes makes $(100)_R$ parallel to $(111)_{BFO}$ for 33 of 35 of the observed pairs. This is consistent with results reported for rutile grown on other perovskite structured compounds.[2,14,16,17] Two possible in-plane orientations have been identified here. In one case, the rutile c-axis, $[001]$, is parallel to the $[1\bar{1}0]$ axis which aligns the closest-packed directions in the substrate and film. For this majority observation (83%), the epitaxy is again described as an alignment of the closest-packed planes and directions. For the minority (12%) OR, the $[001]$ axis of rutile is parallel to the $[\bar{1}2\bar{1}]$ axis of $BiFeO_3$. These two arrangements are depicted schematically in Fig. 7.8 (b) and (c). The observation of two in-plane ORs indicates that they compete with one another during nucleation and the prevalence of the former indicates that a continuation of the closest-packed arrangement is preferred. That they both still align closest-packed planes indicates that they are low-energy nucleation events. That the minority observation exists near the phase boundary of anatase and rutile indicates that the majority OR in rutile is less competitive in the nucleation process at these surface orientations. However, it should also be noted that the low number of observations makes it difficult to interpret at this time.

One puzzling aspect of the results presented here is that for $BiFeO_3$ substrate grains oriented within 10 ° of (111), the growth was polycrystalline and did not exhibit an obvious orientation relationship; considering that 94% of the grains had an OR with $(100)_R$ || $(111)_{BFO}$, one would expect epitaxial films with the same OR at the $(111)_{BFO}$ orientation. In fact, it is well known that this OR is observed on other perovskite (111) single-crystal substrates.[14,16,17] The data available here do not suggest an explanation for this observation, and, in fact, this is not the goal of this work. However, one might speculate that there is some instability in the $BiFeO_3$ (111) surface at the growth temperature that leads to poor growth. Selbach *et al*.[19] reported that when $BiFeO_3$ is heated at 600 °C for 30 min, the formation of $Bi_{25}FeO_{39}$ and $Bi_2Fe_4O_9$ can be detected in the X-ray diffraction patterns. The substrates in this study were annealed at this temperature to heal polishing damage before growth and this was also the nominal growth temperature. Therefore, it is possible that (111)-oriented surfaces decompose preferentially and this leads to surfaces unsuitable for epitaxial growth.

While the ORs that we identify are consistent with previous studies of titania epitaxy on perovskite, it is important to emphasize the vast majority of the observed substrate/film pairs did not share the low-index interface planes characteristic of the previous work. One might argue that even though high-index surfaces are used as substrates, they could be microfaceted and that growth actually nucleates on low-index terraces and then spreads across the entire grain surface. To test this idea, the substrate surfaces were imaged by AFM. However, because no clear facets were observed, the results were inconclusive (the negative observation does not rule out

the possibility of nanostructured facets beyond the resolution of the AFM). The best evidence for the existence of terraces is illustrated in Fig. 7.9, which provides some indication of orientated ledges. However, in no case were distinct facets observed and the largest structured features that we detected were less than 2 nm in height and approximately 20 nm in lateral extent. Therefore, the evidence that the high-index surfaces facet to low-index orientations is weak.

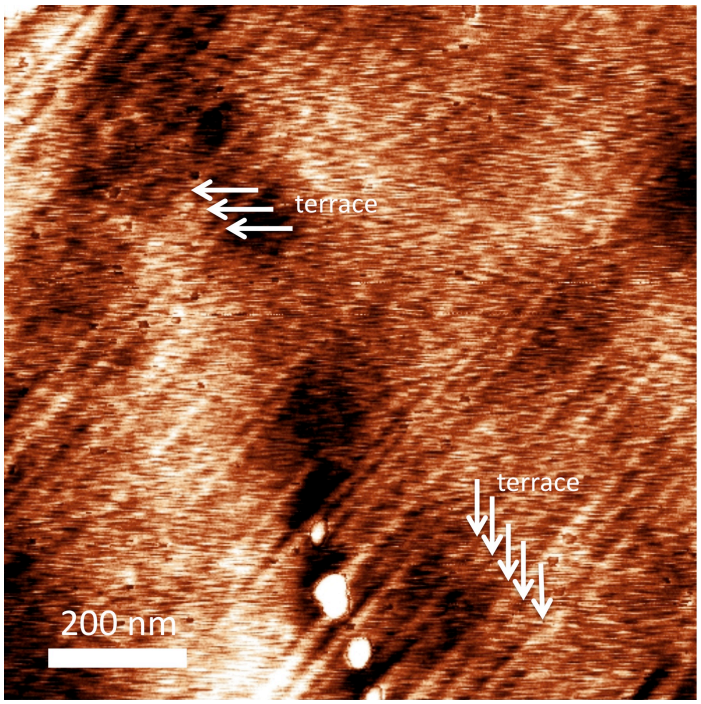

Figure 7.9 AFM images of a $BiFeO_3$ grain misoriented ~ 10 ° from $(100)_{BFO}$ Some of contrasts suggest the presence of terraces (see white arrows). The contrast from bright to dark is 2 nm.

The conclusion that the underlying principle governing the ORs in the $BiFeO_3/TiO_2$ system is the alignment of closest-packed planes and directions was made possible by examining ORs on a wide range of high-index surfaces, using the new CSE technique. Compared to film growth experiments on single-crystal

substrates, the CSE technique allows hundreds of film growth experiments to be conducted in parallel and can, therefore, be considered a high-throughput method for investigating ORs. In addition to the highly parallel nature of the technique, there are other advantages. For example, by using polycrystalline substrates, it is possible to grow on phases that cannot be obtained in single-crystal form. Using polycrystalline substrates, it is also relatively easy to alter the lattice parameter by forming a solid solution. Finally, by conducting many growth experiments at once, competitive ORs can be detected and, if of interest, might be stabilized by adjusting the temperature or the lattice parameters of the substrate through alloying.

These observations can now be used to establish relationships between the reactivity of heterostructured samples and the orientation and phase of the substrate/film. This will be done in later chapter by comparing a statistically relevant number of observations of reactivity as a function of the underlying orientation of the $BiFeO_3$ substrate. Because the proportions of ORs are so large for either phase, deducing the orientation of thin films from the orientations established here for thick films is expected to be a strong indicator. By making many observations, the effects of the few outlier ORs can be minimized.

7.4 Conclusion

Titania films deposited on $BiFeO_3$ using PLD are epitaxial for all substrate orientation more than 10 ° from (111). Anatase films grow on $BiFeO_3$ substrates with an OR $(112)_A \,||\, (111)_{BFO}$ and $[1\bar{1}0]_A \,||\, [1\bar{1}0]_{BFO}$; rutile TiO_2 film is grown on $BiFeO_3$ substrates with $(100)_R \,||\, (111)_{BFO}$ and $[001]_R \,||\, [1\bar{1}0]_{BFO}$ or $(100)_R \,||\, (111)_{BFO}$ and $[001]_R$

|| $[\bar{1}2\bar{1}]_{BFO}$. Anatase grows on substrate orientations within about 30 ° of (001) and rutile films grow on orientations further away. The persistence of strong epitaxy on the highest-index surfaces suggests that the three-dimensional alignment of the closes-packed networks is important and that lattice matching in specific low-index planes is a special case of this more general phenomenon. The dominant ORs align the closest-packed directions and planes of the substrate and film.

References:

[1]N. V. Burbure, P. A. Salvador, and G. S. Rohrer, "Photochemical Reactivity of Titania Films on $BaTiO_3$ Substrates: Influence of Titania Phase and Orientation," *Chem. Mater.,* **22**[21] 5831-37 (2010).

[2]N. V. Burbure, P. A. Salvador, and G. S. Rohrer, "Orientation and Phase Relationships between Titania Films and Polycrystalline $BaTiO_3$ Substrates as Determined by Electron Backscatter Diffraction Mapping," *J. Am. Ceram. Soc.,* **93**[9] 2530-33 (2010).

[3]Y. Zhang, A. M. Schultz, L. Li, H. Chien, P. A. Salvador, and G. S. Rohrer, "Combinatorial Substrate Epitaxy: A High-Throughput Method for Determining Phase and Orientation Relationships and Its Application to $BiFeO_3/TiO_2$ Heterostructures," *Acta Mater.,* **60** 6486-93 (2012).

[4]F. J. Humphreys, Y. Huang, I. Brough, and C. Harris, "Electron Backscatter Diffraction of Grain and Subgrain Structures - Resolution Considerations," *J. Microsc.,* **195** 212-16 (1999).

[5]M. Okeeffe, "Arrangements of Ions in Crystals," *Acta Crystallogr. A,* **33**[Nov] 924-27 (1977).

[6]S. A. Chambers, C. M. Wang, S. Thevuthasan, T. Droubay, D. E. McCready, A. S. Lea, V. Shutthanandan, and C. F. Windisch, "Epitaxial Growth and Properties of MBE-Grown Ferromagnetic Co-Doped TiO_2 Anatase Films on $SrTiO_3$(001) and $LaAlO_3$(001)," *Thin Solid Films,* **418**[2] 197-210 (2002).

[7]S. Chen, M. G. Mason, H. J. Gysling, G. R. Pazpujalt, T. N. Blanton, T. Castro, K. M. Chen, C. P. Fictorie, W. L. Gladfelter, A. Franciosi, P. I. Cohen, and J. F. Evans, "Ultrahigh-Vacuum Metalorganic Chemical-Vapor-Deposition Growth and In-Situ Characterization of Epitaxial TiO_2 Films," *J. Vac. Sci. Technol. A,* **11**[5] 2419-29 (1993).

[8]P. Fisher, O. Maksimov, H. Du, V. D. Heydemann, M. Skowronski, and P. A. Salvador, "Growth, Structure, and Morphology of TiO_2 Films Deposited by Molecular Beam Epitaxy in Pure Ozone Ambients," *Microelectron. J.,* **37**[12] 1493-97 (2006).

[9]C. C. Hsieh, K. H. Wu, J. Y. Juang, T. M. Uen, J. Y. Lin, and Y. S. Gou, "Monophasic TiO_2 Films Deposited on $SrTiO_3$(100) by Pulsed Laser Ablation," *J. Appl. Phys.,* **92**[5] 2518-23 (2002).

[10]R. J. Kennedy and P. A. Stampe, "The Influence of Lattice Mismatch and Film Thickness on the Growth of TiO_2 on $LaAlO_3$ and $SrTiO_3$ Substrates," *J. Cryst. Growth,* **252**[1-3] 333-42 (2003).

[11]M. Murakami, Y. Matsumoto, K. Nakajima, T. Makino, Y. Segawa, T. Chikyow, P. Ahmet, M. Kawasaki, and H. Koinuma, "Anatase TiO_2 Thin Films Grown on Lattice-Matched $LaAlO_3$ Substrate by Laser Molecular-Beam Epitaxy," *Appl. Phys. Lett.,* **78**[18] 2664-66 (2001).

[12]W. Sugimura, T. Yamazaki, H. Shigetani, J. Tanaka, and T. Mitsuhashi, "Anatase-Type TiO_2 Thin Films Produced by Lattice Deformation," *Jpn. J. Appl. Phys. 1,* **36**[12A] 7358-59 (1997).

[13]X. Weng, P. Fisher, M. Skowronski, P. A. Salvador, and O. Maksimovc, "Structural Characterization of TiO_2 Films Grown on $LaAlO_3$ and $SrTiO_3$ Substrates Using Reactive Molecular Beam Epitaxy," *J. Cryst. Growth,* **310**[3] 545-50 (2008).

[14]S. Yamamoto, T. Sumita, T. Yamaki, A. Miyashita, and H. Naramoto, "Characterization of Epitaxial TiO_2 Films Prepared by Pulsed Laser Deposition," *J. Cryst. Growth,* **237** 569-73 (2002).

[15]W. Gao, R. Klie, and E. I. Altman, "Growth of Anatase Films on Vicinal and Flat $LaAlO_3$ (110) Substrates by Oxygen Plasma Assisted Molecular Beam Epitaxy," *Thin Solid Films,* **485**[1-2] 115-25 (2005).

[16]A. Lotnyk, S. Senz, and D. Hesse, "Epitaxial Growth of TiO_2 Thin Films on $SrTiO_3$, $LaAlO_3$ and Yttria-Stabilized Zirconia Substrates by Electron Beam Evaporation," *Thin Solid Films,* **515**[7-8] 3439-47 (2007).

[17]A. Lotnyk, S. Senz, and D. Hesse, "Orientation Relationships of $SrTiO_3$ and $MgTiO_3$ Thin Films Grown by Vapor-Solid Reactions on (100) and (110) TiO_2 (rutile) Single Crystals," *J. Phys. Chem. C,* **111**[17] 6372-79 (2007).

[18]V. F. Silva, V. Bouquet, S. Deputier, S. Boursicot, S. Ollivier, I. T. Weber, V. L. Silva, I. M. G. Santos, M. Guilloux-Viry, and A. Perrin, "Substrate-Controlled Allotropic Phases and Growth Orientation of TiO_2 Epitaxial Thin Films," *J. Appl. Crystallogr.,* **43** 1502-12 (2010).

[19]S. M. Selbach, M. A. Einarsrud, and T. Grande, "On the Thermodynamic Stability of $BiFeO_3$," *Chem. Mater.,* **21**[1] 169-73 (2009).

Chapter 8 Influence of Phase and Orientation on Photocatalytic Activity of TiO_2/$BiFeO_3$ Heterostructure

8.1 Introduction

The knowledge of the orientation relationships of TiO_2 and $BiFeO_3$ enables detailed studies of how the photocatalytic activity of TiO_2/$BiFeO_3$ varies with the phase and orientation of TiO_2.

At the outset of this research, it was hypothesized that the strength of polarization is the dominating factor for photocatalytic activity, therefore $BiFeO_3$ grains oriented along (111) will have the highest activity. On the other hand, the orientation-averaged observations made in Chapter 6 indicated that only the sign of the polarization was important to reactivity. We will further distinguish between these possibilities herein. A simple energy level diagram of $BiFeO_3$ in contact with solution is constructed in Fig. 8.1. The bands of a p-type semiconductor, which is the most common conductivity type for $BiFeO_3$,[1,2] generally bend downward at the solid-liquid interface.[3] Depending on the direction of spontaneous polarization (P_s), the bands of $BiFeO_3$ at the solid-liquid interface can bend less downward, or even upward as depicted in (a), or more downward as depicted in (b). The change in the band bending can either inhibit (a) or facilitate (b) the movement of electrons toward the solution.

These two energy level diagrams are comparable to the ones presented in Fig. 2.11 (a, b) for TiO_2/$BiFeO_3$, which argues that similar photochemical behavior should be observed for the bare $BiFeO_3$ substrate and the heterostructure. This

hypothesis is based on the idea that electrons photogenerated in $BiFeO_3$ are responsible for reactivity. Without a priori knowledge of all the stored charges at the interface, one can postulate that the reactivity should increase with increasing positive strength of P_s. Stronger positive polarizations should lead to stronger band bending and wider space charge regions, which drives more excited electrons to the interface (assuming the space charge width is smaller than the absorption depth in the sample). In this argument, the most reactive grains are expected to be the ones with the strongest positive polarization, namely those along [111]. Therefore, the most reactive $BiFeO_3$ grains are to be found on surfaces oriented at (111) planes, similar to the case of ferroelectric $BaTiO_3$, where the most reactive grains are oriented at (001) planes.[4,5] It should be noted that, if the absorption depth is narrower than the space charge width, then only the sign of the polarity should be important. In this chapter, we aim to establish a correlation between orientation and reactivity, to distinguish between the limiting cases (but not distinguish between total polarization, space charge width, and absorption depth directly).

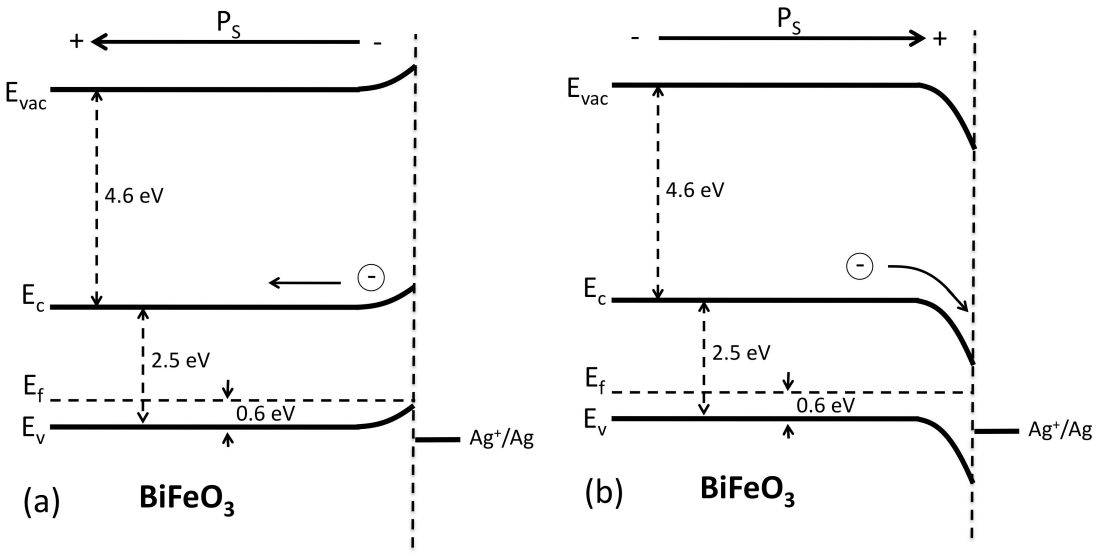

Figure 8.1 The band structures of p-type $BiFeO_3$ in contact with solution. The P_s is directed away from the solid-liquid interface in (a), bending the bands upward. The P_s is directed to the solid-liquid interface in (b), bending the bands downward.

In addition to the influence of polarization and space charge width, the crystallographic orientations of $BiFeO_3$ and the phase and orientation of TiO_2 may have significant influence on photocatalytic activity. These are well known to affect the reactivity of other photocatalysts, especially non-ferroelectric ones.[6-11] On the other hand, UV-light photochemical reactivity in $BaTiO_3$ was correlated to the magnitude of the polarization, and the phase and orientation of thin titania films supported on $BaTiO_3$ correlated with the reactivity of the substrate, and were not strong functions of orientation and phase, unlike bulk TiO_2. Therefore, the effects of orientation and phase of both the $BiFeO_3$ substrate and the heterostructure are examined in this chapter.

8.2 Experimental

The orientation maps of a bare $BiFeO_3$ substrate used for reactivity analysis and another $BiFeO_3$ substrate on which a 10 nm thick TiO_2 film was deposited by PLD later (and then which was used for reactivity analysis) were obtained using the EBSD technique. AFM topographic images were taken before and after a 20-min photochemical reduction of Ag was carried out under illumination from a blue LED operated at 100 mA. Maps were registered from 30 grains on the bare $BiFeO_3$ and 26 grains on the $TiO_2/BiFeO_3$.

8.3 Results and Discussion

In Fig. 8.2, the AFM topographic images registered after reaction are shown for four reactive grains (a1) – (a4) and four unreactive grains (b1) – (b4). The white dots are reduced Ag particles deposited on the surfaces. Some of the features in these images include pores (P), surface scratches (SS), surface steps (S), grain boundaries (GB), and surface contaminations (SC), which are marked in the images. Note that the Ag particles in (a1-a3) are distributed in spatially selective patterns, but in (a4) they are less so, which is likely a result of having one large domain in the field of view. This spatial selectivity is attributed to the influence from polarizations in ferroelectric domains, as seen in ref,[12] and the work presented in Chapter 5 and 6 (see Fig. 5.1(b)).[13] There are a few white speckled features in (b1-b4), but they do not form any spatially selective patterns. Those less significant features could be a small amount of reduced Ag particles from background reactions or surface

contaminations from immersion in $AgNO_3$ solution. The grains in (a1-a4) are much more reactive than the grains in (b1-b4) and the Ag deposition due to the secondary sources, that in (b1-b4), does not significantly affect the interpretation of the results. The topography of a line marked as red in Fig. 8.2(a1) and a line marked as blue in Fig. 8.2(b1) are compared in Fig. 8.3(c). The maximum heights of the spiked features (attributed to Ag particles) are in the range of 50 to 130 nm on the reactive grain; the maximum heights of spiked features (attributed to either Ag or surface contamination) for the unreactive grain do not exceed 20 nm.

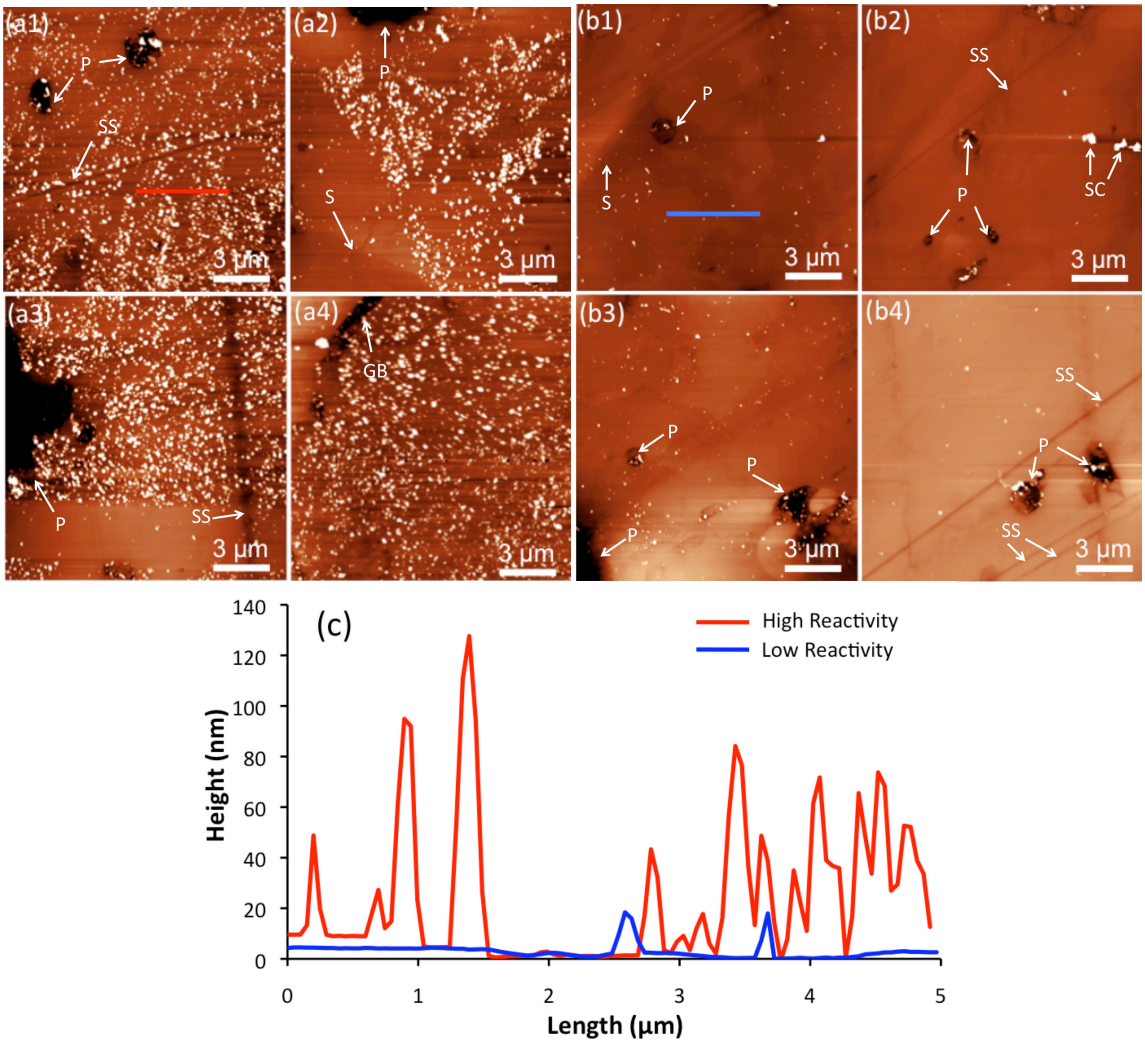

Figure 8.2 AFM topographic images of four reactive grains (a1-a4) and four unreactive grains (b1-b4) after photochemical reaction. The bright dots indicate reduced Ag particles. The contrast from bright to dark is 100 nm for all images. The height profiles of the red and the blue segments in (a1) and (b1) extracted from the images are compared in panel (c).

The reactivity of all of the 30 grains on the $BiFeO_3$ substrate is summarized in the stereographic orientation triangle shown in Fig. 8.3. This triangle covers all possible orientations in a cubic crystallographic system, as the structure of $BiFeO_3$ in this work is treated as pseudo-cubic. The three vertices indicate low index planes

(001), (101), and (111), respectively. Among the 30 grains, 15 are considered reactive, marked by closed blue circles; 15 grains are considered unreactive, marked by open orange circles. The AFM images in Fig. 8.2 are of the grains marked with additional black squares. The most important finding from this figure is that 13 of the 15 reactive grains are clustered in the corner of (001). Calculation of the misorientation angles shows that they are within ~10 ° of [001]. The locations of the unreactive grains are found away from (001).

The two grains in the unreactive region, whose AFM images shown in Fig. 8.4, exhibit silver deposits of dissimilar sizes and shapes as compared to those observed in the reactive region shown in Fig. 8.2 (a1-a4). The exact reason for such features of the two grains remains to be explored and is not the focus of interest in this work.

What is important is that the regions of reactive and unreactive grains can be separated in orientation space, as indicated loosely by the dashed red line in the triangle. This observation stands in contrast to the observations for the $BaTiO_3$ photochemical reactivity, which was not dependent on orientation. Also, this indicates that the strength of the out-of-plane spontaneous polarization is not the only factor that dictates the photocatalytic activity of $BiFeO_3$ grains: orientation plays an important role as well. It is known that orientation plays an important role in the reactivity of certain photochemical catalysts, such as TiO_2, $SrTiO_3$, and Fe_2O_3.[5-11,14] Factors that have been invoked to understand orientation dependence include dissimilar surface energies, defect concentrations, the local band structures, and surface charges. Further study on those factors is needed to explain the current

observation, but what is clear is that both surface orientation and polarization play a role in reactivity, as spatial selectivity is observed for the reactive grains near the (001).

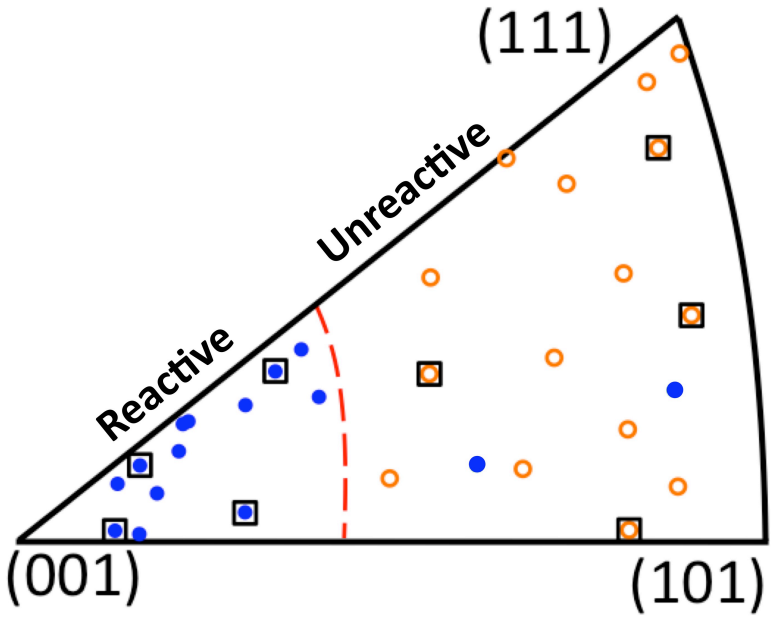

Figure 8.3 Locations of 30 examined grains on the $BiFeO_3$ substrate in a stereographic orientation triangle. Closed blue circles indicate reactive grains; open orange circles indicate unreactive grains; closed green circles indicate abnormal grains. The dashed red line separates the reactive grains and the unreactive ones. AFM images of four reactive grains and four unreactive grains marked by black boxes are given in Fig. 8.2. AFM images of the two reactive grains in the unreactive region are given in Fig. 8.4.

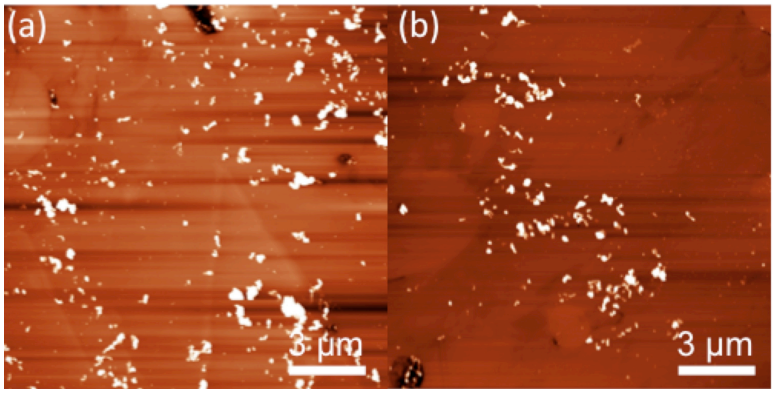

Figure 8.4 AFM topographic images of the two abnormal grains (a) & (b). Relatively large bright features are observed on their surfaces. The contrast from bright to dark is 100 nm for both images.

The result of reactivity against grain orientation for another $BiFeO_3$ substrate, which was used in Chapter 6, is generally consistent with the observation in Fig. 8.3. The plot in Fig. 8.5 has also 30 data points. 10 of the 14 grains in the reactive region and 6 of the 16 grains in the unreactive region are considered to be reactive. Although the separation of reactive and unreactive grains in the orientation space is not as sharp as in Fig. 8.3, the result still suggests a higher chance in finding reactive grains within ~ 10° of [001].

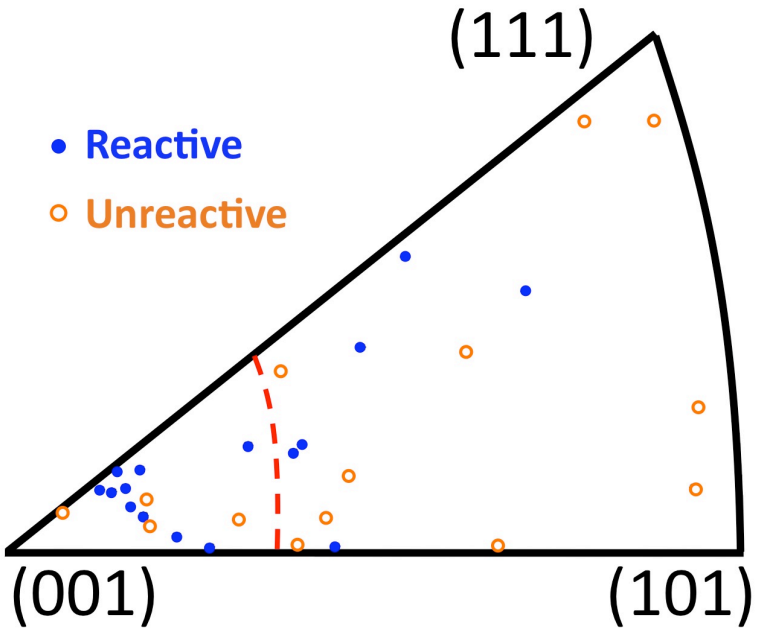

Figure 8.5 Locations of 30 examined grains on the $BiFeO_3$ substrate examined in Chapter 6 in a stereographic orientation triangle.

In Fig. 8.6, AFM topographic images are given for grains from the $TiO_2/BiFeO_3$ heterostructure; these were taken from three reactive grains (a1-a3) exhibiting spatial selectivity, and from three unreactive grains (b1-b3). In addition to all the features described in Fig. 8.2(a1-b4), minority phase inclusions (MP) and features of unknown origin (U), which were created likely during film deposition, are marked. Note that the contrasts ascribed to the reduced Ag in Fig. 8.6 (a1-a3) are less bright as compared to Fig. 8.2 (a1-a4), which implies that the 10 nm TiO_2 film is less reactive than the bare substrate. (Keep in mind that 10 nm and bulk TiO_2 are not reactive in blue light.) Height profiles from the blue and red lines if Fig. 8.6(a) and (b) are given in Fig. 8.7(c). Comparison of the height profiles given in Fig. 8.6(c) and in Fig. 8.2(c) shows a smaller difference between the reactivity of reactive and unreactive grains in the film as compared to the bare substrate. The maximum

heights of spiked features for the reactive grain are in the range of 20 to 40 nm; those for the unreactive grain are less than 20 nm. Recall that the heights of Ag deposits on the reactive grains in the bare substrate are 50 to 130 nm. The reactivity is decreased, on average, with a TiO_2 film for $BiFeO_3$ substrates, an observation consistent with the previous finding[13] presented in Chapter 5.

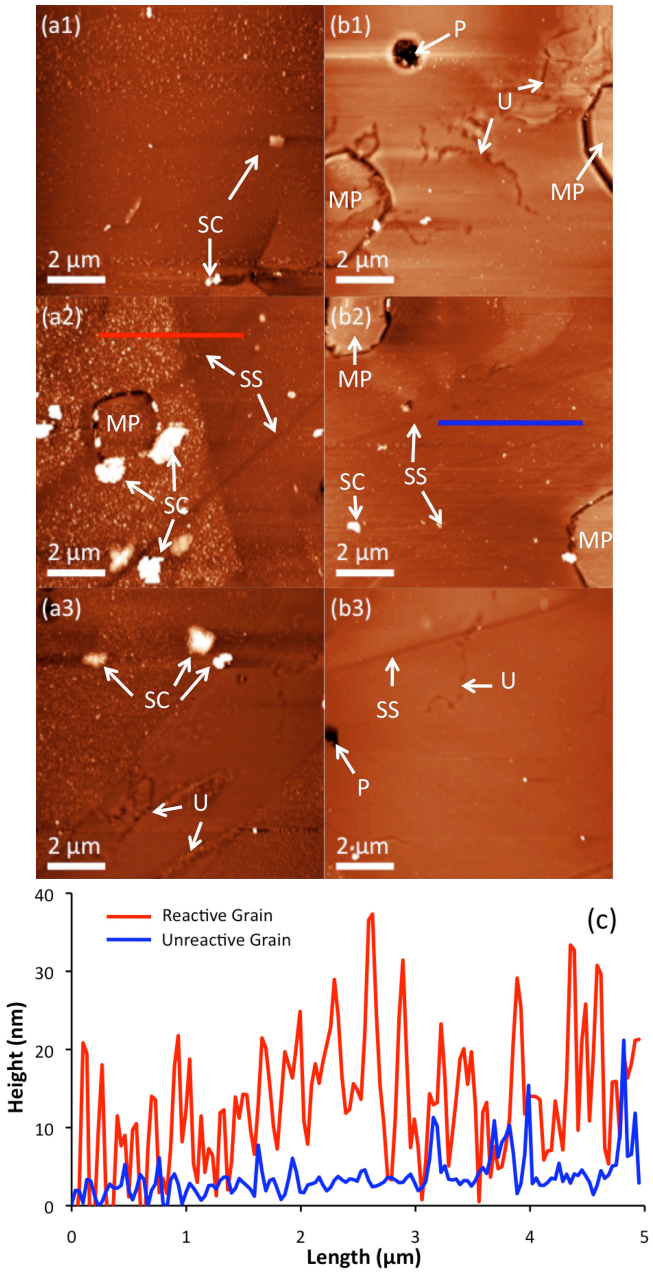

Figure 8.6 AFM topographic images of three reactive grains (a1-a3) and three unreactive grains (b1-b3) are sampled. The bright dots indicate reduced Ag particles. The contrast from bright to dark is 100 nm for all images. Two height profiles of the red and the blue segments in (a2) and (b2) are compared in panel (c).

The result for all of the 26 grains is summarized in the orientation triangle in Fig. 8.7 (a). In like manner, the result for another 26 grains of the 10 nm

$TiO_2/BiFeO_3$ heterostructure examined in Chapter 6 is plotted in Fig. 8.7 (c). Again, closed blue circles indicate reactive grains, and open orange circles indicate unreactive grains. The circles boxed by black squares are sampled grains with their AFM topographic images shown in Fig. 8.6 (a1-b3). The dashed red lines in Fig. 8.7 (a, c) are drawn in identical position as in the triangle in Fig. 8.3 that loosely delineated the reactive from unreactive grains. Compared to the results of the bare $BiFeO_3$ substrate, reactive TiO_2 grains supported on $BiFeO_3$ grains are found spread out in orientations close and far from (001). That all of the four grains on the left side of the red line are reactive in Fig. 8.7 (a) and that 4 of the 6 grains are reactive in the same region in Fig. 8.7 (c) are generally consistent with the bare substrate cases in Fig. 8.3 and in Fig. 8.5. On the other sides, 7 of 22 grains in (a) and 12 of 20 grains in (c) are considered reactive, as opposed to only 2 of 17 and 6 of 16 in the bare substrate cases. The orientations of the $BiFeO_3$ grains supporting those 7 and 12 grains are scattered. Fig. 8.7 (b) is a stereographic orientation triangle borrowed from Chapter 7 (see Fig 7.4 (a)) summarizing the $BiFeO_3$ orientations allowing the growth of anatase and rutile, respectively. The growth fields of anatase and rutile are separated by a black dash-dot line in the Fig. 8.7 (b). The same lines are drawn in Fig. 8.7 (a, c) so that the TiO_2 phases for those grains are clear.

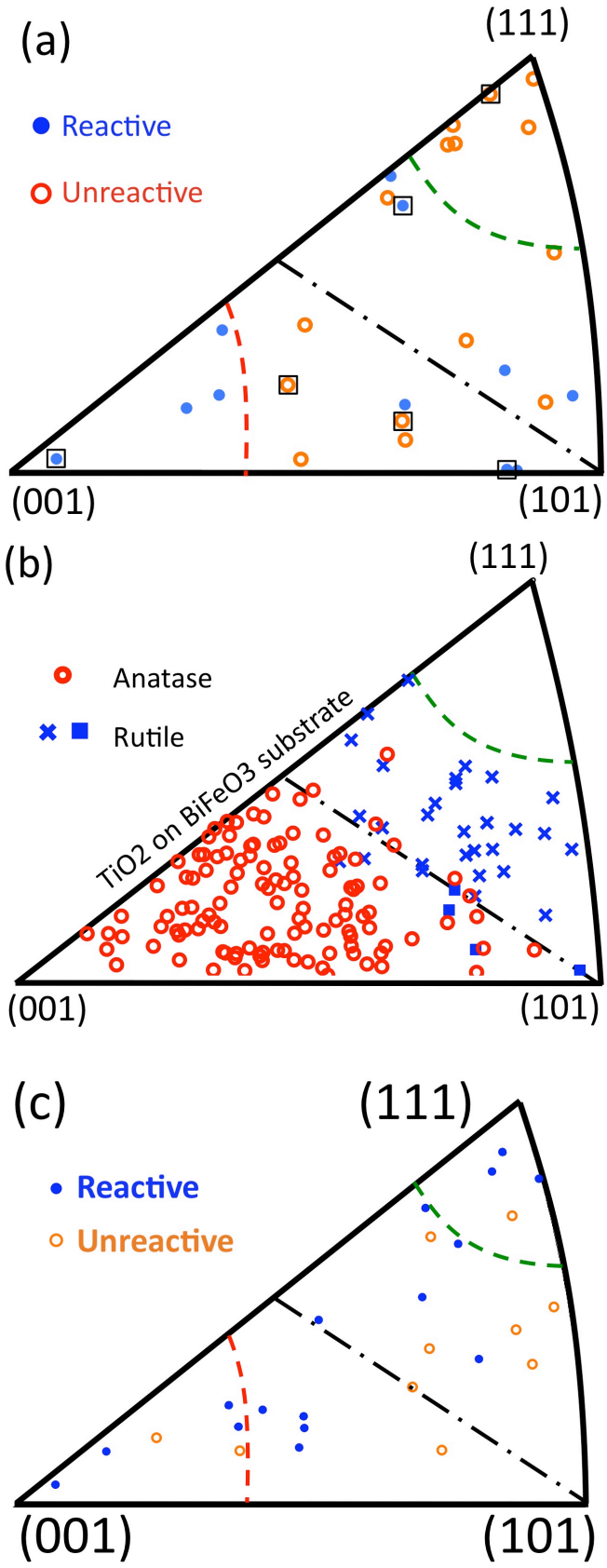
(a)
(111)
Reactive
Unreactive
(001)
(101)
(b)
(111)
Anatase
Rutile
TiO2 on BiFeO3 substrate
(001)
(101)
(c)
(111)
Reactive
Unreactive
(001)
(101)

Figure 8.7 (a) Locations of the 26 $BiFeO_3$ grains supporting the examined TiO_2 film grains in the stereographic orientation triangle. Closed blue circles indicate reactive grains; open orange circles indicate unreactive grains. AFM images of the grains marked by circles boxed with black squares are presented in Fig. 8.6 (a1–a3, b1–b3). (b) The orientation triangle summarizing the $BiFeO_3$ orientations allowing the epitaxial growth of anatase and rutile, respectively, from Fig. 7.4 (a). The red symbols indicate anatase and the blue symbols indicate rutile. A dashed green line is drawn near the empty corner of (111) where no crystalline phase of TiO_2 is observed. A dash-dot black line is drawn to separate the growth fields of anatase and rutile. (c) Locations of the 26 grains of the $TiO_2/BiFeO_3$ heterostructure used in Chapter 6. The dashed red lines (a, c) are in the same position as in Fig. 8.3. The same green and black lines are drawn in (a, c) as in (b).

The absence of crystalline TiO_2 phase in the green line bounded region near $(111)_{BFO}$ is speculated in Chapter 7 to be attributed to the poor growth of crystalline TiO_2 on (111)-oriented $BiFeO_3$ grains, which could further lead to high concentration level of defects, which often serve as scattering and recombination centers for charge carriers. The observation that all of the 6 examined grains are unreactive in that very region in Fig. 8.7 (a) seems to be strongly supportive of the argument. But in Fig. 8.7 (c), however, that 3 of the 4 grains are tested reactive renders that argument unsubstantiated. As a result, no correlation can be safely made between poor reactivity of $BiFeO_3$ grains near (111) and the poor crystallinity without further investigation.

Discounting those grown near $(111)_{BFO,}$ 7 of the 12 anatase TiO_2 grains (58%), on the left side of the black line, and 4 of the 8 rutile grains (50%), on the other side, in Fig. 8.7 (a) are reactive. In Fig. 8.7 (c), these two ratios are 8 out of 11 (73%) for anatase and 5 out of 11 (45%) for rutile. The total ratio for reactive anatase grains is 15 out of 23 (65%) and for reactive rutile grains is 9 out of 19 (47%). The observed reactive anatase and rutile grains are of similar reactivity. Based on these

observations, it is concluded that anatase phase is mildly more reactive than rutile phase in the $TiO_2/BiFeO_3$ heterostructure. This is slightly different from the results observed on the $TiO_2/BaTiO_3$ heterostructure, where both phases are of similar reactivity.[15]

When comparing the results for $TiO_2/BiFeO_3$ heterostructures in Fig. 8.7 (a, c) to the results for bare $BiFeO_3$ substrates in Fig. 8.3 and 8.5, it is statistically found that grains in the reactive region on bare substrates bounded by the red line remain reactive on $TiO_2/BiFeO_3$ heterostructures, and that grains elsewhere on bare substrates become more reactive on average with TiO_2 films. After combining the data of two bare substrates and two heterostructures, the ratios of reactive grains to all grains are listed in the following Table 8.1:

	In reactive region	In unreactive region
Bare $BiFeO_3$	23 / 27 (85%)	8 / 33 (24%)
$TiO_2/BiFeO_3$	8 / 10 (80%)	19 / 42 (45%)

Table 8.1 Ratios of reactive grains to all grains in reactive/unreactive regions for bare $BiFeO_3$ substrates and $TiO_2/BiFeO_3$ heterostructures.

Although the TiO_2 film partially decreases the reactivity of the reactive $BiFeO_3$ grains (see profiles in Fig. 8.2 (c) and Fig. 8.6 (c)), a significant improvement of reactivity by the TiO_2 films for those unreactive grains is observed. Also in this region of improvement combining Fig. 8.7 (a) and (c), reactive grains are not found in any preferred orientations in a conceivable manner. Unlike the cases of bulk titania,[7-11] the orientations of both anatase and rutile are not very influential on the reactivity. An overall view of the patterns in Fig. 8.7 (a, c) and in Fig. 8.3 & 8.5

suggests that the photocatalytic behavior of the $TiO_2/BiFeO_3$ heterostructures is mainly dictated by the underlying $BiFeO_3$ substrates, especially that the reactive TiO_2 grains are spatially selective in patterns that follow the domain structures of the substrates.

It is interesting to note that the carriers that participate in the reactivity for both samples emanate from the $BiFeO_3$ substrate. That orientations farther from the (001) orientation are reactive in the heterostructure but not in the bare substrate indicates that carriers in the substrate are indeed shuttled to the surface on these orientations, but for some reason they are not reactive for Ag^+ reduction. That they are spatially selective on these orientations agree too with the earlier observations that domains of a certain polarizations are reactive in a like manner for reactive orientations. However, polarization is not the only factor that dictates reactivity, though only certain polarizations on reactive orientations are reactive, so both polarization and orientation of the $BiFeO_3$ substrate control reactivity. Finally, that the orientation of reactive domains is near (001), indicates that the total out-of-plane polarity, which would occur for orientations on (111), is not the dominant factor for reactivity, but that orientation dominates and polarization supports the reactivity on a specific orientation.

8.4 Conclusion

It is observed from two separate sets of data that the ratio of reactive grains to all grains of $BiFeO_3$ oriented within $\sim 10\,^\circ$ of $[001]$ is high. The anatase titania films are mildly more reactive than the rutile ones, whence the reactivity of

individual anatase and rutile grains are of similar photocatalytic activity. In addition, both titania phases have little preference on crystallographic orientations for higher reactivity. The photocatalytic behavior of the $TiO_2/BiFeO_3$ heterostructures is mainly dictated by a combination of orientation and polarization associated with the $BiFeO_3$ substrates.

References:

[1]H. Yang, H. M. Luo, H. Wang, I. O. Usov, N. A. Suvorova, M. Jain, D. M. Feldmann, P. C. Dowden, R. F. DePaula, and Q. X. Jia, "Rectifying Current-Voltage Characteristics of $BiFeO_3$/Nb-Doped $SrTiO_3$ Heterojunction," *Appl. Phys. Lett.,* **92**[10] (2008).

[2]S. Y. Yang, L. W. Martin, S. J. Byrnes, T. E. Conry, S. R. Basu, D. Paran, L. Reichertz, J. Ihlefeld, C. Adamo, A. Melville, Y. H. Chu, C. H. Yang, J. L. Musfeldt, D. G. Schlom, J. W. Ager, and R. Ramesh, "Photovoltaic Effects in $BiFeO_3$," *Appl. Phys. Lett.,* **95**[6] (2009).

[3]A. J. Bard, "Photoelectrochemistry," *Science,* **207**[4427] 139-44 (1980).

[4]J. L. Giocondi and G. S. Rohrer, "Spatially Selective Photochemical Reduction of Silver on the Surface of Ferroelectric Barium Titanate," *Chem. Mater.,* **13**[2] 241-42 (2001).

[5]J. L. Giocondi and G. S. Rohrer, "The Influence of the Dipolar Field Effect on the Photochemical Reactivity of $Sr_2Nb_2O_7$ and $BaTiO_3$ Microcrystals," *Top. Catal.,* **49**[1-2] 18-23 (2008).

[6]J. L. Giocondi, P. A. Salvador, and G. S. Rohrer, "The Origin of Photochemical Anisotropy in $SrTiO_3$," *Top. Catal.,* **44**[4] 529-33 (2007).

[7]P. A. M. Hotsenpiller, J. D. Bolt, W. E. Farneth, J. B. Lowekamp, and G. S. Rohrer, "Orientation Dependence of Photochemical Reactions on TiO_2 Surfaces," *J. Phys. Chem. B,* **102**[17] 3216-26 (1998).

[8]M. Kobayashi, V. Petrykin, M. Kakihana, and K. Tomita, "Hydrothermal Synthesis and Photocatalytic Activity of Whisker-Like Rutile-Type Titanium Dioxide," *J. Am. Ceram. Soc.,* **92**[1] S21-S26 (2009).

[9]J. B. Lowekamp, G. S. Rohrer, P. A. M. Hotsenpiller, J. D. Bolt, and W. E. Farneth, "Anisotropic Photochemical Reactivity of Bulk TiO_2 Crystals," *J. Phys. Chem. B,* **102**[38] 7323-27 (1998).

[10]T. Ohno, K. Sarukawa, and M. Matsumura, "Crystal Faces of Rutile and Anatase TiO_2 Particles and Their Roles in Photocatalytic Reactions," *New J. Chem.,* **26**[9] 1167-70 (2002).

[11]T. Taguchi, Y. Saito, K. Sarukawa, T. Ohno, and M. Matsumura, "Formation of New Crystal Faces on TiO_2 Particles by Treatment with Aqueous HF Solution or Hot Sulfuric Acid," *New J. Chem.,* **27**[9] 1304-06 (2003).

[12]A. M. Schultz, Y. L. Zhang, P. A. Salvador, and G. S. Rohrer, "Effect of Crystal and Domain Orientation on the Visible-Light Photochemical Reduction of Ag on $BiFeO_3$," *ACS Appl. Mater. Inter.,* **3**[5] 1562-67 (2011).
[13]Y. Zhang, G. S. Rohrer, A. M. Schultz, and P. A. Salvador, "Spatially Selective Visible Light Photocatalytic Activity of $TiO_2/BiFeO_3$ Heterostructures," *J. Mater. Chem.,* **21**[12] 4168-74 (2011).
[14]A. M. Schultz, P. A. Salvador, and G. S. Rohrer, "Enhanced Photochemical Activity of Alpha-Fe_2O_3 Films Supported on $SrTiO_3$ Substrates under Visible Light Illumination," *Chem. Commun.,* **48**[14] 2012-14 (2012).
[15]N. V. Burbure, P. A. Salvador, and G. S. Rohrer, "Photochemical Reactivity of Titania Films on $BaTiO_3$ Substrates: Influence of Titania Phase and Orientation," *Chem. Mater.,* **22**[21] 5831-37 (2010).

Chapter 9 Conclusions

In this chapter, the conclusions from chapter 5 to 8 are summarized. Whether the three hypotheses are supported or rejected based on the conclusions is presented.

Visible-Light Photocatalytic Activity of $TiO_2/BiFeO_3$

In Chapter 5, thin TiO_2 films supported on $BiFeO_3$ substrates were observed to reduce Ag^+ cations from aqueous $AgNO_3$ solutions when irradiated by visible blue light with energy less than titania's band gap. The patterns of reduced silver on the TiO_2 surface mimicked the domain structure in the $BiFeO_3$ substrate. The hypothesis that electrons photogenerated by blue light irradiation migrate under the influence of ferroelectric polarization from the $BiFeO_3$ substrate to the TiO_2 film surface and then participate in the photochemical reduction of Ag^+ in aqueous solution is supported by the experimental observations.

In Chapter 6, the observations show that domains of same polarity photocatalytically behave the same, in the bare $BiFeO_3$ substrate and in the $TiO_2/BiFeO_3$ heterostructure. The vertical piezoresponse force microscopy (VPFM) results suggest that the photochemical reduction of Ag^+ occurs on domains with low magnitude signals, which can be correlated to the polarization direction. We speculated there that these are positive domains, but the polarity of the reactive domains remains to be resolved. Nevertheless, it is clearly shown that domain

polarity is the dominating factor in determining the photochemical activity in $BiFeO_3$ and the heterostructure.

Orientation Relationships of TiO_2 and $BiFeO_3$

In Chapter 7, TiO_2 films deposited on polycrystalline $BiFeO_3$ substrates using PLD in the temperature range of 500 – 700 °C were determined to be epitaxial for all substrate orientations > 10 ° from $BiFeO_3$ (111). Anatase grows on substrate orientations within about 30 ° of (001) and rutile films grow on other orientations. Anatase films are grown on $BiFeO_3$ substrates with an OR $(112)_A \parallel (111)_{BFO}$ and $[1\bar{1}0]_A \parallel [1\bar{1}0]_{BFO}$; rutile TiO_2 film is grown on $BiFeO_3$ substrates with $(100)_R \parallel (111)_{BFO}$ and $[001]_R \parallel [1\bar{1}0]_{BFO}$ or $(100)_R \parallel (111)_{BFO}$ and $[001]_R \parallel [\bar{1}2\bar{1}]_{BFO}$. The new high-throughput Combinatorial Substrate Epitaxy (CSE) technique described in this work uncovered a persistence of strong epitaxy on the high-index surfaces that are consistent with observations made is prior work on low-index titania epitaxy on perovskites. The dominant ORs align the closest-packed directions and planes of the substrate and film, and this indicates that the three-dimensional alignment of the closest-packed networks is the driver for epitaxy and that lattice matching in specific low-index planes is a special case of this more general phenomenon.

Influence of Phase and Orientation on Photocatalytic Activity

It is observed from two separate sets of data that the ratio of reactive grains to all grains of $BiFeO_3$ oriented within ~ 10 ° of $[001]$ is high. The anatase titania films are mildly more reactive than the rutile ones, whence the reactivity of

individual anatase and rutile grains are of similar photocatalytic activity. In addition, both titania phases have little preference on crystallographic orientations for higher reactivity. The photocatalytic behavior of the $TiO_2/BiFeO_3$ heterostructures is mainly dictated by a combination of orientation and polarization associated with the $BiFeO_3$ substrates.

Ferroelectric $BiFeO_3$-supported titania films have exhibited enhanced photocatalytic activity in the visible-light range. This enhancement is primarily ascribed to the visible-light-absorbing ferroelectric substrate $BiFeO_3$. Together with the prior work on $TiO_2/BaTiO_3$ in our group,[1-8] this work created a novel path to achieve efficient photocatalysts in harvesting solar energy. This study also suggests the possibility of controlling specific reactions on the surface of heterostructured ferroelectric photocatalysts, a benefit that can be extended into fields beyond solar energy, via engineering grain orientations and domain polarizations during the synthesis stage.

Reference:

[1]N. V. Burbure, "Influence of Ferroelectric Substrates on the Photochemical Reactivity of Titanium Dioxide Thin Films," *PhD Thesis* (2009).

[2]N. V. Burbure, P. A. Salvador, and G. S. Rohrer, "Influence of Dipolar Fields on the Photochemical Reactivity of Thin Titania Films on $BaTiO_3$ Substrates," *J. Am. Ceram. Soc.,* **89**[9] 2943-45 (2006).

[3]N. V. Burbure, P. A. Salvador, and G. S. Rohrer, "Photochemical Reactivity of Titania Films on $BaTiO_3$ Substrates: Origin of Spatial Selectivity," *Chem. Mater.,* **22**[21] 5823-30 (2010).

[4]N. V. Burbure, P. A. Salvador, and G. S. Rohrer, "Photochemical Reactivity of Titania Films on $BaTiO_3$ Substrates: Influence of Titania Phase and Orientation," *Chem. Mater.,* **22**[21] 5831-37 (2010).

[5]N. V. Burbure, P. A. Salvador, and G. S. Rohrer, "Orientation and Phase Relationships between Titania Films and Polycrystalline $BaTiO_3$ Substrates as Determined by Electron Backscatter Diffraction Mapping," *J. Am. Ceram. Soc.,* **93**[9] 2530-33 (2010).
[6]J. L. Giocondi and G. S. Rohrer, "Spatial Separation of Photochemical Oxidation and Reduction Reactions on the Surface of Ferroelectric $BaTiO_3$," *J. Phys. Chem. B,* **105**[35] 8275-77 (2001).
[7]J. L. Giocondi and G. S. Rohrer, "Spatially Selective Photochemical Reduction of Silver on the Surface of Ferroelectric Barium Titanate," *Chem. Mater.,* **13**[2] 241-42 (2001).
[8]J. L. Giocondi and G. S. Rohrer, "The Influence of the Dipolar Field Effect on the Photochemical Reactivity of $Sr_2Nb_2O_7$ and $BaTiO_3$ Microcrystals," *Top. Catal.,* **49**[1-2] 18-23 (2008).